Institut de Physique du Globe de Paris

Ecole doctorale des Sciences de la Terre

Thèse de Doctorat

pour l'obtention du titre de

Docteur en Science

de l'Institut de Physique du Globe de Paris

Specialité : Geophysique

Soutenue par

Clément Thorey

Magmatisme intrusif sur les planètes telluriques

Équipe Planétologie et Sciences Spatiales,

Défendue le 5 Décembre, 2013.

Jury :

Directeur:	Chloé Michaut	-	IPGP (Paris)
Co-directeur:	Mark Wieczorek	-	IPGP (Paris)
Rapporteur :		-	
Rapporteur :		-	
Examinateur :		-	
Examinateur :		-	

Remerciements

Je remercie marion rouault mae sans qui tout ceci n'aurait jamais vu le jour ;)

Contents

Résumé de la problématique et résultats principaux

Part I

Dynamique des magmas magma à faible profondeur

Chapter 1
Magmatisme intrusif

Contents

1.1 Formation, transport et stockage des magmas

1.1.1 Formation

Sur Terre, la majorité des magmas sont formés par fusion partielle des roches du manteau supérieur. Dans les conditions normales de pression, la température du manteau supérieur n'est pourtant pas suffisante pour provoquer leur fusion (Figure 1.1) et d'autres mécanismes sont nécessaires pour amener les roches du manteau à croiser leur liquidus. Au niveau des dorsales en contexte océanique ou des rifts en contexte continental ou encore au sein des panaches mantelliques, la fusion partielle est ainsi générée par décompression (Figure 1.1 b). Au niveau des zones de subduction, les mécanismes mis en jeu sont plus complexes et font intervenir la déshydratation par chauffage des roches et la migration des fluides abaissant le liquidus et provoquant ainsi la fusion des roches alentour (Figure 1.1 c).

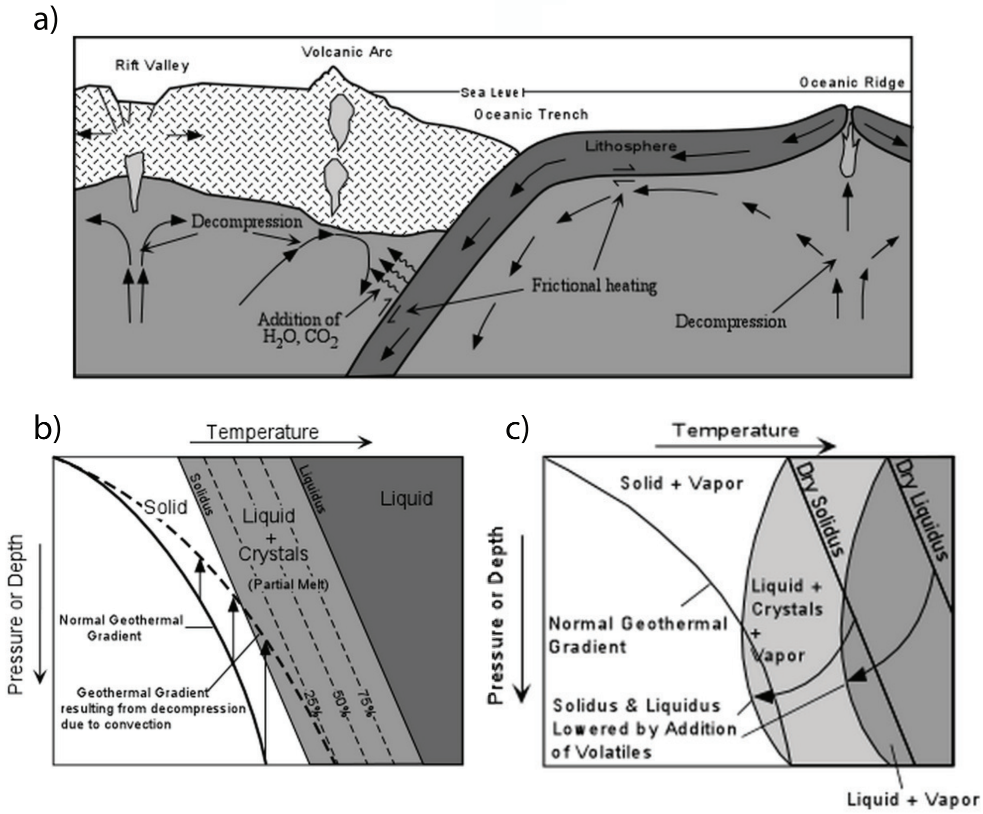

Figure 1.1: a) Lien entre le magmatisme et la tectonique des plaques: production de magma par fusion partielle par décompression au niveau des dorsales océaniques ou des rifts en contexte continental ou par addition de volatiles au niveau des zones de subduction. Schéma du diagramme de phase des roches du manteau supérieur dans deux contextes différents: b) dorsale océanique ou panache mantellique, c) zone de subduction.

1.1.2 Transport

Les liquides de fusions ainsi formés sont moins denses que les roches alentours et s'élèvent donc, par compaction et percolation, au sein de la source (*McKenzie*, 1984, 1985). Le transport du magma depuis la source jusqu'au couches superficielles de la lithosphère a longtemps était l'objet de débat (*Clemens* *and Mawer*, 1992; *Miller and Paterson*, 1999). Cependant, les modèles de gros volumes diapiriques de magma remontant lentement au sein de la lithosphère, invoqués traditionnellement notamment pour expliquer la présence de gros volumes de magma intrudés au sein de la croûte à l'érosion (dans la vallée du Yosemite aux Etats-Unis par exemple), sont maintenant en désaveux. En effet, il est maintenant admis que ces gros volumes se sont mis en place par incrément successif de magmas et que celui ci est transporté depuis la source rapidement au sein de le croûte au sein de chenaux verticaux, i.e. de dykes ou le long de failles préexistantes (*Clemens and Mawer*, 1992; *Petford et al.*, 1993; *Rubin*, 1995; *Glazner et al.*, 2004).

1.1.3 Stockage

Les travaux de *Walker* (1989) ont montré que les magmas remontent jusqu'à rencontrer leur zone de flottabilité neutre, une région où la densité de la roche encaissante est proche de celle du magma lui-même. En effet, au-dessus de cette couche, le magma est plus dense que la roche encaissante et sa flottabilité l'entraîne vers le bas. De nombreux travaux, tant théoriques (*Lister and Kerr*, 1991; *Petford et al.*, 1993; *Rubin*, 1995) qu'expérimentaux (*Taisne and Tait*, 2009; *Taisne et al.*, 2011) ont en effet depuis montré que l'ascension d'un dyke était contrôlée par la différence de densité entre la tête de celui-ci et la roche encaissante. Lorsque le dyke entre dans une région de densité inférieure, la souspression induite peut, sous certaines conditions, conduire à l'étalement du magma au niveau de la base de la région de plus faible densité permettant ainsi la formation de réservoir magmatique sous forme d'intrusion magmatique au sein de la croûte (*Taisne et al.*, 2011).

Plus récemment, d'autres études ont montré que les contrastes de rigidité entre les différentes couches crustales pourraient aussi jouer un rôle non négligeable sur l'arrêt de l'ascension des dykes (*Menand*, 2011). En effet, des expériences réalisées par *Kavanagh et al.* (2006) ont montré que la propagation d'un dyke peut être arrêtée quand celui-ci rencontre une interface qui sépare un milieu plus rigide surplombant un milieu moins rigide (Figure 1.2). Le dyke arrête ainsi son ascension verticale et s'étale horizontalement juste en dessous de la couche de rigidité plus élevée. Ce mécanisme serait d'autant plus efficace que le contraste de rigidité est important (*Kavanagh et al.*, 2006).

Finalement, les contraintes, locales ou globales, peuvent aussi dévier la trajectoire d'un dyke et influencer les trajets des magmas au sein de la croûte. En effet, de nombreuses études ont montrés que les chenaux par lesquels se propage le magma tendent à s'orienter perpendiculairement à la contrainte minimum de compression (*Anderson*, 1951; *Watanabe et al.*, 2002). Les dykes ont donc tendance à exister dans des situations dans lesquelles la contrainte

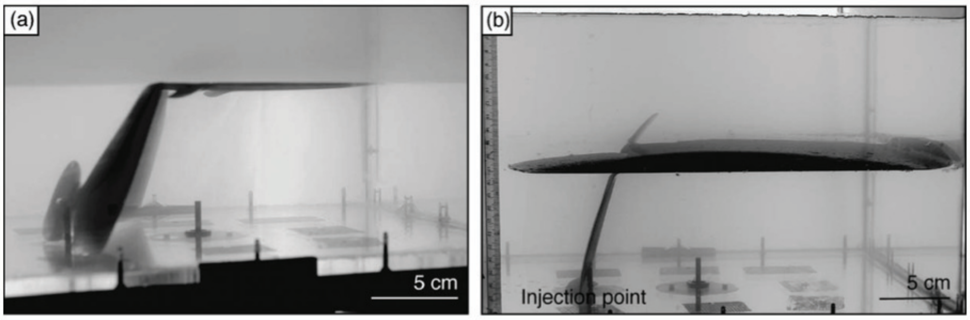

Figure 1.2: a) Photographie de deux des expériences réalisées par *Kavanagh et al.* (2006) sur le comportement d'un dyke à l'interface entre deux milieux de rigidité différente. a) Le contraste de rigidité est très important et le dyke s'étale sous la couche de rigidité importante. b) Le contraste de rigidité est plus faible et, tout en s'étalant en dessous de la couche de rigidité supérieure, le dyke continue sa progression dans le milieu plus rigide.

minimum de compression est horizontales et à être dévié, voir même s'étaler horizontalement si la contrainte minimum de compression devient verticale (*Pinel and Jaupart*, 2000, 2004; *Maccaferri et al.*, 2014). *Menand et al.* (2010) ont cependant montré que l'échelle de longueur sur laquelle le dyke répondait à cette évolution du champ de contrainte dépendait de la flotabilité du magma. Notamment, à l'échelle de la croûte, la propension d'un champ de contrainte à dévier un dyke devient importante seulement si la contrainte de compression domine sur la flotabilité du magma (*Menand et al.*, 2010).

En conclusion, même si ces différents facteurs jouent un rôle sur le contrôle des trajets des magmas au sein de la croûte, la densité relative du magma et de la roche encaissante et donc l'existence d'une zone de flottabilité neutre est certainement le facteur le plus déterminant dans la mise en place d'intrusions magmatiques. Le magmatisme intrusif et la question du stockage des magmas, est donc de manière générale étroitement lié à la structure en densité de la croûte elle-même.

1.2 Importance et multiples visages du magmatisme intrusif

1.2.1 Magmatisme intrusif sur Terre

Sur Terre, la composition de la croûte, et donc sa densité, est bimodale. Au niveau des océans, la croûte océanique présente une nature essentiellement basaltique avec une densité moyenne proche de 2900 kg m^{-3}. Elle est formée continuellement au niveau des dorsales océaniques et recyclée, environ 200 Ma d'année plus tard au niveau des zones de subduction. Elle est épaisse en moyenne de 6 km et couvre à elle seule 70% de la surface du globe. Au contraire, la croûte continentale, qui occupe les 30% restants, présente une composition plus évoluée et globalement andésitique avec une densité moyenne plus proche de 2700 kg m^{-3}. Elle est beaucoup plus vieille que la croûte océanique et est âgée en moyenne de 2.5 Ga, avec certaines roches d'environ 4 Ga d'années. Elle est aussi beaucoup plus épaisse que la croûte continentale; son épaisseur moyenne est de 35 km et peut excéder les 70 kilomètres sous certaines chaînes de montagnes comme l'Himalaya.

De par sa densité relativement basse, en particulier au niveau des continents, la croûte constitue un filtre efficace à la remontée des magmas en surface qui sont donc préférentiellement stockés en profondeur sous forme d'intrusions magmatiques. *Crisp* (1984) et *White et al.* (2006) estiment en effet que les volumes de lave extrudée à la surface sont relativement faibles en comparaison des volumes mis en place au sein de la croûte terrestre, i.e. 5 fois plus faibles en contexte océanique et jusqu'à 10 fois plus faibles en contexte continental. Le magmatisme intrusif apparaît donc comme un processus essentiel dans la formation de la croûte. Sur Terre, les mouvements tectoniques en son sein ainsi que l'érosion ont permis d'exposer certaines de ces intrusions à la surface. Outre leur taille, qui peut varier de quelques mètres à des centaines de kilomètres, la morphologie de ces intrusions présente une grande variabilité.

Les batholites sont de loin les plus imposants représentants de cette famille d'intrusions magmatiques se mettant en place au sein de la partie fragile de la croûte. Ils peuvent atteindre jusqu'à quelques kilomètres d'épaisseur et s'étendre sur des centaines de kilomètres. Par exemple, le batholite de la Sierra Nevada est une intrusion granitique qui s'étend sur presque la totalité de la Sierra Nevada en Californie. Des données géochronologiques sur certains de ces batholites ont montré que leur mise en place peut s'échelonner sur quelques millions d'années, un temps beaucoup plus grand que les temps raisonnables pour le refroidissement d'une chambre magmatique dans la partie fragile de la croûte (*Glazner et al.*, 2004). En effet, il est maintenant clair que la mise en place de ces gigantesques volumes de magmas se fait par incréments successifs de petits volumes de magma se solidifiant lors de leur mise en place sur de longues échelles de temps, de 10^5 à 10^6 années (*Petford et al.*, 2000; *Glazner et al.*, 2004). Dans cette thèse, nous nous focalisons sur les mécanismes de formation et de mise en place de volumes intermédiaires de magma dans la partie fragile de la croûte continentale, à des profondeurs inférieures à 10 km.

Des études géologiques de terrain ont montré la présence de quatre grandes familles d'intrusions magmatiques de taille intermédiaire à faible profondeur.

Deux de ces familles, les dykes et les bysmalites, sont discordantes, c'est-à-dire qu'elles se mettent en place perpendiculairement à la stratification naturelle de l'encaissant et deux autres, les sills et les laccolites, sont concordantes, i.e. elles se mettent en place parallèlement aux couches géologiques.

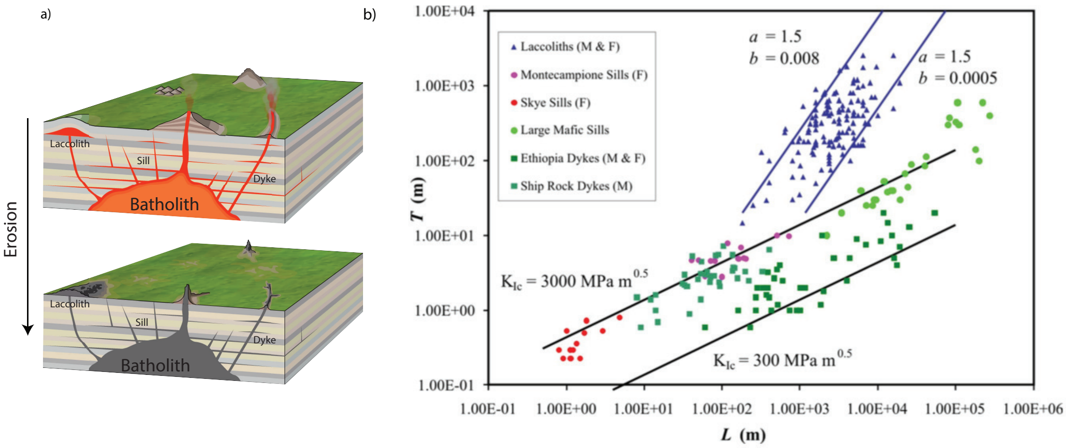

Figure 1.3: a) Différentes formes du magmatisme intrusif: batholite, dyke, sill et laccolite. Dimensions typiques pour des laccolites, dyke et sill de compositions et d'origines différentes d'après de *Cruden et al.* (2012).

- Les dykes, par lesquels remontent le magma à travers la lithosphère sont discordants et caractérisés par de faibles rapports d'aspects, de 0.01 – 0.0001 (Figure 1.3, 1.7 a) (*Rubin*, 1995; *Schultz et al.*, 2008; *Kavanagh and Sparks*, 2011). Leur épaisseur peut varier de quelques mètres à quelques centaines de mètres (*Walker*, 1989; *Krumbholz et al.*, 2014), cependant, l'épaisseur moyenne est de quelques dizaines de mètres. Les dykes de compositions felsiques sont généralement plus épais et moins longs que leurs équivalents mafiques (*Rubin*, 1995).

- Les sills, à la différence des dykes, sont concordants (Figure 1.3, 1.7 b,f). Ils se mettent en place le long de discontinuités ou de failles préexistantes, à la jonction entre deux couches sédimentaires par exemple. Les sills aux dimensions les plus importantes répertoriés sont mafiques et peuvent attendre jusqu'à 100 km pour des épaisseurs de plusieurs centaines de mètres (*Cruden et al.*, 2012). Leurs homologues felsiques, plus rares, sont souvent de dimensions plus faibles.

- Les laccolites ont étés décrit premièrement par *Gilbert* (1877) suite à son étude géologique des Henry Mountains, dans l'Utah aux États-Unis

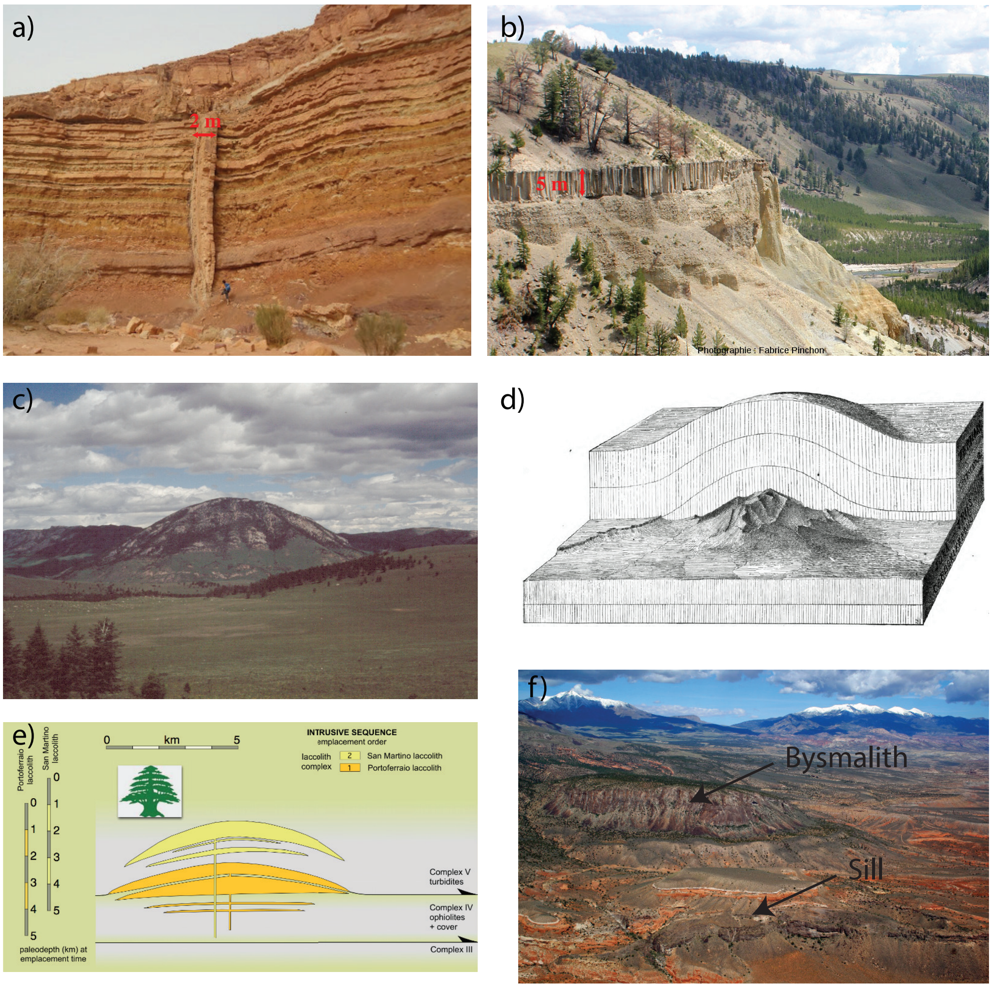

Figure 1.4: a) Dyke traversant des couches sédimentaires dans le Makhtesh Ramon, Israël; b) Sill basaltique au sein de sédiments, vallée de la Yellowstone River, parc National du Yellowstone (USA). Photographie de Fabrice Pinchon. c) Laccolite à l'érosion dans le Montana d) Schéma de l'emplacement d'un laccolite réalisé par *Gilbert* (1877). e) Schéma simplifié de la structure en arbre de noel d'un complexe de laccolite sur l'île d'Elbe, en Italie, étudiée par *Rocchi et al.* (2010). f) Intrusions à l'érosion aux alentour de la montagne Hillers, dans les Henry Mountains. On peut distinguer le Black Mesa Bysmalite au centre et le Maiden Creek sill en dessous. Photographie de Jack Share

(Figure 1.7 c, d, e). Ils se mettent en place principalement par flexion des couches sédimentaires sus-jacentes, ce qui leur donne une forme de dôme caractéristique. Certains d'entre eux peuvent aussi être caractérisés par une forme un peu plus aplatie au centre (*Koch et al.*, 1981). *Corry* (1988) a répertorié à peu près 900 laccolites, principalement dans le nord des États-Unis. Leurs épaisseurs varient de quelques dizaines à quelques centaines de mètres et leurs rayons peuvent atteindre quelques kilomètres pour les plus gros (Figure 1.3 b). Ces laccolites se sont parfois mis en place les uns sur les autres formant une structure en forme de sapin de Noël (*Corry*, 1988). Cette géométrie est aussi observée sur l'île d'Elbe, en Italie, où un complexe de neuf laccolites, exceptionnellement bien conservé, a été étudié en détail par *Rocchi et al.* (2002).

- Les bysmalites sont d'imposants volumes cylindriques, préférentiellement composés de roche granitique, discordants (Figure 1.7 f). Ils sont notamment bordés par d'importantes failles presque verticales et peuvent atteindre quelques centaines de mètres d'épaisseur (*Johnson and Pollard*, 1973). Un exemple typique de ce type d'intrusion est le Black Mesa Bysmalite dans les Henry Mountains (200 m d'épaisseur et 1 km de large (*Morgan et al.*, 2008)).

À l'instar des batholites, de nombreuses observations de terrains proposent que ces intrusions de taille moyenne se forment aussi par incréments successifs de petits volumes de magma (*Habert and De Saint-Blanquat*, 2004; *Horsman et al.*, 2005; *Morgan et al.*, 2008) (Figure 1.5). Cependant, les mêmes études montrent aussi que ces intrusions se forment nécessairement sur de petites échelles de temps, des échelles assez faibles pour pouvoir garder un corps chaud et liquide des premières étapes du processus d'intrusion à la solidification. Au niveau du bysmalite de Black Mesa par exemple (Figure 1.7 f), *Habert and De Saint-Blanquat* (2004) ont montré l'absence de discontinuités entre les différentes couches ainsi que l'absence de métamorphisme important dans l'encaissant indiquant un temps de mise en place de moins de 100 ans. L'absence de discontinuité au sein des différents laccolites sur l'île d'Elbe supporte aussi leur formation rapide, i.e. à la suite d'une seule injection où de plusieurs injections sur un temps assez court pour que les magmas des différentes injections coalescent (*Roni et al.*, 2014).

1.2.2 Magmatisme intrusif sur la Lune

La lune s'est probablement formée suite à l'impact d'un corps de la taille de Mars sur la proto-Terre une centaine de millions d'années après la formation de la Terre, le disque de débris produit se réaccrétant ensuite en moins d'un

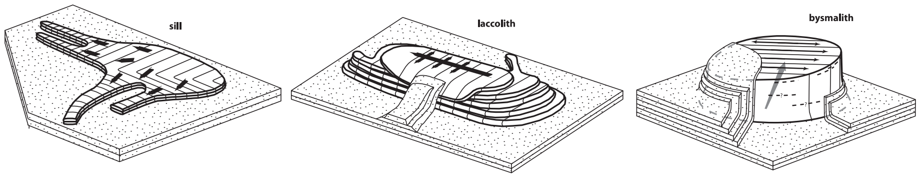

Figure 1.5: Ces diagrammes, réalisés par *Horsman et al.* (2009), montrent la structure verticale en couche de trois intrusions à l'érosion dans les Henry Mountains. De gauche à droite: le Maiden Creek Sill (Figure 1.7 f), le Trachyte Mesa Laccolite et le Black Mesa Bysmalite (Figure 1.7 f).

millier d'années pour former notre satellite (*Mizutani et al.*, 1972; *Cameron and Benz*, 1991; *Canup and Asphaug*, 2001; *Canup*, 2012). Compte tenu des quantités importantes d'énergie libérée durant le processus d'accrétion, on considère aujourd'hui que la Lune était partiellement fondue, sur une épaisseur encore débattue, suite à sa formation (*Elkins-Tanton et al.*, 2011). Le refroidissement et la lente cristallisation fractionnée de l'océan de magma lunaire aurait ensuite conduit à la formation d'une croûte primaire par flottaison des minéraux légers de plagioclase (en particulier du pôle calcique, l'anorthite) à la surface de l'océan de magma tandis que les éléments les plus incompatibles, en particulier les éléments producteurs de chaleur, se seraient concentrés dans les derniers liquides magmatiques résiduels entre la croûte et le manteau, formé, lui, principalement de cumulats d'olivine et de pyroxène (Figure 1.6).

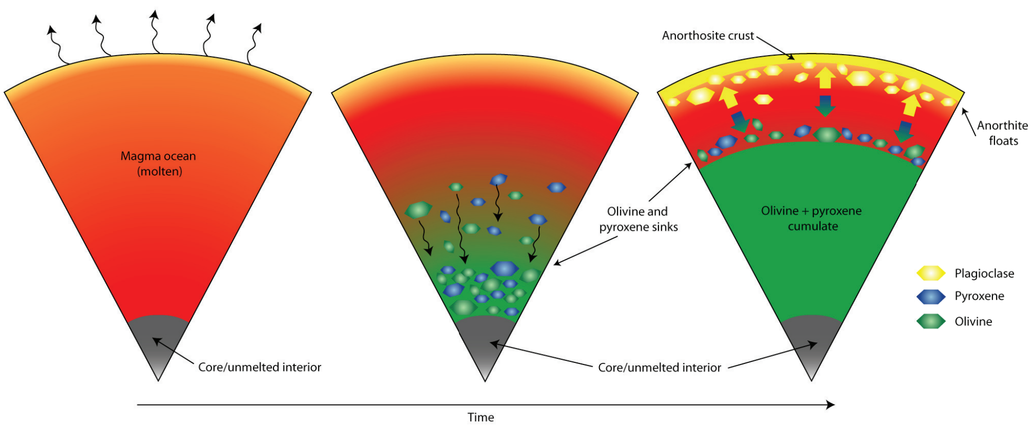

Figure 1.6: Cristallisation fractionnée de l'océan de magma et formation de la croûte primaire composé d'anorthosite. Source: LPI

Etant donné sa composition et la porosité résultante de 4 milliards d'années de bombardement météoritiques, la densité de la croûte lunaire est particulièrement faible (*Huang and Wieczorek*, 2012; *Han et al.*, 2014). D'après les dernières estimations, rendues possibles grâce aux mesures du champ de gravité d'une résolution sans précédent obtenues par la mission GRAIL de la NASA, la densité moyenne au niveau des terres hautes serait de 2550 kg m^{-3} (*Wieczorek et al.*, 2013). Ces données ont aussi permis de réévaluer à la baisse l'épaisseur de la crôute à entre 34 et 44 km en moyenne avec une tendance à être moins épaisse au niveau des mers lunaires.

La faible densité de sa crôute et son épaisseur non négligeable ont certainement joué un rôle important sur le volcanisme lunaire. En effet, les magmas formées par fusion du manteau lunaire sont particulièrement dense, de l'ordre de 3000 kg m^{-3} (*Kiefer et al.*, 2012) en lien avec leur composition basaltique riche en oxydes métalliques, en particulier en oxyde de Fer FeO et de Titane T_iO_2. Ainsi, la croûte primaire formée par cristallisation de l'océan de magma étant très légère, elle a sans aucun doute aussi été un filtre puissant à l'éruption des magmas sur la lune, leur flottabilité ne leur permettant pas d'être transporté jusqu'à la surface.

Wieczorek et al. (2001) ont ainsi confirmé que le volcanisme à la surface est généralement lié à l'extraction d'une partie de cette crôute de faible densité, comme c'est la cas par exemple des mers lunaires qui se sont mises en place au sein de larges bassins d'impacts. *Head and Wilson* (1992) ont estimé à 50 fois plus importants les volumes de magma mis en place en profondeur que les volumes éruptés en surface. Cependant, bien que ce rapport puisse donner de précieuses indications sur l'évolution thermique et magmatique de la lune elle-même, il est de fait très peu contraint et la part intrusive du magmatisme lunaire est encore mal connue. La détection des déformations de surface induites par la mise en place d'intrusions magmatiques au sein de la croûte apparaît donc comme une première étape visant à la meilleur caractérisation du magmatisme intrusif lunaire.

Deux manifestations principales à la surface de la lune ont été proposées comme potentiellement résultantes de la mise en place d'intrusions magmatiques au sein de la croûte lunaire: les dômes à faible pente et les cratères à sol fracturé.

- Les dômes à faible pente sont localisés en bordure ou dans les mers lunaires, principalement sur la face visible (Figure 1.8 a, b). Une quinzaine de ces dômes, possiblement d'origine intrusive, ont été récemment décrit par *Wöhler et al.* (2007). Bien que leur morphologie s'apparente à des laccolites terrestres, ils sont de manière générale beaucoup plus étalés que ceux sur Terre; pour une même épaisseur, l'équivalent lunaire peut

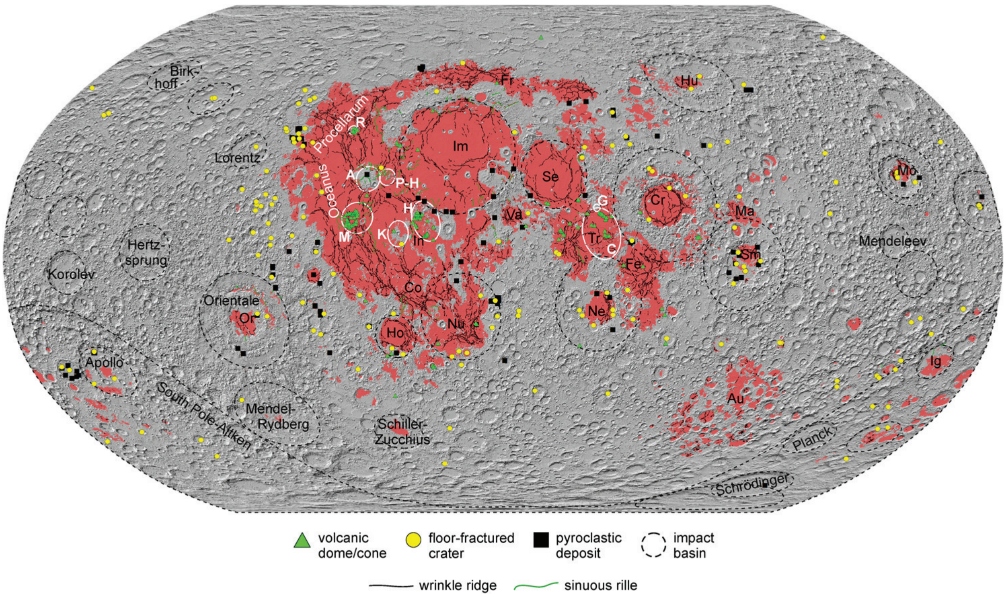

Figure 1.7: Distribution des principales structures d'origines volcaniques à la surface lunaire. Les mers lunaires apparaissent en rouge. Les bassins d'impact supérieurs à 300 km apparaissent en pointillé. Les cratères à sol fracturé sont marqués d'un triangle jaune, les dépôt pyroclastiques d'un carré noir, les dômes et cônes avec un triangle vert et les sineous rilles à l'aide d'une ligne verte. Les abréviations utilisées sont: Au, Australe; Co, Cognitum; Cr, Crisium; Fe, Fecundidatis; Fr, Frigoris; Ho, Humorum; Hu, Humboldtianum; Ig, Ingenii; Im, Imbrium; In, Insularum; Ma, Marginis; Mo, Moscoviense; Ne, Nectaris; Nu, Nubium; Or, Orientale, Se, Serenitatis; Sm, Smythii; Tr, Tranquillitatis; Va, Vaporum. Source: *Platz et al.* (2015)

ainsi être deux fois plus large que son homologue terrestre.

- Les cratères à sol fracturé sont des cratères d'impacts ayant subi des déformations suite à leur formation. À peu près 200 de ces cratères ont été répertorié par *Schultz* (1976), principalement autour des mers lunaires (Figure 1.8 c, d, e, f). La principale caractéristique de ces cratères est leur faible profondeur par rapport à celles des cratères non déformés. En effet, certains cratères au sol fracturé peuvent être jusqu'à 2 km moins profonds que leurs homologues non déformés. Leur sol, soit en forme de dôme, soit plat séparé des bords du cratère par un imposant fossé circulaire, est systématiquement caractérisé par d'importants réseaux de fractures radiales, concentriques ou encore pentagonales (Figure 1.8 c, d, e, f). Basé sur leur profondeur, topographie et niveau de déformation,

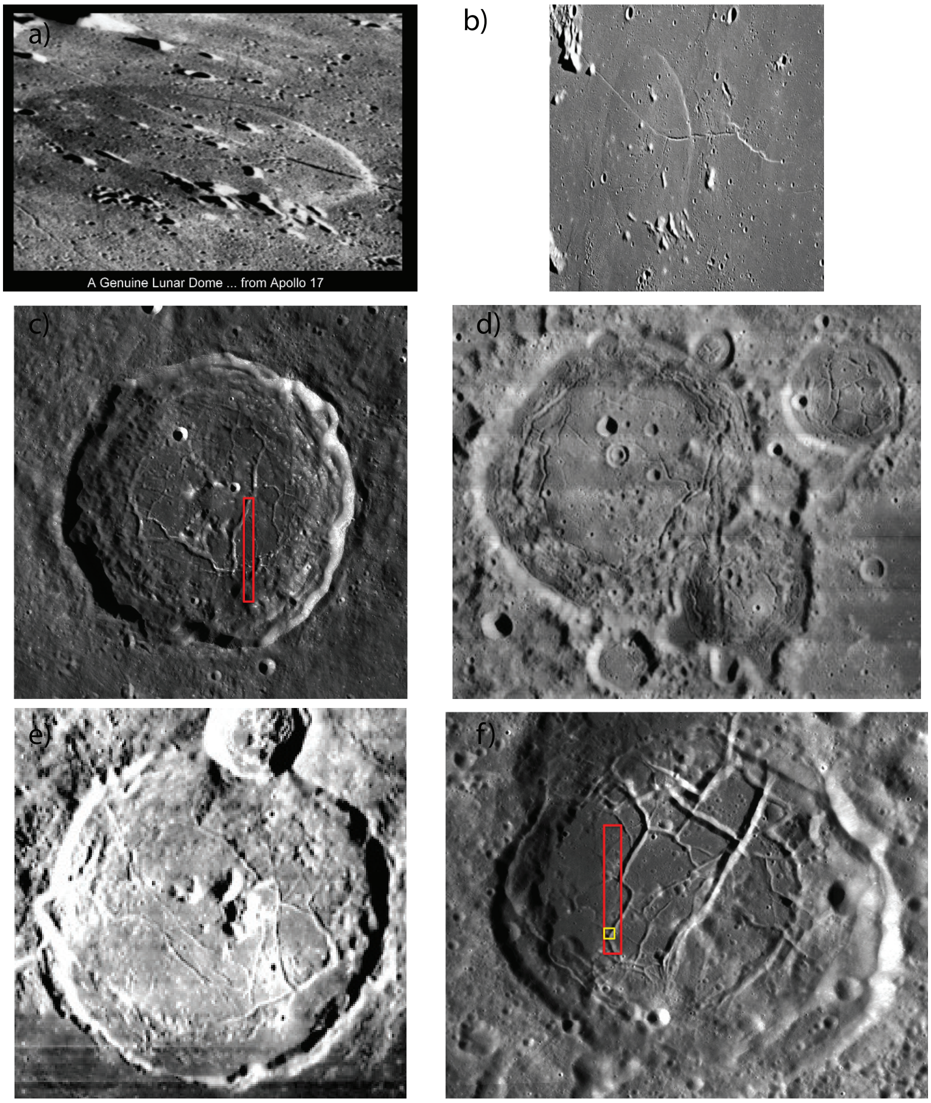

Figure 1.8: a) Dome lunaire, photo par Appolo 17 b) Apollo 15 orbital image AS15-91-12372, vue oblique du dôme Valentine. c) Cratère au sol fracture Atlas (Classe 1). d) Cratère au sol fracturé Lavoisier (Classe 5). e) Cratère au sol fracturé Gassendi (Classe 3). f) Cratère au sol fracturé Komarov (Classe 5). Photo extraite de *Lunar Orbiter Photographic Atlas of the Moon, NASA*

Schultz (1976) a postulé l'existence de six grandes classes de déformation. La proximité de ces cratères avec les mers lunaires, ainsi que la présence de produits volcaniques au sein de certains d'entre eux, suggère qu'ils ont été déformés suite à la mise en place de magma en profondeur sous leur sol.

1.3 Caractérisation de la mise en place d'une intrusion magmatique à faible profondeur

1.3.1 Modèle statique de déformation d'une couche élastique

Bien que la morphologie et les volumes de magma puissent être récupérés, à partir d'observations directes ou de méthodes de prospection géophysique sur Terre ou via les déformations induites à la surface des autres corps telluriques du système solaire, ces informations seules ne donnent que peu d'indications sur les mécanismes de mise en place de ces intrusions magmatiques. De nombreux travaux ont ainsi été centrés sur la modélisation des processus donnant lieu à ces déformations, dans le but de mieux comprendre le mécanisme d'intrusion d'une part, mais aussi, de déduire des observations des informations sur le magma, les paramètres mécaniques de l'encaissant ou encore la profondeur de l'intrusion au moment de sa mise en place.

La propagation d'un dyke dans un milieu élastique a été beaucoup étudiée (*Lister and Kerr*, 1991; *Rubin*, 1995). En particulier, *Lister and Kerr* (1991) ont montré que, à l'exception de la tête du dyke où les contraintes élastiques induites par les roches encaissantes jouent un rôle important, la dynamique du magma au sein du dyke est contrôlée par un équilibre entre la flottabilité et les pertes de charge associées aux frottements visqueux sur les parois du conduit. On a vu qu'un dyke peut se transformer en sill si celui-ci rencontre sa zone de flottabilité neutre. Bien que la dynamique des dykes et des sills soit comparable à forte profondeur (*Lister and Kerr*, 1991; *Cruden et al.*, 2012), à faible profondeur, la forme des laccolites suppose que les intrusions magmatiques se mettent en place principalement par flexion des couches sus-jacentes (*Johnson and Pollard*, 1973). Une pratique, courante en science planétaire, consiste à modéliser ces laccolites par la déformation d'une plaque mince élastique, de longueur fixée et égale à la taille de l'intrusion, soumise à une pression donnée (*Pollard and Johnson*, 1973). Dans ces modèles statiques, cette pression, donnant lieu à la déformation, est soit prise constante sur la taille de l'intrusion et égale au poids du magma (*Pollard and Johnson*, 1973; *Wichman and Schultz*, 1996; *Jozwiak et al.*, 2012), soit imposée suivant un profil décrivant la perte de charge associée à un écoulement visqueux (*Kerr and Pollard*, 1998; *Wöhler et al.*, 2009). Cependant, dans aucun des cas, cette pression n'est reliée aux paramètres de l'écoulement lui-même, i.e. volume ou taux d'injection. De plus, ces modèles ne fournissent pas un cadre théorique suffisant à la compréhension de la dynamique de l'intrusion et sont donc incapables d'expliquer la diversité des formes et des tailles observées. Enfin, ils considèrent la flexion de la couche sus-jacente comme unique pression motrice à l'écoulement, sans considérer le poids du magma lui-même, qui doit pourtant nécessairement jouer un rôle sur la mise en place de l'intrusion.

1.3.2 Inférence sur la dynamique à partir de la géométrie

En l'absence d'un modèle dynamique, la géométrie des intrusions répertoriées a souvent été utilisée pour en déduire des indications sur les processus de mise en place et de croissance de ces intrusions. Ainsi, en utilisant les données répertoriées sur les laccolites par *Corry* (1988), *McCaffrey and Petford* (1997) proposent une loi de puissance empirique pour l'épaisseur des intrusions h_0 en fonction de leur longueur R, $h_0 = bR^a$ ou a est l'exposant de la loi de puissance et b une constante. Un exposant supérieur à l'unité indique que l'intrusion croit préférentiellement en s'épaississant tandis qu'un exposant inférieur à l'unité indique qu'elle croit plutôt par étalement.

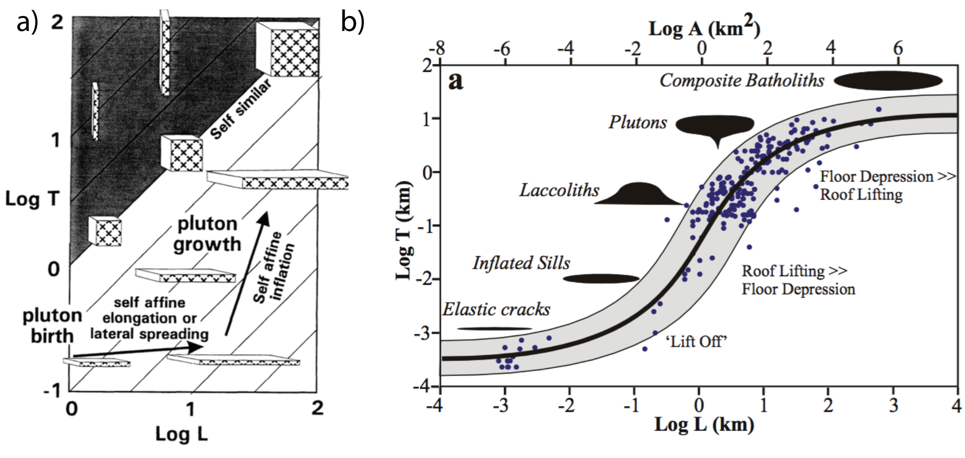

Figure 1.9: a) Schéma de la formation des laccolites en deux étapes par *McCaffrey and Petford* (1997). Épaisseurs en fonction de leur longueur de différents types d'intrusions magmatiques à différentes locations. Figure extraite de *Cruden et al.* (2012).

Les laccolites répertoriées par *Corry* (1988) montrent un exposant $a < 1$

(0.88 ± 0.1), interprété comme reflétant l'étalement de l'intrusion sur une certaine distance sous forme d'un sill avant son épaississement (Figure 1.9). Ce modèle est cohérent avec le modèle en deux étapes couramment accepté pour la mise en place des laccolites (*Johnson and Pollard*, 1973; *McCaffrey and Petford*, 1997). Premièrement, le magma s'étale latéralement au niveau de sa zone de flottabilité neutre , i.e. $a < 1$ jusqu'à ce qu'un sill, caractérisé par un rapport d'aspect assez large, soit formé. Ensuite, lorsque le sill est assez large, il s'épaissit par flexion des couches sus-jacentes pour former un laccolite caractérisé par une valeur de $a > 1$ (*Johnson and Pollard*, 1973; *Koch et al.*, 1981). Si la roche sus-jacente est soumise à des contraintes trop importantes, des failles se forment au niveau des bords du sill et celui-ci s'épaissit uniformément sur toute sa surface formant un bysmalite (*Corry*, 1988). Dans la continuité de l'étude de *McCaffrey and Petford* (1997), *Rocchi et al.* (2002) ont réalisé une étude détaillée du complexe intrusif de l'île d'Elbe en Italie et ont trouvé un exposant a supérieur à l'unité, i.e. ~ 1.5, interprété comme étant la preuve de l'existence d'une phase dominée par l'épaississement de l'intrusion dans la croissance de ces laccolites.

Des modèles plus récents conçoivent plutôt la formation des laccolites par empilements successifs de sills, de grand rapport d'aspect, plutôt que par l'injection d'un seul volume de magma fini à un temps donné (*Menand*, 2011). En effet, ces modèles sont étayés par les expériences de *Kavanagh et al.* (2006) (Section 1.1.3) où il est montré qu'un sill peut se mettre en place à l'interface entre deux couches de rigidité différentes, la rigidité de la couche sus-jacente étant plus importante que celle de la couche sous-jacente. Dès lors, la mise en place d'un sill, en refroidissant, procure un environnement favorable à la mise en place d'un nouveau sill, soit au-dessus si la rigidité du sill solidifié est inférieure à celle de la roche sus-jacente, soit en dessous dans le cas contraire. Ce modèle de croissance a aussi été suggéré par de récentes études structurales et stratigraphiques, notamment au niveau des intrusions de tailles intermédiaires dans les Henry Mountains (*Horsman et al.*, 2005; *Morgan et al.*, 2008; *Horsman et al.*, 2009; *Menand*, 2011). Ce modèle, à la différence des modèles statiques exposés plus haut, a aussi l'avantage de pouvoir expliquer la structure aplatie au niveau du centre de certains laccolites (*Morgan et al.*, 2008). Cependant, ce modèle ne fournit pas de mécanisme ni ne permet d'expliquer l'origine de la loi de puissance caractéristique de la géométrie de ces intrusions. De plus, il ne permet pas de relier la géométrie finale de l'intrusion aux propriétés physiques de l'écoulement (volume, taux d'injection).

Cruden and McCaffrey (2002) ont réuni des données sur une plus grande plage de longueurs, de petits filons de quelques dizaines de mètres à des batholites de quelques centaines de kilomètres (Figure 1.9) et proposent que l'épaisseur en fonction de la longueur des intrusions magmatiques forme une distribution en forme de sigmoïde (dans une échelle logarithmique), avec une pente maximum de 1.5 caractéristique des laccolites. Cependant, aucune théorie sous-jacente ne soutient cette observation. De plus, les données de *Cruden et al.* (2012) sur les larges sills mafiques contredisent cette affirmation (Figure 1.3).

1.3.3 Discussion

Bien que de nombreux modèles ont été proposés pour essayer de rendre compte des observations, peu d'entre eux s'intéressent à la dynamique de l'intrusion qui permettrait cependant de relier la morphologie de ces intrusions aux propriétés physiques de l'écoulement (volume ou taux d'injection). Afin de comprendre la morphologie des intrusions peu profondes, il apparaît donc important de s'intéresser à la dynamique d'un tel écoulement.

Michaut (2011) a ainsi proposé un modèle théorique d'étalement d'un magma visqueux sous une couche élastique d'épaisseur contante continuellement nourrie par un conduit vertical en son centre. Ce modèle diffère des précédents par sa capacité à traiter la dynamique même de l'intrusion ainsi que le poids du magma comme un moteur de l'écoulement. Les résultats et la capacité de ce modèle à reproduire les observations sont discutés dans le chapitre suivant.

Chapter 2

Isoviscous elastic-plated gravity current model for shallow magmatic intrusion

Contents

Michaut (2011) proposed a model for the spreading of a shallow depth intermediate-size intrusion, in which magma is continuously injected at the center and is accommodated by the bending of the overlying strata. In particular, the model differs from previous ones by considering both the dynamics of the emplacement itself, in a sense that the radius is self-consistently determined, and the driving force associated with the magma weight. Both were neglected in previous models. In the original paper from *Michaut* (2011), the model was derived in both cartesian and axisymmetric geometry and the results were presented in $2D$. A similar model in $2D$ with an additional fracture criterion at the tip of the intrusion has been derived by *Bunger and Cruden* (2011) and *Hewitt et al.* (2014) discussed more precisely the dynamics at the contact line and the case of an elastic-plated gravity current spreading over an inclined plane. In this chapter, we present a summary of the model and the results for the spreading of an isoviscous elastic-plated gravity current over a rigid horizontal surface in an axisymmetrical geometry. Results in this geometry have been thoroughly studied by *Lister et al.* (2013) and this will constitute the reference for more elaborate models in the manuscript.

2.1 Theoretical model

The model considers an isoviscous elastic-plated gravity current, i.e. an isoviscous fluid of viscosity η_h and density ρ_m spreading beneath a thin elastic sheet of thickness d_c and above a semi infinite rigid layer (*Michaut*, 2011; *Bunger and Cruden*, 2011) (Figure 2.1). The fluid is injected continuously at the base and center of the current at a rate Q_0 through a cylindrical conduit of diameter a.

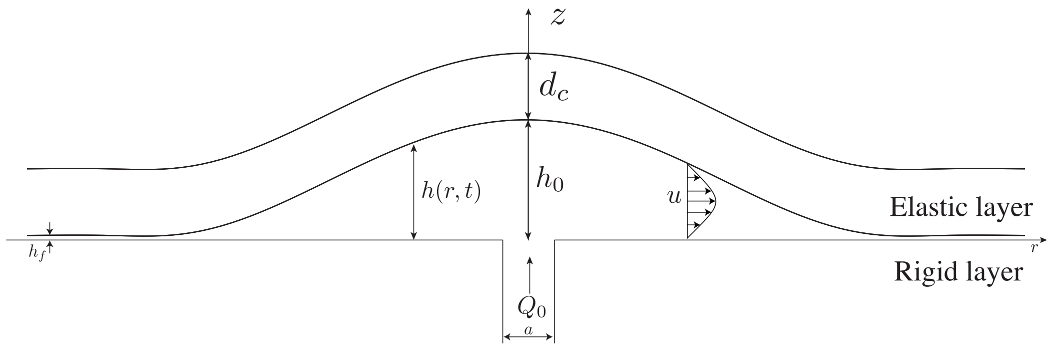

Figure 2.1: Model geometry and parameters.

2.1.1 Governing equation

Driving pressure

The intrusion develops over a length scale Λ that is much larger than its thickness H ($\varepsilon = H/\Lambda << 1$). In the laminar regime and in axisymmetrical coordinates (r,z), the Navier-Stokes equations within the lubrication assumption are

$$-\frac{\partial P}{\partial r} + \frac{\partial}{\partial z}\left(\eta_h \frac{\partial u}{\partial z}\right) = 0 \tag{2.1}$$

$$-\frac{\partial P}{\partial z} - \rho_m g = 0 \tag{2.2}$$

where $u(r,z,t)$ is the radial velocity, g is the standard acceleration due to gravity and $P(r,z,t)$ is the pressure within the fluid. Integration of (2.2) thus gives the total pressure $P(r,z,t)$ within the flow. When the vertical deflection $h(r,t)$ of the upper elastic layer is small compared to its thickness d_c, i.e $h << d_c$, we can neglect stretching of the upper layer and only consider bending stresses. Therefore, the total pressure $P(r,z,t)$ at a level z in the intrusion is the sum of four contributions: the weight of the magma and of the upper layer, the bending pressure P_b and the atmospheric pressure P_0

$$P = \rho_m g(h - z) + \rho_r g d_c + P_b + P_0 \tag{2.3}$$

where $h(r,t)$ is the intrusion thickness and ρ_r the density of the surrounding rocks. The bending pressure is given by the force per unit area that is necessary for a vertical displacement h of the thin elastic plate (*Turcotte and Schubert*, 1982)

$$P_d = D\nabla_r^4 h \tag{2.4}$$

where D is the flexural rigidity of the thin elastic layer, that depends on the Young's modulus E, Poisson's ratio ν^* and on the elastic layer thickness d_c as $D = Ed_c^3/\left(12(1-\nu^{*2})\right)$.

Velocity field

At the contact with the elastic sheet $z = h(r,t)$, the no-slip boundary condition hold; the tangential velocity is zero and the normal velocity is the rate of height change ($\partial h/\partial t$). With $\vec{n}$ the normal to the surface and $\vec{t}$ the tangent, we have

$$\vec{n} \cdot \vec{u} = \frac{\partial h}{\partial t} \tag{2.5}$$

$$\vec{t} \cdot \vec{u} = 0 \tag{2.6}$$

The tangent vector is $\vec{t} = (1, \partial h/\partial r)$. However, within the lubrication assumption, the vertical component of the tangent vector scales as ε and thus, is negligible compared to the radial component. Therefore, the boundary condition (2.6) reduces to $u(r, z = h, t) = 0$. At the base of the flow, the same boundary condition holds and $u(r, z = 0, t) = 0$.

Equation (2.1) is integrated twice as a function of z using these boundary conditions and the horizontal velocity is

$$u(r,z,t) = \frac{1}{2\eta_h}\frac{\partial P}{\partial r}\left(z^2 - hz\right) \tag{2.7}$$

Injection rate

Assuming a Poiseuille flow within the cylindrical feeding conduit, the vertical injection velocity $w_i(r,t)$ within the conduit reads

$$w_i = \begin{cases} \frac{\Delta P^*}{4\eta_h Z_c}(\frac{a^2}{4} - r^2) & r \leq \frac{a}{2} \\ 0 & r > \frac{a}{2} \end{cases} \tag{2.8}$$

and depends on the effective overpressure $\Delta P^*(t)$ driving the flow. The effective overpressure $\Delta P^*(t)$ and then the injection rate $Q(t)$ decrease as the weight of the intrusion increases at the center and read

$$\Delta P^*(t) = \Delta P - \rho_m g h_0(t) \tag{2.9}$$

$$Q(t) = Q_0(1 - \frac{\rho_m g h_0(t)}{\Delta P}) \tag{2.10}$$

where ΔP is the initial overpressure or the overpressure at the base of the dyke ($z = -Z_c$) and $Q_0 = (\pi \Delta P a^4) / (128\eta_h Z_c)$. In (2.9), the bending pressure at the center, which scales as $\mathrm{D}h_0(t)/R(t)^4$ where $R(t)$ is the current radius, has been neglected. Although it tends to infinity at the initiation of the flow, it rapidly vanishes as the current spreads and the hydrostatic pressure $\rho_m g h_0$ becomes the main contribution to the pressure at the center. In addition, the model assumes a large aspect ratio for the flow and does not consider the initiation of the flow itself.

Later in this thesis, we will also consider a constant flux injection where $\Delta P^* = \Delta P$ and the injection rate is constant, i.e. $Q(t) = Q_0$. Implicitely, it thus assumes that $\Delta P \gg \rho_m g h_0$.

Mass conservation

The fluid is assumed incompressible and a global statement of mass conservation gives

$$\frac{\partial h}{\partial t} + \frac{1}{r}\frac{\partial}{\partial r}\left(r\int_0^h u dz\right) = w_i. \tag{2.11}$$

Injecting (2.7) into (2.11), we find that the equation for the evolution of the thickness in time and space reads

$$\frac{\partial h}{\partial t} = \frac{\rho_m g}{12\eta_h r}\frac{\partial}{\partial r}\left(rh^3\frac{\partial h}{\partial r}\right) + \frac{D}{12\eta_h r}\left(rh^3\frac{\partial}{\partial r}\nabla_r^4 h\right) + w_i. \tag{2.12}$$

It is composed of three different terms on the right hand side. The first term represents gravitational spreading, i.e. spreading of the current under its own weight. The second term represents the squeezing of the flow by the upper elastic layer. Both term are negative and induces spreading. The last term represents fluid injection and is positive.

2.1.2 Dimensionless equations

Equation (2.12) is nondimensionalized using a horizontal scale Λ, a vertical scale H and a time scale τ given by

$$\Lambda = \left(\frac{D}{\rho_m g}\right)^{1/4} \tag{2.13}$$

$$H = \left(\frac{12\eta_h Q_0}{\rho_m g \pi}\right)^{\frac{1}{4}} \tag{2.14}$$

$$\tau = \frac{\pi\Lambda^2 H}{Q_0} \tag{2.15}$$

in which scales are chosen such that $Q_0 = \pi\Lambda^2 H/\tau$. The length scale Λ represents the flexural wavelength of the upper elastic layer, i.e. the length scale at which bending stresses and gravity equally contribute to flow. The height scale H is the thickness of a typical gravity current and the time scale τ is the characteristic time to fill up a cylindrical flow of radius Λ and thickness H at constant rate Q_0. In addition, we can define a horizontal velocity scale $U = \Lambda/\tau = (\rho_m g H^3)/(12\eta_h\Lambda)$ and a pressure scale $\rho_m g H$.

The dimensionless equation is

$$\begin{aligned}\frac{\partial h}{\partial t} &= \frac{1}{r}\frac{\partial}{\partial r}\left(rh^3\frac{\partial h}{\partial r}\right) + \frac{1}{r}\left(rh^3\frac{\partial}{\partial r}\nabla_r^4 h\right)\\ &+ \frac{32}{\gamma^2}\left(\frac{1}{4} - \frac{r^2}{\gamma^2}\right)\left(1 - \frac{h_0}{\sigma}\right)\end{aligned} \tag{2.16}$$

where the last term is replaced by zero for $r > \gamma/2$. γ and σ are two dimensionless numbers controlling the dynamics of the flow

$$\gamma = \frac{a}{\Lambda} \tag{2.17}$$

$$\sigma = \frac{\Delta P}{\rho_m g H}. \tag{2.18}$$

γ is the dimensionless radius of the conduit, it does not significantly influence the flow and is set to 0.02 in the following (*Michaut and Bercovici*, 2009; *Michaut*, 2011). σ is the normalized pressure head, i.e., the ratio between the initial overpressure driving the flow and the weight of the magma at the center.

2.1.3 Need for regularization

One of the main mathematical difficulty in solving equation (2.16) arises at the contact line between the rigid support and the elastic plate. Indeed, the assumption that the thickness of the fluid tends to zero at the contact line leads to divergent viscous stresses, i.e. $\eta_h \partial u/\partial z \rightarrow \infty$ and hence, the theoretical immobility of the blister (*Flitton and King*, 2004; *Lister et al.*, 2013; *Hewitt et al.*, 2014). This problem, known as the contact-line paradox, is a well know problem for surface-tension driven flow such as the spreading of a water droplet (*Bertozzi*, 1998; *Snoeijer and Andreotti*, 2013).

The formal proof has been given by *Flitton and King* (2004) and can be derived as follow. Suppose that (2.16) has a solution and the solution near the contact line has the form

$$h \sim A(t)(R(t) - r)^{\alpha} \tag{2.19}$$

As $r \rightarrow R(t)$, the bending term dominates the gravitational term and (2.16) reduces to

$$\frac{\partial h}{\partial t} = \frac{1}{r}\frac{\partial}{\partial r}\left(rh^3 \frac{\partial}{\partial r}\nabla_r^4 h\right). \tag{2.20}$$

Injecting (2.19) into (2.20) and keeping only the leading powers of $R - r$ gives

$$\begin{aligned} \frac{\partial R}{\partial t} A\alpha\,(R-r)^{\alpha-1} + \frac{\partial A}{\partial t}\,(R-r)^{\alpha} \quad &= \quad A^4\alpha(\alpha-1)(\alpha-2) \\ &\quad\quad (\alpha-3)(\alpha-4)(\alpha-5)(R-r)^{4\alpha-6}. \end{aligned}$$

The time derivative is locally dominated by its convective part at the tip, the second term on the left is small compared to the first and therefore, by equating the exponent of $R - r$, we obtain $\alpha = 5/3$ and then

$$\frac{\partial R}{\partial r} = -\frac{280}{243}A^3. \tag{2.21}$$

Given that $A > 0$, this shows that (2.16) can only have solutions with retreating contact line ($dR/dt < 0$) but not with advancing contact line ($dR/dt > 0$) (*Lister et al.*, 2013; *Flitton and King*, 2004).

To mitigate this problem, one common approach is to add a thin prewetting film, with thickness h_f such that $h \to h_f$ as $r \to \infty$ (Figure 2.1). While the solution will depend upon the prewetting film thickness h_f and will not show any convergence properties when $h_f \to 0$, we will see that the dependence in h_f is weak and the difference between different values for h_f will be relatively small (*Lister et al.*, 2013; *Hewitt et al.*, 2014). Unless otherwise specified, we often consider $h_f = 5 \cdot 10^{-3}$ in the manuscript which represents the smallest length scale with a physical meaning (Section 2.3.1).

2.2 Results

For a small prewetting film thickness, i.e. $h_f << 1$, the numerical resolution of the equation (2.16) shows two or three asymptotic spreading regimes: a bending regime where gravity is negligible, a viscous gravity current regime where bending is negligible as well as a regime of lateral propagation if the weight of the magma at the center compensates for the initial overpressure (*Michaut*, 2011; *Bunger and Cruden*, 2011; *Lister et al.*, 2013). In the following, we present the shape of the flow as well as scaling laws that predict the evolution of the thickness at the center $h_0(t)$ and the radius $R(t)$ in each regime.

2.2.1 Bending regime

At early times, when $R << \Lambda$, gravity is negligible and the dynamics of the spreading is governed by the bending of the upper layer. In addition, if $h_0 << \sigma$, the overpressure ΔP driving the flow is much larger than the weight of the blister at the center and the injection rate can be considered constant.

In that case, the spreading is very slow and the interior has uniform dimensionless pressure $P = \nabla_r^4 h$. The flow is bell-shaped and its thickness is given by

$$h(r,t) = h_0(t)\left(1 - \frac{r^2}{R^2(t)}\right)^2 \tag{2.22}$$

with $h_0(t)$ the thickness of the intrusion at the center (Figure 2.2, $t < 10$) (*Michaut*, 2011; *Lister et al.*, 2013). In this regime, *Lister et al.* (2013) have shown that the spreading is controlled by the propagation of a peeling by bending wave at the intrusion front with dimensionless velocity c

$$c = \frac{\partial R}{\partial t} = h_f^{1/2}\left(\frac{\kappa}{1.35}\right)^{5/2} \tag{2.23}$$

where $\kappa = \partial^2 h/\partial r^2$ is the dimensionless curvature of the interior solution. Using the propagation law (2.23) and the form of the interior solution (2.22),

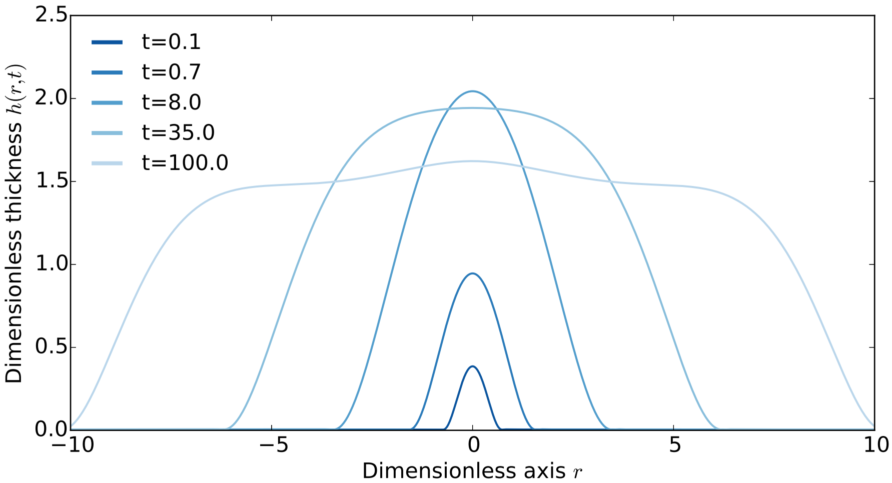

Figure 2.2: Shape of the flow, i.e. thickness $h(r,t)$ as a function of the radial axis r at five different times indicated on the plot. Variables are dimensionless and one needs to multiply by the characteristic scales (thickness, length or time given by (2.14), (2.13) or (2.15)) to obtain dimensional values. For $t < 10$, the intrusion is in the bending regime whereas for $t > 10$ the intrusion is in the gravity current regime.

they find that the radius and the height of the intrusion evolve following

$$R(t) = 2.2 h_f^{1/22} t^{7/22} \tag{2.24}$$

$$h_0(t) = 0.7 h_f^{-1/11} t^{8/22} \tag{2.25}$$

where the numerical pre-factors match our simulations as well as the results of *Lister et al.* (2013) (Figure 2.3) . The bell-shaped morphology of the flow in this regime is very close to the dome-shaped morphology of solidified laccoliths (Figure 1.7 c, d, e) (*Michaut*, 2011).

2.2.2 Gravity current regime

In contrast, when the radius R becomes larger than $\sim 4\Lambda$, the weight of the intrusion becomes dominant over the bending terms. The dimensionless pressure is given by the hydrostatic pressure $P = h$ and the intrusion enters a classical viscous gravity current regime where bending terms only affect the solution near the intrusion edge (Figure 2.2, $t > 10$) (*Huppert*, 1982a; *Michaut*, 2011; *Lister et al.*, 2013). In this second regime, while the thickness tends to be a constant, the radius evolves as $t^{1/2}$ (Figure 2.3). The flow is therefore characterized by a small aspect-ratio h_0/R and a constant thickness

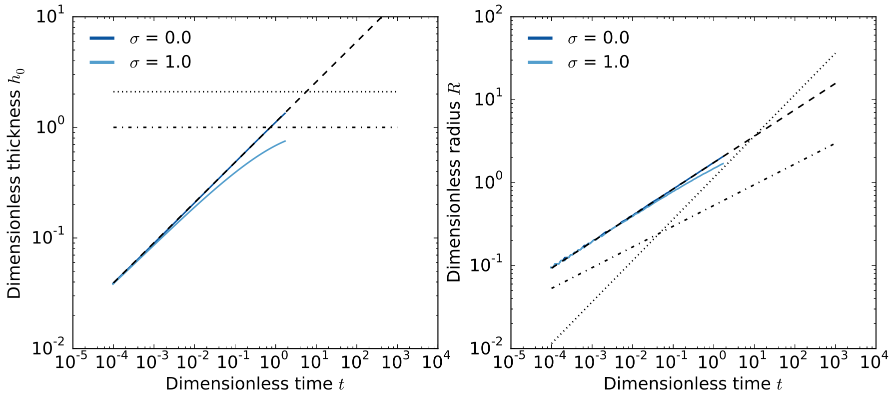

Figure 2.3: Left: Dimensionless thickness at the center h_0 versus dimensionless time t for different dimensionless numbers σ indicated on the plot. The dashed-line represents the scaling law in the bending regime $h_0(t) = 0.7h_f^{-1/11}t^{8/22}$, the dotted line in the gravity regime $h_0(t) = 2.1$ and the dashed-dotted line in the lateral propagation regime $h_0 = \sigma$. Right: Dimensionless radius R versus dimensionless time t for the same dimensionless number σ. The dashed-line represents the scaling law in the bending regime $R(t) = 2.2h_f^{1/22}t^{7/22}$, the dotted line in the gravity regime $R(t) = 1.2t^{1/2}$ and the dashed-dotted line in the lateral propagation regime $R(t) = (\sigma^3 t/(4\pi))^{1/4}$.

disk-like morphology close to the one shown by large mafic sills (Figure 1.7 a).

In between the bending and gravity regime, *Lister et al.* (2013) also describe a short intermediate regime where the peeling by bending continues to control the propagation but where, due to the increasing effect of gravity, the flow shows an interior flat-topped region (Figure 2.2, $t = 38$). This flat-topped morphology is also observed for many laccoliths (*Koch et al.*, 1981; *Bunger and Cruden*, 2011).

2.2.3 Lateral propagation

Once $h_0 \to \sigma$, the flow is thick enough to compensate for the initial overpressure. The thickness at the center remains constant and the flow enters a regime of lateral propagation, where only its radius $R(t)$ increases (*Michaut*, 2011). In this regime, except at the center where it redistributes the pressure over a length scale Λ, the bending term becomes negligible compared to the gravitational term as lateral propagation in enhanced and R reaches $\sim 4\Lambda$ more quickly. In that case, *Michaut* (2011) has shown that the thickness remains constant and the radius evolves as $t^{1/4}$

$$R(t) = \left(\frac{\sigma^3 t}{4\pi}\right)^{1/4} \tag{2.26}$$

$$h_0 = \sigma \tag{2.27}$$

The intrusion shows a disk-like shape, similar to the gravity-current morphology. Therefore, the model is able to reproduce the variety of shapes of intermediate scale magmatic intrusions: from the dome shape and flat topped morphology of laccolith to the disk-like morphology of large mafic sills. In the following, we quantitatively compare the model predictions to some observations on terrestrial planets.

2.3 Application to the spreading of shallow magmatic intrusions

2.3.1 Observations versus predictions on Earth

Observations

Corry (1988) has made an extensive catalog of 900 laccoliths across the world. In particular, *Corry* (1988) provides the thickness and the radius of 168 laccoliths. For 40 of them, he gives an estimate for the intrusion depth. These laccoliths, who are mainly felsic in composition, show thicknesses that range from 100 meters to 1 km with radii in between 1 and 10 km (Figure 2.5 a). While most of the data are located in the United State ($\sim 90\%$), the different laccoliths are widely spread among the territory and variations in the flow parameters between different laccoliths are most likely to be important.

In addition to the data from *Corry* (1988), we also consider in this study the data provided by *Rocchi et al.* (2002) on 9 laccoliths nested in a christmas tree structure at Elba Island, Italy (Figure 2.4). The detailed mapping and reconstruction of tectonic history made by *Rocchi et al.* (2002) provides for the parameters of each intrusive layer in the laccolith complex. In addition, for this dataset, each laccolith is part of a larger intrusive system, and hence variability of the model parameters should be limited, except for the overlying elastic layer thickness, assumed to be the intrusion depth in the model, whose variation between laccoliths is given by *Rocchi et al.* (2002). The dispersion is much smaller for this dataset; the radius ranges from 800 m to 5 km and the thickness from 50 m to 700 m (Figure 2.5 a).

Finally, we also show the morphology of 25 large mafic sills whose thicknesses and radii are given by *Cruden et al.* (2012) (Figure 2.5 a). In order to

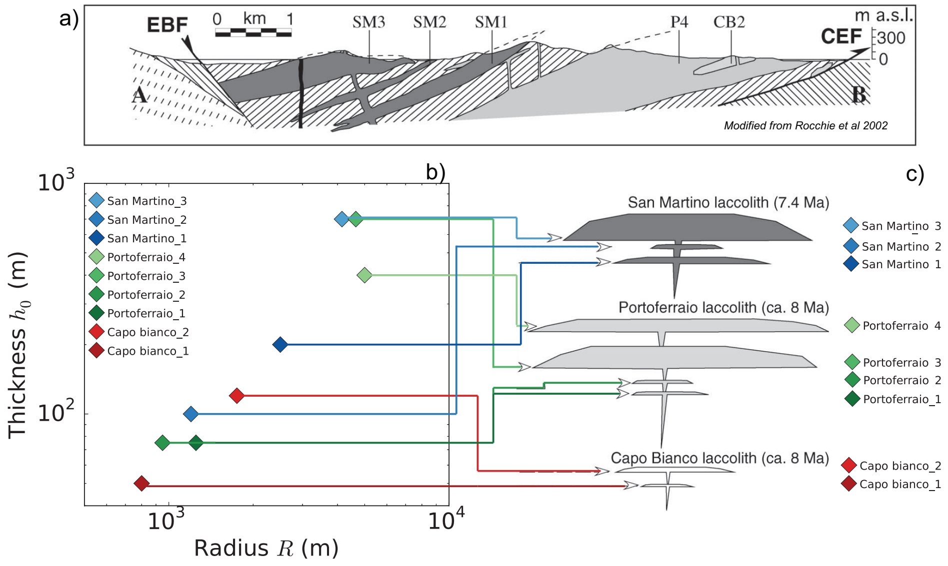

Figure 2.4: a): Cross section of western and central Elba Island where we can see the christmas tree structure of the laccolith complex and the main laccolith units visible at the surface. b) Thickness versus radius of the different laccolith units. c) Sketch of the corresponding location of these laccoliths within the christmas tree structure shortly after their formations. Figure modified from *Rocchi et al.* (2002).

account for the intrinsic scale of different settings for each intrusion and compare them to the model, the data have first to be nondimensionalized using characteristic values for each intrusion parameters and also their depth, when absent from the catalog.

Range of values for the parameters

In terrestrial settings, magma density ρ_m mainly depends on its composition and varies between 2500 kg m^{-3} for felsic magmas to 2900 kg m^{-3} for more mafic magmas. Reported intrusion depths vary from 180 to 2200 m for laccoliths in *Corry* (1988) and from 1.9 to 3.7 km for laccoliths at Elba Island. Hence, for a Young's modulus value of 10 GPa, the characteristic length scale Λ varies between $\sim$ 1 km and $\sim$ 7 km for laccoliths. The density does not affect much the value of Λ and the characteristic length scale for large mafic sills, whose depths are not reported in *Cruden et al.* (2012) and set to 1.5 km, is equal to $\sim$ 3 km.

On Earth, laccoliths are generally formed by relatively evolved lavas that may have differentiated from primitive magma in deep crustal magma cham-

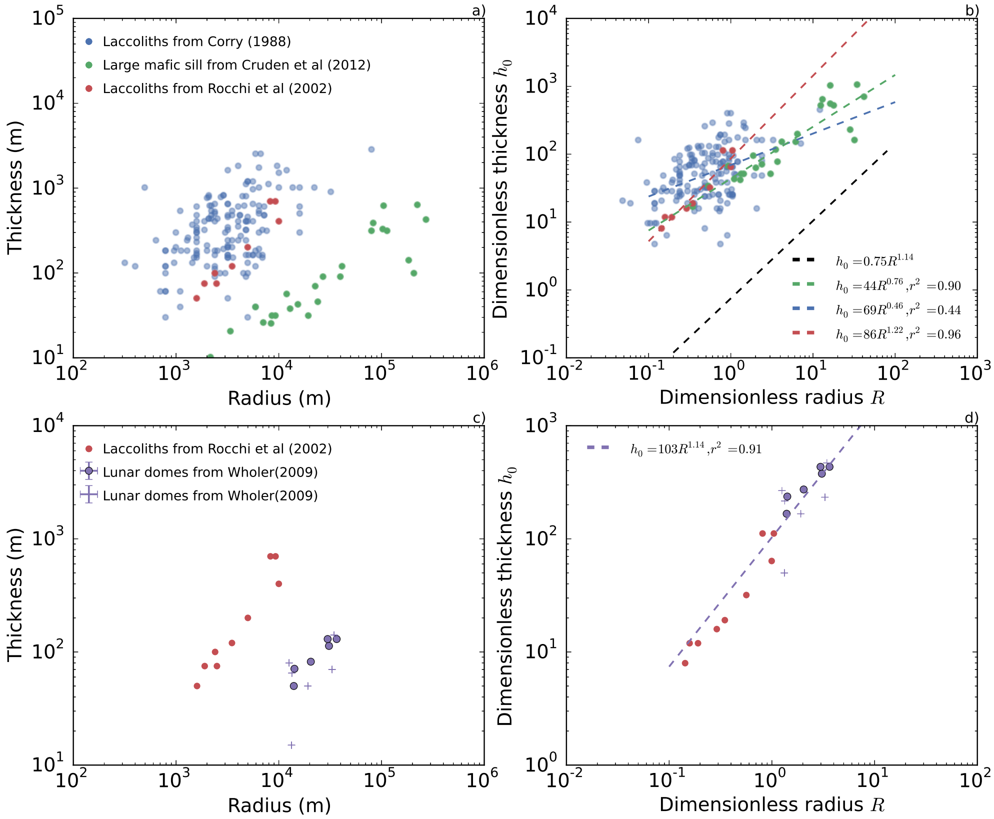

Figure 2.5: a) Thickness at the center h_0 (m) versus radius R (m) for magmatic intrusions from different datasets indicated on the plot. b) Dimensionless thickness as a function of dimensionless radius. Characteristic thickness and length are calculated from (2.14) and (2.13). Dashed lines: predicted scaling law from the simulations (black) and best fit for the power law $h_0 = aR^b$ for each dataset obtained from a linear least-square regression in log-log space. r^2 is the squared of the correlation coefficient, i.e. Pearson product-moment correlation coefficient which gives an indication on the goodness of the fit; 1 is total positive correlation and 0 is no correlation. We use $\rho_m = 2500$ kg m^{-3}, $Q_0 = 10$ m^3 s^{-1} and $\eta_h = 10^6$ Pa s for felsic laccoliths and $\rho_m = 2900$ kg m^{-3}, $Q_0 = 10$ m^3 s^{-1} and $\eta_h = 10^2$ Pa s for large mafic sills. Unless the intrusion depth is given by the dataset, we use $d_c = 1500$ m. $g = 9.81$ m s^{-2}. c) and d), same plots but where we compared the laccoliths from *Rocchi et al.* (2002) to a set of low-slope lunar domes given by *Wöhler et al.* (2009). Lunar domes are nondimensionalized using $g = 1.62$ m s^{-2}, $\rho_m = 2900$ kg m^{-3}, $Q_0 = 10$ m^3 s^{-1}, $\eta_h = 1$ Pa s and d_c, which is not given in the dataset, is set to 1500 m. Purple dots correspond to morphometry reevaluated with the LOLA instrument topography and crosses to the original data. In all cases, the Poisson's ratio is $\nu^* = 0.25$.

bers, located some 5 to 15 km below the surface. The overpressures driving magma ascent are typically 20 to 50 MPa (*Stasiuk et al.*, 1993; *Barmin et al.*, 2002), which gives overpressure gradients of $\sim 10^3$ Pa m^{-1}. Lava viscosity at eruption temperature η_h mainly depends on its composition and water content; close to its liquidus temperature, it can vary from 10^2 Pa s for mafic lavas to 10^6 Pa s for felsic lavas (*Shaw*, 1972; *Giordano et al.*, 2008; *Whittington et al.*, 2009; *Chevrel et al.*, 2013). However, *Wada* (1994) shows that the dyke width tends to increase with viscosity to the power 1/4 (*Kerr and Lister*, 1995) and overall, the injection rate Q_0 should be similar for different magma compositions. Based on common effusion rate for lava flows on Earth, we take $Q_0 \sim 0.1 - 100$ m^3 s^{-1} (*Pieri and Baloga*, 1986; *Harris et al.*, 2000; *Castro et al.*, 2013; *Tuffen et al.*, 2013). The height scale H thus varies between ~ 1 to 10 m for felsic laccoliths and ~ 0.1 and 1 m for large mafic sills.

Table 2.1: Range of values for the model parameters

Parameters	Symbol	Earth	Moon	Unit
Depth of intrusion	d_c	$0.2 - 2.7$	$0.5 - 1.5$	km
Young's Modulus	E	10	10	GPa
Poisson's ratio	ν^*	0.25	0.25	
Gravity	g	9.81	1.62	m s^{-2}
Magma density	ρ_m	$2500 - 2900$	2900	kg m^{-3}
Magma viscosity	η_h	$10^2 - 10^6$	$1 - 10$	Pa s
Feeder dyke width	a	$1 - 100$	10	m
Depth of the melt source	Z_c	$1 - 10$	500	km
Initial overpressure	ΔP	$20 - 50$	50	MPa
Injection rate	Q_0	$0.1 - 100$	$1 - 10^4$	m^3 s^{-1}
Characteristic scales	**Symbol**	**Earth**	**Moon**	**Unit**
Height scale	H	$0.1 - 10$	$0.1 - 1$	m
Length scale	Λ	$1 - 7$	$2.2 - 12$	km
Time scale	τ	$10^{-3} - 100$	$10^{-3} - 10$	years

The model also considers a thin prewetting film of thickness h_f whose meaning in the application to the spreading of laccolith is unclear. In particular, the model shows no convergence when h_f tends to zero (*Lister et al.*, 2013) and therefore, the thickness h_f might be linked to some structural length scale at the front of the laccolith or to the natural imperfection of the flow geometry. For the purpose of the application, we choose a film thickness of 1 mm, i.e. the minimum length scale with physical significance for the spreading of laccoliths which give a dimensionless h_f that varies between 10^{-2} and 10^{-4}. In the following, we set h_f to 10^{-3} unless otherwise specified.

Dimensionless data and comparison with the model

Each magmatic intrusion unit is made dimensionless using its characteristic length scale Λ, which depends upon the intrusion depth, and its characteristic height scale, which is taken as either $H = 6$ m for felsic laccoliths or $H = 0.6$ m for large mafic sills (Figure 2.5). When the intrusion depth is not provided, we use $d_c = 1.5$ km. First, the dimensionless radius of laccoliths at Elba Island and 95% of those from *Corry* (1988) are smaller than 4 consistent with their arrest in the bending regime. The prediction of the model for the evolution of the thickness h_0 of the current as a function of its radius R can be easily derived from the scaling laws (2.25) and (2.24) and should follow

$$h_0 \sim 0.3 h_f^{-1/7} R^{8/7} \tag{2.28}$$

in agreement with the power law relationship $h_0 = bR^a$ initially proposed by *McCaffrey and Petford* (1997) (Section 1.3.2). To characterize the mean trend in each population, we use a linear least-square regression in log-log space to obtain a value for the coefficient a and b that best fit the observations. We found $h_0 = 86R^{1.22}$ for the laccoliths at Elba island which is very close to $R^{1.14}$ predicted by the model (Figure 2.5, $r^2 = 0.96$). Actually, the geometry of these laccoliths is not well known and probably not perfectly axisymmetric. *Hewitt et al.* (2014) found that for a two dimensional flow, $h_0 \propto h_f^{-1/7} L^{10/7}$ where L is the half-length of the flow ($10/7 \sim 1.43$). The best fit value for the coefficient a then nicely inserts between the expected values for the two geometries as noted by *Michaut* (2011). In contrast, the prediction for the coefficient b is much smaller than the value derived from the observations. Even for $h_f = 10^{-2}$, which would be an upper bound for this parameter, the model predict $b = 0.15$, which is three orders of magnitudes smaller than the observations (Figure 2.5). Matching the data to the model will require using a viscosity η_h for the magma abnormally high, i.e. $\eta_h \sim 10^{15}$ Pa s or unreasonable injection rate, i.e. $Q_0 \sim 1$ km^3 s^{-1}.

The best fit power law relationship for the laccoliths from *Corry* (1988) is $h_0 = 85R^{0.62}$ (Figure 2.5, $r^2 = 0.54$). In that case, the exponent a is smaller than one and does not agree with the model. This value for a, slightly smaller than the value calculated directly on the data by *McCaffrey and Petford* (1997), was interpreted as reflecting the two-stage growth process historically invoked for the formation of laccoliths (Section 1.3.2). However, the dispersion in the data is much more important than in the observation from *Rocchi* *et al.* (2010) and is not taken into account in the nondimensionalization which assumes the same parameters for all the different laccoliths. It might explain the discrepancy between the model prediction and the observation in this example.

Half of the large mafic sills show dimensionless radius smaller than $R = 4$, not consistent with their arrest in the gravity current regime (Figure 2.5). It might suggest that these mafic sills have intruded shallower into the crust; for instance, for $d_c = 250$ m, the characteristic length scale for the mafic sill is smaller $\Lambda = 800$ m and 95% of the population show dimensionless radius larger than 4. Nevertheless, their dimensionless thickness, which should tend to a constant of order $O(1)$ according to the model, is much larger than the expected value and increases with the radius R. For a gravity current in a two dimensional geometry, the thickness is indeed expected to increase with the length of the sill, but as $L^{1/4}$ (*Michaut*, 2011), i.e. with an exponent much smaller than the value of 0.76 found for the coefficient a for large mafic sills (Figure 2.5, $r^2 = 0.9$). Therefore, the model predictions hardly reconcile with the observations for large mafic sills.

2.3.2 Low-slope domes on the Moon

Observations

On the Moon, 13 elongated low-slope domes, located around the lunar maria, have been recently identified as potentially intrusive domes (*Wöhler et al.*, 2007, 2009). *Wöhler et al.* (2009) used an image-based 3D reconstruction approach which relies on a combination of photoclinometry and shape from shading techniques to determine the morphometric properties of each of these lunar domes which results in a 10% error estimate on the intrusion thickness. These data have since been updated by Mélanie Thiriet, an under graduate student in our laboratory, who used the high resolution of the topography obtained from the 64 ppd, ~ 450 m/pixel (*Zuber et al.*, 2009), LOLA gridded topography data to reevaluate the thickness and the radius of some of these potentially intrusive lunar domes (Figure 2.5).

Range of values for the parameters

Given the basalt composition of most lunar rocks brought back from the lunar maria by the Apollo missions, the lunar magmas are more likely to be mafic in composition and we use $\rho_m = 2900$ kg m^{-3} for the lava density. Intrusion depths, which are not given by *Wöhler et al.* (2009), should vary between 500 m and 5 km and in the following, we set $d_c = 1.5$ km for all the lunar domes. Therefore, on the Moon, the larger lava density and the smaller gravity leads to length scale 1.5 times larger than terrestrial ones. For instance, using $E = 10$ GPa and $d_c = 1.5$ km, the characteristic length scale for a lunar intrusion is ~ 5 km and 3.3 km for a terrestrial laccolith.

The source of magma in the lunar interior is poorly constrained and more likely to be deeper than on Earth; most of the mare basalt are thought to be a product of melting initiated deep in the lunar mantle, deeper than 400 km (*Shearer*, 2006). Using the same value for the initial driving pressure, $\Delta P = 50$ MPa, unless lunar magmas are likely to be more mafic and contain less volatiles implying smaller driving pressure, and a depth of 500 km for the magma source region, the overpressure gradient is only of 100 Pa m^{-1}. However, reported run out distance for some lava flows in the lunar maria are very large and implies higher effusion rate than on Earth, i.e. $Q_0 = 10^3 - 10^8$ m^3 s^{-1} (*Crisp and Baloga*, 1990; *Zimbelman*, 1998). Mare basalts, which have lower concentration in alkalies than terrestrial basalts, should also have a lower viscosity (*Zimbelman*, 1998). We take $\eta_h = 1$ Pa s and for injection rate between $Q_0 = 1 - 10^4$ m^3 s^{-1}, the typical height scale for lunar domes varies between 0.5 and 1.5 m.

Predictions versus observations

After nondimensionalization, the lunar low-slope domes show dimensionless radius smaller than 4 consistent with their arrest in the bending regime (Figure 2.5). In addition, if we use $Q_0 = 10$ m^3 s^{-1} and the values of the parameters listed above to calculate the height scale H, they are almost perfectly aligned with the terrestrial laccolith from Elba Island (Figure 2.5) (*Michaut*, 2011). Indeed, the best fit for the power law $h_0 = bR^{8/7}$ for all the observations, lunar domes + Elba Island laccoliths, is $h_0 = 103R^{1.14}$ with a high correlation coefficient $r^2 = 0.9$. Given that the same intrusion depth has been arbitrarily chosen for all intrusions, the fit is surprisingly accurate. Therefore, the isoviscous elastic-plated gravity current model supports the intrusive origin of the lunar domes described by *Wöhler et al.* (2009) and their arrest in the bending regime. In addition, it is able to explain the difference between Earth laccolith and lunar intrusive domes (*Michaut*, 2011).

2.3.3 What causes the arrest of a shallow magmatic intrusion?

The model shows promising results in reproducing the overall morphology of terrestrial laccoliths but lacks of a predictive criteria for their arrest. Fracturation is generally considered as the limiting mechanism for the spreading of magmatic intrusions and in the following, we consider fracturation as a possible mechanism for the arrest of magmatic intrusions into the bending regime.

As the flow length increases, the pressure in the intrusion eventually decreases to the critical value equal to the pressure necessary for fracturing the tip. In that case, fracturing at the tip might limit spreading and trigger the arrest of a laccolith in the bending regime. The stress intensity factor K_I for a mode I fracture and a uniformly loaded crack situated close to a boundary (i.e., $d << R$) can be approximated by (*Dyskin et al.*, 2000; *Bunger and Emmanuel*, 2005)

$$K_I = K_M M_0 d_c^{-3/2} \tag{2.29}$$

where $K_M = 1.932$ is a constant and M_0 is the bending moment at the crack tip given by

$$M_0 = -D\left(\frac{\partial^2 h}{\partial r^2} + \frac{1}{r}\frac{\partial h}{\partial r}\right)\bigg|_{r=R(t)}. \tag{2.30}$$

Once K_I reaches the fracture toughness limit K_c, which is in the range $\sim 1-10$ MPa m$^{1/2}$ for crustal rocks and a mode I fracture (*Lister and Kerr*, 1991), fracturing at the tip will limit the lateral extent of the intrusion.

Injecting the dimensional scaling law for the thickness h_0 as a function of the radius R (2.28) into the predicted flow shape in the bending regime (2.22) gives the flow shape as a function of the radius $R(t)$ for a fractured-limited flow in the bending regime is

$$h(r,t) = 0.6H^{8/7}\Lambda^{-8/7}R(t)^{8/7}\left(1 - \frac{r^2}{R^2(t)}\right)^2. \tag{2.31}$$

Injecting this expression into (2.30) and (2.29) and inverting for the radius, one can then found that the critical dimensionless radius R_{cr} for the laccolith is

$$R_{cr} \sim \frac{0.5E^{7/6}H^{4/3}K_m^{7/6}}{K_c^{7/6}\Lambda^{4/3}}d^{7/4} \tag{2.32}$$

which, in terms of the parameters, reads

$$R_{cr} \sim 3E^{7/12}K_m^{7/6}Q_0^{1/3}\eta_h^{1/3}g^{1/4}\rho_m^{1/4}K_c^{-7/6} \tag{2.33}$$

and therefore mainly depends in the fracture toughness of the encasing rocks. On can calculate that for typical crustal and magma parameters for terrestrial laccoliths (Section 2.3) and the largest reported value for the parameter $K_c =$ 10 MPa m$^{1/2}$, the critical radius is equal to $\sim 80\Lambda$ and therefore, still much larger than the transition radius between the bending and gravity regime $R = 4\Lambda$. Therefore, while fracturation might explain the arrest for large mafic sills, it does not provide a sufficient mechanism for the arrest of laccoliths.

2.3.4 Discussion

Historical models for intermediate scale magmatic intrusions consider that the main phase of laccolith growth and spreading require a two-stage process: horizontal spreading of a sill followed by vertical inflation when the sill has grown horizontally enough so that the magma has enough leverage on the overlying layer to begin to bend them upward (*Johnson and Pollard*, 1973; *Koch et al.*, 1981). More recent models instead proposed that these intrusions form as a series of sub-horizontally staked magma sheets (*Morgan et al.*, 2008; *Menand*, 2011). While both models are able to account for several geological observations, they both lack a physical description of the intrusion process and are then not able to explain the solidified morphology of these magmatic intrusions in terms of flow parameters (injection rate, volume) at the time of emplacement.

Michaut (2011) has developed a new approach to model intermediate-scale intrusions such as sills, laccoliths or bysmaliths through a dynamic elastic-plated gravity current model that considers both the bending and the own weight of the magma as driving the flow. This model shows promising results in predicting the variety of shapes of intermediate scale magmatic intrusions; from the dome shape of laccolith to the disk-like morphology of large mafic sill. It allows to relate the laccolith morphology to the crustal and magma physical properties, and more importantly, to the injection rate. The prediction of the model, especially the exponent of the thickness to radius power law relationship, also fits the variability in the laccolith units at Elba Island, hence providing for a physical explanation for the observed laccolith morphology. In addition, the model is also consistent with a two-stage growth process; first, the lateral growth of a sill and then, when the conditions of applicability for the model are met, i.e. $R > h_0$ and $R \gtrsim d_c$, spreading and thickening occur simultaneously (*Michaut*, 2011). Finally, the model shows promising results in explaining the discrepancy between terrestrial laccolith and low-slope lunar domes on the Moon. Therefore, it can be used to assess the intrusive origin of intrusive candidates on other terrestrial planets.

However, other questions remain open. First, we have shown that the model hardly accounts for the absolute final value for both the thickness and the radius of these laccoliths and that reconciliating predictions and observations requires abnormally high magma viscosity. In addition, we show that the model does not offer a satisfactory explanation for the increase in large mafic sill thickness with their diameter. Finally, we also show that fracturation is not likely to stop a magmatic intrusion in the bending regime. Therefore, other mechanisms not taken into account in the model of *Michaut* (2011), are required to understand the final morphology of these magmatic intrusions.

2.4 Toward a more realistic model for shallow magmatic intrusions

In this manuscript, we propose to explore two important mechanisms that have been neglected until now and will certainly influence the emplacement of shallow magmatic intrusions in the crust of terrestrial planets: the effect a temperature-dependent rheology for the magma and the effect of an overburden characterized by a non-constant thickness.

The former has already shown important implications for the cooling of lava domes (*Bercovici*, 1994; *Bercovici and Lin*, 1996; *Balmforth and Craster*, 2004; *Garel et al.*, 2014). Indeed, the viscosity of magma can vary by several orders of magnitudes during cooling (*Shaw*, 1972; *Lejeune and Richet*, 1995). As the fluid cools, its composition and crystal content change which, in turn, modifies the viscosity and the dynamics of the flow itself. The first part of the manuscript deals with this matter and try to better understand the dynamics of a cooling elastic-plated gravity current. In particular, in chapter 3, we propose a model for the cooling of an elastic-plated gravity current with a temperature-dependent viscosity and isothermal boundary conditions. This model is next further refined to account for the heating of the wall rocks and compared to the observation in chapter 4.

The second part of the manuscript addresses the second point and in particular, the problem of crater-centered intrusions with application to the endogenous deformations observed at lunar floor-fractured craters. Indeed, these impact craters on the Moon show important deformations that might be related to the emplacement of a shallow magmatic intrusion below their floor (*Schultz*, 1976). Chapter 5 presents the theoretical model and its application to the deformations observed at floor-fractured craters. Then, chapter 6 takes the study of floor-fractured craters one step further by looking at the gravitational signature of lunar floor-fractured craters in the light of the model predictions.

This thesis, closely combining theoretical models and observations, expands and generalizes the model of *Michaut* (2011) exposed in this chapter, and sheds light on the final morphology of shallow magmatic intrusions on one side and on the origin of lunar floor-fractured craters on the other side.

Part II

Evolution thermique des intrusions magmatiques à faible profondeur

Chapter 3

Elastic-plated gravity current with temperature-dependent viscosity

Contents

Temperature-dependent elastic-plated gravity currents have numerous applications in nature, from shallow magmatic intrusions to the flow of melt-water below an ice sheet. We develop the general equations for an elastic-plated gravity current with a temperature-dependent viscosity for constant influx conditions. We show that the coupling between the thermal structure and the flow itself results in important deviations from the isoviscous case. In particular, the bending and gravity asymptotic regimes, characteristic of the isoviscous case, both split into three phases: a first 'hot' isoviscous phase, a second phase where the flow effective viscosity and thickness drastically increase and a third 'cold' isoviscous phase. These three phases are controlled by the extent of the thermal anomaly, for which we develop analytical scaling laws. The effective flow viscosity is governed by the local thermal state at the current tip in the bending regime while it is the average flow viscosity in the gravity regime. In the end, the complete evolution of such an elastic-plated gravity current depends on its thermal state at the transition between the bending and gravity regimes. We provide a phase diagram which predicts the different evolution scenarios as a function of the flow Peclet number and viscosity contrast.

3.1 Introduction

Elastic-plated gravity currents involve the spreading of viscous material beneath an elastic sheet. The applications range from the emplacement of lava in the shallow crust (*Michaut*, 2011; *Bunger and Cruden*, 2011) and melt-water drainage below ice sheet (*Das et al.*, 2008; *Tsai and Rice*, 2010) in geological setting to the manufacture of flexible electronics and microelectromechanical systems (MEMS) in engineering (*Hosoi and Mahadevan*, 2004).

When the thickness of the flow is small compared to its extent, lubrication approximation applies and the study of elastic-plated gravity currents resumes to the study of a sixth order, non-linear partial differential equation (*Michaut*, 2011; *Lister et al.*, 2013; *Hewitt et al.*, 2014) . However, the assumption that the thickness of the fluid tends to zero at the contact line leads to divergent viscous stresses, and hence, a regularization condition is needed at the front (*Flitton and King*, 2004; *Lister et al.*, 2013; *Hewitt et al.*, 2014). One common approach is to add a thin prewetting film of fluid, thus avoiding the requirement for any boundary conditions at the contact line (*Lister et al.*, 2013; *Hewitt et al.*, 2014).

The dynamics of the spreading has been described in an axisymmetric geometry for a Newtonian fluid with constant viscosity (*Michaut*, 2011; *Lister et al.*, 2013; *Thorey and Michaut*, 2014) and show two distinct regimes of evolution. First, gravity is negligible and the peeling of the front is driven by bending of the overlying layer; the interior is bell-shaped, the radius evolves as $t^{8/22}$ and the thickness as $t^{7/22}$. When the radius becomes larger than 4Λ, where Λ is the flexural wavelength of the upper layer, the weight of the current becomes dominant over the bending terms and the flow enters a gravity current regime (*Huppert*, 1982a). In this regime, the thickness profile develops a flat top with bent edges, the radius evolves as $t^{1/2}$ while the thickness tends to a constant. Different analogue experiments of isoviscous flows confirm these theoretical results (*Dixon and Simpson*, 1987; *Lister et al.*, 2013).

However, in many real geological settings, the isothermal/isoviscous assumption are not valid. For instance, the viscosity of magmas, produced by partial melting of the upper mantle, can vary by several orders of magnitude (*Shaw*, 1972; *Lejeune and Richet*, 1995). Therefore, as the fluid flows, it cools down, its composition and crystal content change which, in turn, modifies the viscosity and the dynamics of the flow. Several studies have shown that, in a gravity current, this coupling between the cooling and the flow itself results in important deviations from the isoviscous case (*Bercovici*, 1994; *Bercovici and Lin*, 1996; *Balmforth and Craster*, 2004; *Garel et al.*, 2014).

In this paper, we examine how the spreading of an elastic-plated gravity current is affected by the cooling itself. In particular, we consider the problem of an elastic-plated gravity current whose viscosity depends on temperature according to a prescribed rheology $\eta(T)$. This gives rise to a set of two coupled non-linear equations that we solve numerically. We study the flow thermal structure and its effect on the dynamics through the rheology in each regime separately. In both regimes, we identify different "thermal" phases of propagation that we characterize by different scaling laws.x

3.2 Theory

3.2.1 Formulation

We model the axisymmetric flow of fluid below an elastic layer of constant thickness d_c and above a semi infinite rigid layer (Figure 3.1). The assumption that the thickness of the fluid $h(r,t)$ tends to zero at the contact line leads to divergent viscous stresses and to the theoretical immobility of the current (*Flitton and King*, 2004). To avoid problem at the contact line, we consider

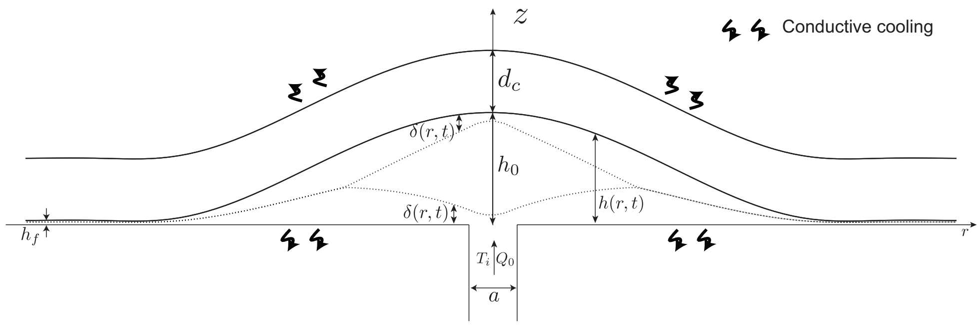

Figure 3.1: Model geometry and parameters. The vertical scale is exaggerated.

a thin pre-wetting film of thickness h_f (*Lister et al.*, 2013) (Figure 3.1).

The fluid is injected continuously at the base and center of the current at a constant rate Q_0 through a conduit of diameter a. The hot fluid is intruded at temperature T_i and cools through the top and bottom by conduction in the surrounding medium, whose temperature is considered constant and equal to T_0. In using a fixed temperature at the flow boundary, we essentially assume that the fluid is bounded by a medium with infinite thermal conductivity.

As it cools, the viscosity of the fluid increases following a prescribed temperature-dependent rheology $\eta(T)$ given by

$$\eta(T) = \frac{\eta_h \eta_c (T_i - T_0)}{\eta_h (T_i - T_0) + (\eta_c - \eta_h)(T - T_0)} \tag{3.1}$$

where η_h and η_c are the viscosities of the hottest and coldest fluid at the temperature T_i and T_0 respectively (*Bercovici*, 1994). Although this rheology is largely simplified, the inverse dependence of viscosity on temperature captures the essential behavior of a viscous fluid, i.e. the viscosity variations are the largest where the temperature is the coldest (*Shaw*, 1972; *Marsh*, 1981; *Lejeune and Richet*, 1995; *Giordano et al.*, 2008).

3.2.2 Pressure

The intrusion develops over a length scale Λ that is much larger than its thickness H ($\Lambda >> H$). In the laminar regime and in axisymmetrical coordinates

(r,z), the Navier-Stokes equations within the lubrication approximaton are

$$-\frac{\partial P}{\partial r}+\frac{\partial}{\partial z}\left(\eta(T)\frac{\partial u}{\partial z}\right) = 0 \tag{3.2}$$

$$-\frac{\partial P}{\partial z}-\rho_m g = 0 \tag{3.3}$$

where $u(r,z,t)$ is the radial velocity, ρ_m the fluid density, g the standard acceleration due to gravity and $P(r,z,t)$ the pressure within the fluid. Integration of (3.3) gives the total pressure $P(r,z,t)$ within the flow. When the vertical deflection $h(r,t)$ of the upper elastic layer is small compared to its thickness d_c, i.e $h << d_c$, we can neglect stretching of the upper layer and only consider bending stresses. Therefore, the total pressure $P(r,z,t)$ at a level z in the current is the sum of three contributions: the weight of the magma and of the upper layer and the bending pressure

$$P=\rho_m g(h-z)+\rho_r g d_c + D\nabla_r^4 h \tag{3.4}$$

where $h(r,t)$ is the flow thickness, ρ_r the density of the surrounding rocks and D is the flexural rigidity of the thin elastic layer, that depends on Young's modulus E, Poisson's ratio ν^* and on the elastic layer thickness d_c as $D = Ed_c^3/\left(12(1-\nu^*)\right)$.

3.2.3 Injection rate

Assuming a Poiseuille flow within the cylindrical feeding conduit, the vertical injection velocity $w_i(r,t)$ and injection rate Q_0 are given by

$$w_i(r,t)=\begin{cases}\frac{\Delta P}{4\eta_h Z_c}(\frac{a^2}{4}-r^2) & r\le \frac{a}{2}\\ 0 & r>\frac{a}{2}\end{cases} \tag{3.5}$$

$$Q_0=\frac{\pi\Delta P a^4}{128\eta_h Z_c} \tag{3.6}$$

where ΔP is the initial overpressure within the melt at $z = Z_c$.

3.2.4 Heat transport equation

3.2.4.1 Local energy conservation

In the laminar regime and in axisymmetrical coordinates (r,z), the local energy conservation equation within the lubrication assumption is

$$\frac{D}{Dt}\left(\rho_m C_{p,m}T+\rho_m L(1-\phi)\right) = k_m\frac{\partial^2 T}{\partial z^2} \tag{3.7}$$

where $T(r, z, t)$ is the fluid temperature and ρ_m, k_m and $C_{p,m}$ are the density, thermal conductivity and specific heat of the fluid. Here, we also account for energy release by crystallization of the fluid, which is a non negligible source of heat for magmas; $\phi(r, z, t)$ is the crystal fraction in the melt and L the latent heat of crystallization. In this model, the crystals are considered only as a source/sink of energy as they melt/form during flow emplacement. In particular, the physical properties of the fluid are not modified by the presence of crystals.

Following a common approximation, we assume that the crystal fraction is a linear function of temperature over the melting interval

$$\phi = \frac{T_L - T}{T_L - T_s} \tag{3.8}$$

where T_S and T_L are the solidus and liquidus temperatures of the magma (*Hort*, 1997; *Michaut and Jaupart*, 2006). In addition, we assume that the fluid is injected at its liquidus temperature , i.e. $T_L = T_i$ and, for simplicity, that the solidus temperature is equal to the surrounding rock temperature $T_S = T_0$. With these approximations, the local energy equation (3.7) resumes to

$$\frac{\partial T}{\partial t} + u\frac{\partial T}{\partial r} + w\frac{\partial T}{\partial z} \quad = \quad \frac{St}{St+1}\kappa_m\frac{\partial^2 T}{\partial z^2} \tag{3.9}$$

where $u(r, z, t)$ and $w(r, z, t)$ are the radial and vertical fluid velocities, $St = \left(C_{p,m}(T_i - T_0)\right)/L$ is the Stefan number and κ_m is the fluid thermal diffusivity $\kappa_m = k_m/(\rho_m C_{p,m})$. We use an integral balance method to solve the heat transport equation (3.9). This theory is based on the integral-balance method of heat-transfer theory of *Goodman* (1958), in which the vertical structure of the temperature field is represented by a known function of depth that approximates the expected solution.

3.2.4.2 Integral balance solution for the temperature $T(r, z, t)$

Following *Balmforth and Craster* (2004), we model the cooling of the flow through the growth of two thermal boundary layers: one growing downward from the top and a second growing upward from the base. As we consider homogeneous thermal properties for the surrounding rocks, we assume that the two thermal boundary layers grow symmetrically and have the same thickness $\delta(r, t)$ (Figure 3.1). We use the following approximation for the vertical temperature profile $T(r, z, t)$

$$T = \begin{cases} T_b - (T_b - T_0)(1 - \frac{z}{\delta})^2 & 0 \le z \le \delta \\ T_b & \delta \le z \le h - \delta \\ T_b - (T_b - T_0)(1 - \frac{h-z}{\delta})^2 & h - \delta \le z \le h \end{cases} \tag{3.10}$$

where $T_b(r,t)$ is the temperature at the center of the flow. The integral balance solution in (3.10) assumes a symmetry around $z = h/2$ and a decrease of the temperature in the two thermal boundary layers down to the surrounding rock temperature T_0 (*Balmforth and Craster*, 2004). In addition, it assumes a uniform temperature T_b in between the thermal boundary layers. As the fluid is injected at temperature T_i, we have $T_b(r,t) = T_i$ as long as $\delta < h/2$ (Figure 3.1). However, if the two thermal boundary layers connect, then $\delta = h/2$ and $T_b \leq T_i$. This profile assures the continuity of the temperature and heat flux within the flow.

3.2.4.3 Integral balance equation

We begin by integrating the local energy conservation equation (3.9) separately over the two thermal boundary layers. The integration over the bottom thermal layer, i.e. from the base, $z = 0$ to a level $z = \delta$ gives

$$\begin{aligned} &\frac{\partial}{\partial t}\left(\delta(\bar{T} - T_b)\right) + \frac{1}{r}\frac{\partial}{\partial r}\left(r\delta(\overline{uT} - \bar{u}T_b)\right) + \delta\left(\frac{\partial T_b}{\partial t} + \bar{u}\frac{\partial T_b}{\partial r}\right) \\ = \;& -\frac{\kappa_m}{1+St}\left.\frac{\partial T}{\partial z}\right|_{z=0} + w_i(T_i - T_b) \end{aligned} \tag{3.11}$$

where the bars indicate the vertical average over the bottom thermal boundary layer

$$\bar{f} = \frac{1}{\delta}\int_0^\delta f dz,$$

which will be determined once the horizontal flow velocity is derived, $T_b(r,t)$ is the temperature at $z = \delta$, $w_i(r)$ is the vertical injection velocity and we have used the nullity of the thermal gradient at $z = \delta$ and the local mass conservation

$$\frac{1}{r}\frac{\partial ru}{\partial r} + \frac{\partial w}{\partial z} = 0. \tag{3.12}$$

The integration over the top thermal layer, i.e., from the level, $z = h - \delta$ to the top $z = h$ gives

$$\begin{aligned} &\frac{\partial}{\partial t}\left(\delta(\bar{T} - T_b)\right) + \frac{1}{r}\frac{\partial}{\partial r}\left(r\delta(\overline{uT} - \bar{u}T_b)\right) + \delta\left(\frac{\partial T_b}{\partial t} + \bar{u}\frac{\partial T_b}{\partial r}\right) \\ = \;& \frac{\kappa_m}{1+St^{-1}}\left.\frac{\partial T}{\partial z}\right|_{z=h} \end{aligned} \tag{3.13}$$

where, in addition to the local mass conservation (3.12) and the fact that the thermal gradient at $z = h - \delta$ is equal to zero, we have used the kinematic boundary condition in $z = h(r,t)$

$$\frac{\partial h}{\partial t} + u\frac{\partial h}{\partial r} = w. \tag{3.14}$$

Therefore, the heat balance equation, i.e. the heat equation (3.9) integrated over the flow thickness, is obtained by adding (3.11) and (3.13). Using (3.10) to derive the conductive fluxes, we finally obtain

$$\frac{\partial}{\partial t}\left(\delta(\bar{T}-T_b)\right)+\frac{1}{r}\frac{\partial}{\partial r}\left(r\delta(\overline{uT}-\bar{u}T_b)\right)+\delta\left(\frac{\partial T_b}{\partial t}+\overline{u}\frac{\partial T_b}{\partial r}\right)$$
$$= -\frac{2\kappa_m}{(1+St^{-1})}\frac{(T_b-T_0)}{\delta}+\frac{w_i}{2}(T_i-T_b). \tag{3.15}$$

3.2.5 Equation of motion

A global statement of mass conservation gives

$$\frac{\partial h}{\partial t}+\frac{1}{r}\frac{\partial}{\partial r}\left(r\int_0^h udz\right)=w_i. \tag{3.16}$$

To obtain an equation for the flow thickness, we first note that the chosen vertical structure of the temperature field (3.10) is symmetric around $h/2$, and thus, because the boundary condition are the same at $z=0$ and $z=h$, the viscosity and velocity u possess the same symmetry. Taking advantage of this symmetry, we integrate once (3.2) using $\frac{\partial u}{\partial z}\big|_{z=h/2}=0$ to get

$$\frac{\partial u}{\partial z}=\frac{1}{\eta(z)}\frac{\partial P}{\partial r}\left(z-\frac{h}{2}\right). \tag{3.17}$$

Using no-slip boundary conditions at the top and the bottom of the flow, i.e. $u(r,z=0,t)=u(r,z=h,t)=0$, (3.16) can be rewritten as

$$\frac{\partial h}{\partial t}=\frac{1}{r}\frac{\partial}{\partial r}\left(r\int_0^h\frac{\partial u}{\partial z}zdz\right)+w_i. \tag{3.18}$$

Finally, injecting (3.17) into (3.18) gives the equation for the flow thickness evolution in axisymmetric coordinates

$$\frac{\partial h}{\partial t}=\frac{1}{r}\frac{\partial}{\partial r}\left(r\left(\rho_m g\frac{\partial h}{\partial r}+D\frac{\partial}{\partial r}\left(\nabla_r^4 h\right)\right)\left(\int_0^h\frac{1}{\eta(y)}\left(y-\frac{h}{2}\right)ydy\right)\right)+w_i \tag{3.19}$$

In addition, integration of (3.17) using the no-slip boundary condition at the base of the flow gives

$$u(r,z,t)=\frac{\partial P}{\partial r}\int_0^z\frac{1}{\eta(y)}\left(y-\frac{h}{2}\right)dy. \tag{3.20}$$

where

$$\frac{1}{\eta(y)}=\frac{1}{\eta_c}+\frac{\eta_c-\eta_h}{\eta_h\eta_c}\frac{T(y)-T_0}{T_i-T_0}. \tag{3.21}$$

$T(y)$ being a polynom, integrals in (3.19), (3.20) as well as the averaged quantities $\overline{u}$ and $\overline{uT}$ over the thermal boundary layer in (3.15) can easily be calculated.

3.2.6 Dimensionless equations

We use the characteristic temperature interval $\Delta T = T_i - T_0$ to nondimensionalize temperatures. The dimensionless integral balance approximation (3.10) becomes

$$\theta(z) = \begin{cases} \Theta_b\left(1-(1-\frac{z}{\delta})^2\right) & 0 \le z \le \delta \\ \Theta_b & \delta \le z \le h-\delta \\ \Theta_b\left(1-(1-\frac{h-z}{\delta})^2\right) & h-\delta \le z \le h \end{cases} \quad (3.22)$$

where $\theta(r,z,t)$ is the dimensionless temperature and $\Theta_b = \frac{T_b - T_0}{T_i - T_0}$. Finally, equations (3.15) and (3.19) are nondimensionalized using a horizontal scale Λ, a vertical scale H and a time scale τ given by

$$\Lambda = \left(\frac{D}{\rho_m g}\right)^{1/4} \quad (3.23)$$

$$H = \left(\frac{12\eta_h Q_0}{\rho_m g \pi}\right)^{1/4} \quad (3.24)$$

$$\tau = \frac{\pi \Lambda^2 H}{Q_0} \quad (3.25)$$

where Λ represents the flexural wavelength of the upper elastic layer (*Michaut*, 2011), H the characteristic thickness of an isoviscous constant flux gravity current with viscosity η_h (*Huppert*, 1982b) and τ the characteristic time to fill up a cylindrical flow of radius Λ and thickness H at a constant rate Q_0. In addition, we can define a horizontal velocity scale $U = \Lambda/\tau = (\rho_m g H^3)/(12\eta_h \Lambda)$ and a pressure scale $\rho_m g H$.

The dimensionless equations are

$$\frac{\partial h}{\partial t} = \frac{12}{r}\frac{\partial}{\partial r}\left(r\left(\frac{\partial h}{\partial r} + \frac{\partial}{\partial r}\left(\nabla_r^4 h\right)\right) I_1(h)\right) + w_i \quad (3.26)$$

$$\frac{\partial}{\partial t}\left(\delta(\bar{\theta} - \Theta_b)\right) = -\frac{1}{r}\frac{\partial}{\partial r}\left(r\delta(\overline{u\theta} - \bar{u}\Theta_b)\right) - \delta\left(\frac{\partial \Theta_b}{\partial t} + \bar{u}\frac{\partial \Theta_b}{\partial r}\right)$$
$$- 2Pe^{-1}St_m\frac{\Theta_b}{\delta} + \frac{w_i}{2}(1-\Theta_b) \quad (3.27)$$

$$w_i = \frac{32}{\gamma^2}\left(\frac{1}{4} - \frac{r^2}{\gamma^2}\right) \text{ if } r < \gamma/2, \; w_i = 0 \text{ if } r \ge \gamma/2 \quad (3.28)$$

$$u(r,z,t) = 12\left(\frac{\partial h}{\partial r} + \frac{\partial}{\partial r}\left(\nabla_r^4 h\right)\right) I_0(z) \quad (3.29)$$

with

$$I_0(z) = \int_0^z (\nu + (1-\nu)\theta(y))\left(y - \frac{h}{2}\right) dy \quad (3.30)$$

$$I_1(z) = \int_0^z (\nu + (1-\nu)\theta(y))\left(y - \frac{h}{2}\right) y dy \quad (3.31)$$

and where γ, Pe, St_m and ν are the four dimensionless numbers that control the dynamics of the flow

$$\gamma = \frac{a}{\Lambda} \tag{3.32}$$

$$Pe = \frac{H^2}{\kappa_m \tau} \tag{3.33}$$

$$St_m = \frac{C_{p,m}\,(T_i - T_0)}{C_{p,m}\,(T_i - T_0) + L} \tag{3.34}$$

$$\nu = \frac{\eta_h}{\eta_c} \tag{3.35}$$

γ is the dimensionless radius of the conduit, it does not significantly influence the flow and is set to 0.02 in this study (*Michaut and Bercovici*, 2009; *Michaut*, 2011); Pe is the Peclet number which compares the vertical diffusion of heat to the horizontal advection in the interior; St_m is a modified Stefan number which represents the ratio of sensible heat between solidus and liquidus to the total energy of the fluid at the liquidus temperature and ν is the maximum viscosity contrast, i.e. the ratio between the hottest and coldest viscosity.

3.2.7 Further simplifications

3.2.7.1 Heat equation

In the end, the heat balance equation (3.27) can reduce to

$$\frac{\partial}{\partial t}\left(\delta(\bar{\theta}-1)\right) + \frac{1}{r}\frac{\partial}{\partial r}\left(r\delta(\overline{u\theta}-\bar{u})\right) = -2Pe^{-1}St_m\frac{\Theta_b}{\delta} \tag{3.36}$$

Indeed, if the thermal boundary layers exist, $\Theta_b = 1$, δ is the variable quantity and (3.27) directly reduces to (3.36). In contrast, if the thermal boundary layers merge, $\delta = h/2$ and the variable quantity is Θ_b. In this case, the heat balance equation (3.27) reduces to

$$\frac{\partial h\bar{\theta}}{\partial t} + \frac{1}{r}\frac{\partial}{\partial r}\left(rh\overline{u\theta}\right) - \Theta_b\left(\frac{\partial h}{\partial t} + \frac{1}{r}\frac{\partial}{\partial r}\left(rh\bar{u}\right)\right) = -8St_mPe^{-1}\frac{\Theta_b}{h} + w_i(1-\Theta_b) \tag{3.37}$$

which, by using (3.16), rewrites

$$\frac{\partial h\bar{\theta}}{\partial t} + \frac{1}{r}\frac{\partial}{\partial r}\left(rh\overline{u\theta}\right) = w_i - 8St_mPe^{-1}\frac{\Theta_b}{h}. \tag{3.38}$$

Equation (3.38) also corresponds to (3.36) when $\delta = h/2$.

Following *Balmforth and Craster* (2004), we rewrite (3.36) using a new variable $\xi = \delta(1-\bar{\theta})$

$$\frac{\partial \xi}{\partial t} + \frac{1}{r}\frac{\partial}{\partial r}\left(r\bar{u}\xi\right) - \frac{1}{r}\frac{\partial}{\partial r}\left(r\delta(\overline{u\theta}-\bar{u}\bar{\theta})\right) = 2Pe^{-1}St_m\frac{\Theta_b}{\delta}. \tag{3.39}$$

where our unknown Θ_b or δ can be calculated directly from the expression of ξ using $\delta = h/2$ or $\Theta_b = 1$ respectively

$$\Theta_b(r) = \begin{cases} 1 & \text{if} \quad \xi \leq \xi_t \\ \frac{3}{2} - \frac{3\xi}{h} & \text{if} \quad \xi > \xi_t \end{cases} \qquad \delta(r) = \begin{cases} 3\xi & \text{if} \quad \xi \leq \xi_t \\ h(r,t)/2 & \text{if} \quad \xi > \xi_t \end{cases}$$

with $\xi_t = h/6$.

The second term on the left hand side of (3.39) contains advection by the vertically integrated radial velocity while the third term contains a correction accounting for the vertical structure of the temperature field. The term on the right is the loss of heat by conduction in the surrounding medium.

3.2.7.2 Average quantities

The average velocity over a thermal boundary layer $\overline{u}$ reads

$$\overline{u} = \frac{1}{\delta}\int_0^\delta u dz = u(r,\delta,t) - \frac{1}{\delta}\int_0^\delta \frac{\partial u}{\partial z} z dz \tag{3.40}$$

$$= \frac{12}{\delta}\frac{\partial P}{\partial r}\left(\delta I_0(\delta) - I_1(\delta)\right) \tag{3.41}$$

where $P(r,z,t) = h + \nabla_r^4 h$ is the dimensionless dynamic pressure and we have used (3.17) in (3.40). The average rate of heat advected $\overline{u\theta}$ over a thermal boundary layer reads

$$\overline{u\theta} = \frac{1}{\delta}\int_0^\delta u\theta dz = \frac{1}{\delta}\left([uG(z)]_0^\delta - \int_0^\delta G(z)\frac{\partial u}{\partial z} dz \right)$$

$$= \frac{12}{\delta}\frac{\partial P}{\partial r}\left(G(\delta)I_0(\delta) - I_2(\delta)\right) \tag{3.42}$$

where

$$G(z) = \frac{\Theta_b z^2}{3\delta^2}\left(3\delta - z\right) \tag{3.43}$$

is a primitive of θ when $z < \delta$ and

$$I_2(z) = \int_0^z \left(\nu + (1-\nu)\theta(y)\right) G(y) \left(y - \frac{h}{2}\right) dy. \tag{3.44}$$

Therefore, we have

$$\overline{u\theta} - \overline{u}\overline{\theta} = \frac{12}{\delta}\frac{\partial P}{\partial r}\left(I_0(\delta)\left(G(\delta) - \delta\overline{\theta}\right) + \overline{\theta} I_1(\delta) - I_2(\delta)\right) \tag{3.45}$$

where the average temperature over a thermal boundary layer is $\overline{\theta} = 2\Theta_b/3$

3.2.8 Summary of the equations

In the end, the coupled equations governing the cooling of an elastic-plated gravity current are

$$\frac{\partial h}{\partial t} - \frac{12}{r}\frac{\partial}{\partial r}\left(rI_1(h)\frac{\partial P}{\partial r}\right) = \mathcal{H}(\frac{\gamma}{2}-r)\frac{32}{\gamma^2}\left(\frac{1}{4}-\frac{r^2}{\gamma^2}\right) \quad (3.46)$$

$$\frac{\partial \xi}{\partial t} + \frac{1}{r}\frac{\partial}{\partial r}\left(r\left(\bar{u}\xi - \Sigma\right)\right) = 2Pe^{-1}St_m\frac{\Theta_b}{\delta} \quad (3.47)$$

with

$$\Theta_b(r) = \begin{cases} 1 & \text{if} \quad \xi \leq \xi_t \\ \frac{3}{2} - \frac{3\xi}{h} & \text{if} \quad \xi > \xi_t \end{cases} \qquad \delta(r) = \begin{cases} 3\xi & \text{if} \quad \xi \leq \xi_t \\ h(r,t)/2 & \text{if} \quad \xi > \xi_t \end{cases}$$

$$\bar{u} = \frac{12}{\delta}\frac{\partial P}{\partial r}\left(\delta I_0(\delta) - I_1(\delta)\right) \quad (3.48)$$

$$\Sigma = \frac{\partial P}{\partial r}\left(8I_1(\delta)\Theta_b - 12I_2(\delta)\right) \quad (3.49)$$

where $P = h + \nabla_r^4 h$ is the dimensionless pressure and $\mathcal{H}$ the Heaviside function. The expression of $I_0(\delta)$, $I_1(h)$, $I_1(\delta)$ and $I_2(\delta)$ as well as the numerical scheme used to solve equations (3.46) and (3.47) are given in appendix **??**.

3.2.9 Preliminary results for an isothermal flow

For a constant injection rate, a small pre-wetting film thickness, i.e. $h_f << 1$ and a viscosity contrast ν set to 1, numerical resolution of (3.46) shows two asymptotic spreading regimes (*Michaut*, 2011; *Lister et al.*, 2013).

At early times, when $R << \Lambda$, gravity is negligible and the spreading dynamics is governed by the bending of the upper layer. The spreading is very slow and the interior has uniform pressure $P = \nabla_r^4 h$. The flow is bell-shaped and its thickness is given by

$$h(r,t) = h_0(t)\left(1 - \frac{r^2}{R^2(t)}\right)^2 \quad (3.50)$$

with $h_0(t)$ the thickness of the current at the center (*Michaut*, 2011; *Lister et al.*, 2013). In this regime, *Lister et al.* (2013) have shown that the spreading is controlled by the propagation of a peeling by bending wave at the flow front with dimensionless velocity c

$$c = \frac{dR}{dt} = h_f^{1/2}\left(\frac{\kappa}{1.35}\right)^{5/2} \quad (3.51)$$

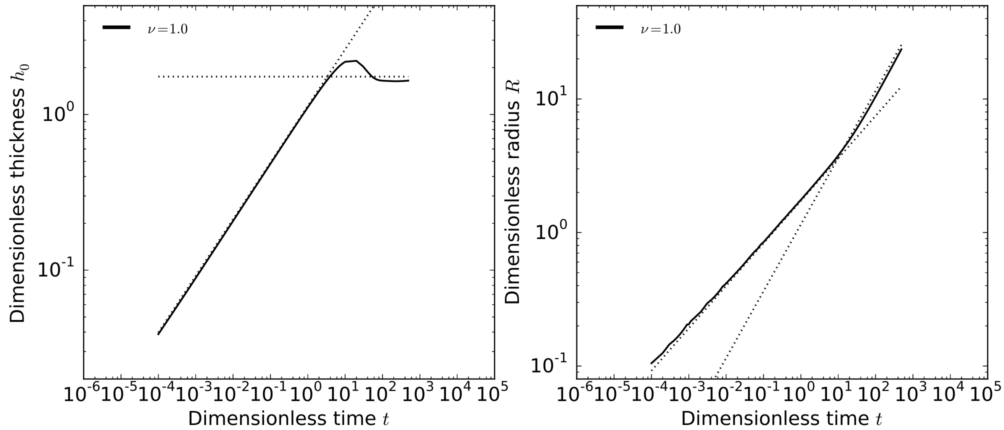

Figure 3.2: Left: Dimensionless thickness at the center h_0 versus dimensionless time t. Dotted-lines: scaling laws in the bending regime $h_0 = 0.7 h_f^{-1/11} t^{8/22}$ and in the gravity regime where h_0 tends to a constant. Right: Dimensionless radius R versus dimensionless time t. Dotted-lines: scaling laws in the bending regime $R = 2.2 h_f^{1/22} t^{7/22}$ and in the gravity current regime $R \propto t^{1/2}$.

where $\kappa = \partial^2 h/\partial r^2$ is the dimensionless curvature of the interior solution. Using the propagation law (3.51) and the form of the interior solution (3.50), *Lister et al.* (2013) predicted that, in this regime, the flow radius and height evolve following

$$h_0(t) = 0.7 h_f^{-1/11} t^{8/22} \quad (3.52)$$
$$R(t) = 2.2 h_f^{1/22} t^{7/22} \quad (3.53)$$

where the numerical pre-factor obtained in our simulations match those of *Lister et al.* (2013) (Figure 3.2).

In contrast, when the radius R becomes larger than 4Λ ($R >> \Lambda$), the weight of the current becomes dominant over the bending terms. The pressure is given by the hydrostatic pressure $P = h$ and the current enters a classical gravity current regime where bending terms only affect the solution near the edge of the current (*Huppert*, 1982a; *Michaut*, 2011; *Lister et al.*, 2013). In this second regime, the radius evolves as $t^{1/2}$ and the thickness tends to a constant (Figure 3.2).

In the following, we study the effect of the cooling on the flow dynamics in both regimes separately. We first describe the thermal structure for an isoviscous flow, i.e. $\nu = 1$ and then study the effect of the temperature-dependent viscosity on the flow dynamics without crystallization, i.e $St_m = 1$. Finally, we introduce crystallization by setting $St_m < 1$. For simplicity, we present the results for a given film thickness ($h_f = 5{\cdot}10^{-3}$); results for different film thicknesses are shown in Appendix **??**.

3.3 Evolution in the bending regime

We first concentrate on the case in which only bending contributes to the dynamic pressure. The governing equations are thus (3.46) and (3.47) where $P = \nabla_r^4 h$.

3.3.1 Thermal structure for an isoviscous flow, effect of Pe

The current cools by conduction and thermal boundary layers form at the contact with the surrounding medium. These boundary layers first connect at the tip of the flow, where the small thickness induces an important cooling (Figure 3.3). A region of cold fluid forms at the front.

As the current thickens with time, a balance between advection and diffusion of heat is never reached in the interior of the current. The hot thermal anomaly grows in extent with time but slower than the current itself and the cold fluid region at the tip grows. For instance, for $Pe = 100$, while the region of cold fluid extends over about 10% of the current at $t = 0.5$, it extends over about 20% at $t = 10$ (Figure 3.3). The smaller Pe, the more important the conductive cooling and the larger the cold region (Figure 3.4 and 3.5). For instance, at $t = 10$, while the cold region extends over about 20% of the current for $Pe = 100$, it extends over more than 70% for $Pe = 1$ (Figure 3.4).

3.3.2 Thickness and temperature profile, effect of ν

When accounting for the temperature dependence of the viscosity, the region of cold fluid at the tip is marked by a higher viscosity and enhances flow thickening at the expense of spreading. The larger the viscosity contrast, the larger the aspect ratio h_0/R (Figure 3.4). For instance, for the same value of $Pe = 1$, while the aspect ratio is 0.7 for $\nu = 1$ at $t = 10$, it is 4.2 at the same time for $\nu = 10^{-3}$ (Figure 3.4). Nevertheless, the shape of the flow remains essentially self-similar, i.e. well described by (3.50) and cannot be differentiated from the shape of an isoviscous current if the thickness and the radial coordinates are rescaled by the thickness at the center $h_0(t)$ and radius $R(t)$ (Figure 3.5).

The flow thermal structure is similar to the isoviscous case (Figure 3.4), the thermal anomaly rapidly detaches from the tip of the current and a region

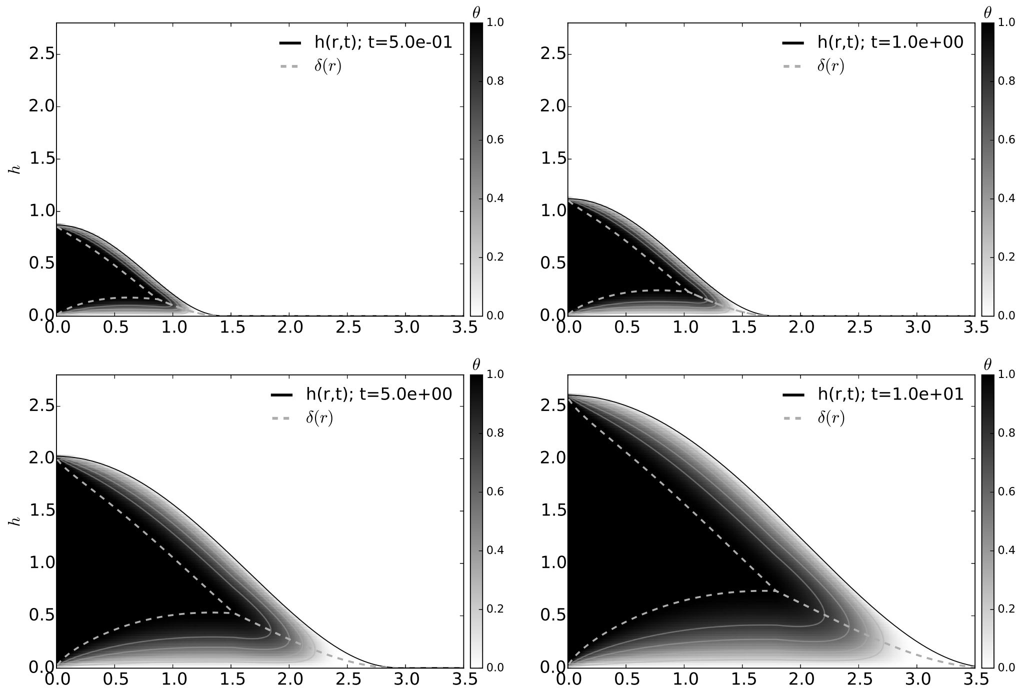

Figure 3.3: Snapshots of the flow thermal structure $\theta(r, z, t)$ at different times indicated on the plot. Dashed lines represent the thermal boundary layers. Solid grey lines are isotherms for $\theta = 0.2$, 0.4, 0.6 and 0.8. Here, $\nu = 1.0$, $Pe = 100$, $St_m = 1$.

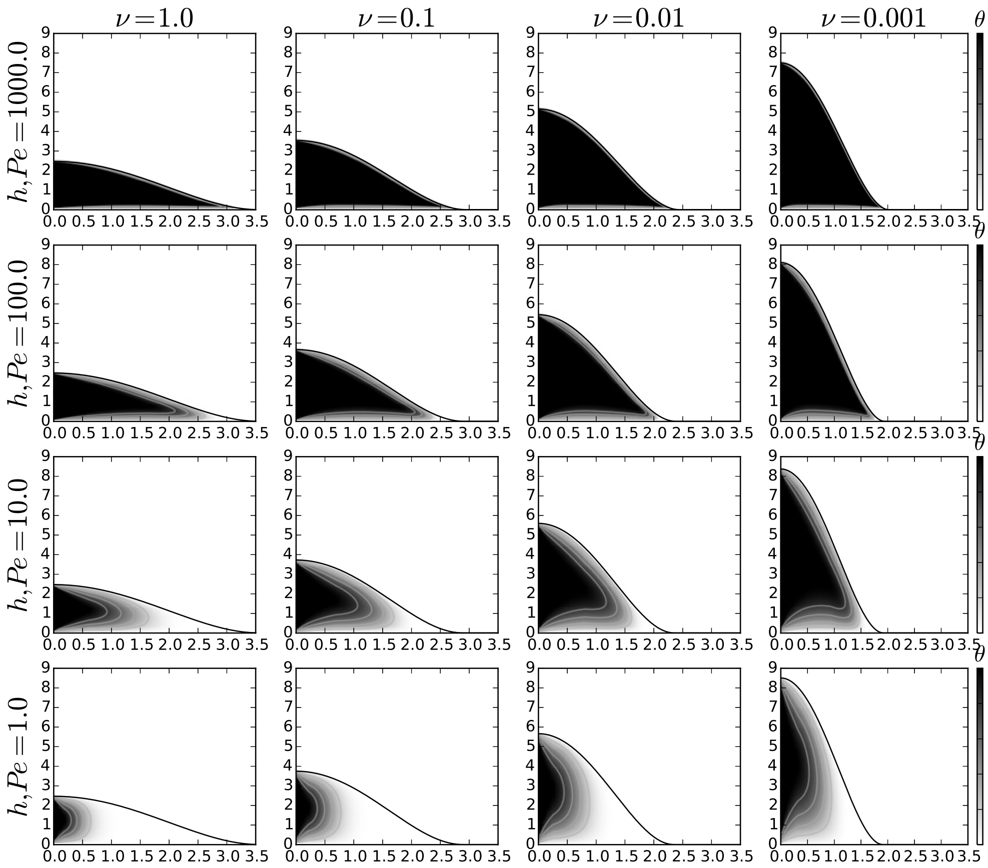

Figure 3.4: Snapshots of the flow thermal structure $\theta(r, z, t)$ for different set (ν,Pe) with ν = 1, 0.1, 0.01 and 0.001 and Pe = 1, 10, 100 and 1000 at t = 10. While Pe controls the thermal structure of the flow, it has only a small influence on the flow aspect ratio which is controlled by ν.

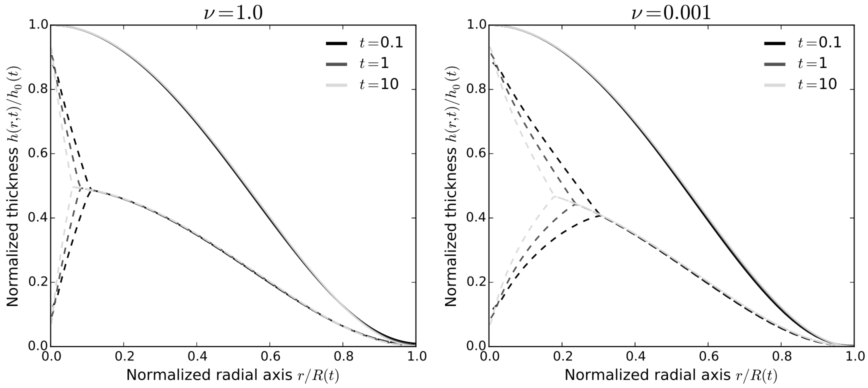

Figure 3.5: Left: thickness normalized by the thickness at the center $h(r,t)/h_0(t)$ versus radial axis normalized by the current radius $r/R(t)$ at different times indicated on the plot for $Pe = 1.0$ and $\nu = 1.0$. Solid-lines represent the thickness profiles. Dashed-lines represent the thermal boundary layers. Right: Same plot but for $\nu = 10^{-3}$.

of cold fluid develops at the front where heat loss is the largest. However, the important thickening induced by the viscosity increase limits heat loss to the surrounding. The larger the viscosity contrast ν, the more important the thickening and the larger the thermal anomaly at a given time. For instance, for $Pe = 1$, while the thermal anomaly extends over about 30% of the flow for $\nu = 1$ at $t = 10$, it extends over more than 50% for $\nu = 10^{-3}$ (Figure 3.4).

As expected, a larger Peclet number leads to a larger thermal anomaly (Figure 3.4). However, although different Peclet numbers cause very different thermal structures, the influence of the Peclet number on the flow morphology is small, much smaller than the effect of the viscosity contrast ν (Figure 3.4). For instance, for $\nu = 10^{-3}$ at $t = 10$, the thermal anomaly is still attached to the tip of the current for $Pe = 1000$ whereas it makes about 50% of the current for $Pe = 1$; but, the thickness h_0 and the radius R in both cases differ only by a few percents (Figure 3.4). This suggests that, in this regime, the spreading of the flow is not controlled by the mean temperature or average viscosity of the flow.

3.3.3 Evolution of the thickness and the radius

In this bending dominated regime, the dynamics show three different spreading phases. The thickness as well as the radius first follow the isoviscous scaling laws for a hot viscosity current $h_0 \propto t^{8/22}$ (3.52) and $R \propto t^{7/22}$ (3.53) (Figure 3.6). In the second phase, thickening occurs at the expense of spread-

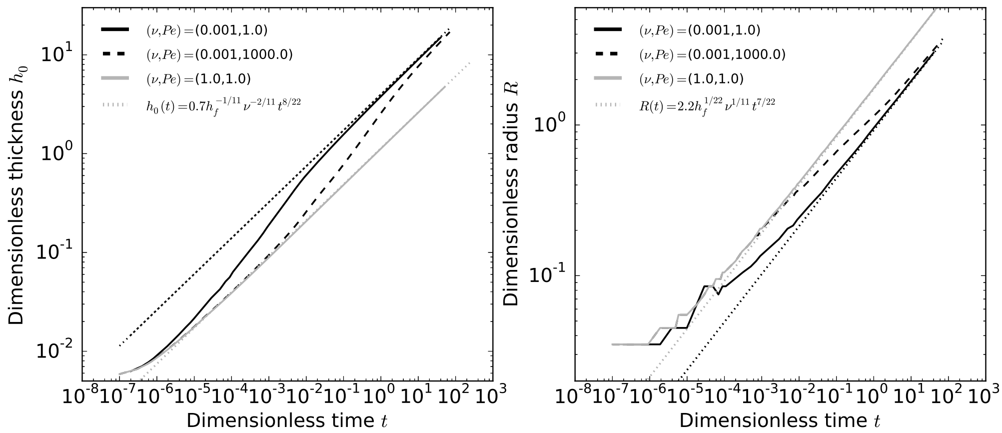

Figure 3.6: Left: Dimensionless thickness at the center h_0 versus dimensionless time t for different sets (ν, Pe) indicated on the plot. Dotted-lines: scaling laws $h_0 = 0.7h_f^{-1/11}\nu^{-2/11}t^{8/22}$ for $\nu = 1.0$ and 0.001. Right: Dimensionless radius R versus dimensionless time t for the same sets of values (ν, Pe). Dotted-lines: scaling laws $R = 2.2h_f^{1/22}\nu^{1/11}t^{7/22}$ for $\nu = 1.0$ and 0.001.

ing because the thermal anomaly has detached from the current radius and the viscous cold fluid region at the front slows down the spreading. Finally, the dynamics enters a third phase where the thickness and radius follow the scaling laws for the spreading of an isoviscous current characterized by a dimensionless cold viscosity $1/\nu$. These scaling laws are obtained from (3.52) and (3.53) by rescaling the characteristic thickness and time by $\nu^{1/4}$ and read

$$h_0 = 0.7\nu^{-2/11}h_f^{-1/11}t^{8/22} \tag{3.54}$$
$$R = 2.2\nu^{1/11}h_f^{1/22}t^{7/22}. \tag{3.55}$$

The dependence on the viscosity contrast ν indeed fits very well the third phase of the flow observed in the numerical simulations (Figure 3.6). In the end, the effective viscosity η_e of the flow evolves from the viscosity of the hot fluid in the first phase to asymptotically tend to the one of the cold fluid in the third phase.

The time the flow spends in each phase depends on the Peclet number Pe. For instance, for $\nu = 10^{-3}$, while the current leaves the first phase at $t \sim 10^{-6}$ for $Pe = 1.0$, this transition happens only after $t \sim 10^{-2}$ for $Pe = 10^3$ (Figure 3.6). The larger the Peclet number, the less efficient the cooling and thus the longer the flow remains in the first phase and the later it reaches the third phase.

3.3.4 Characterization of the thermal anomaly

Following *Garel et al.* (2012), we quantify the size of the thermal anomaly through a critical thermal radius $R_c(t)$ where the temperature at the center of the flow Θ_b is 1% of the injection temperature, i.e. $\Theta_b(r=0)-\Theta_b(r=R_c)=0.99$. The thermal anomaly is first advected at the same velocity as the current itself, i.e. $R(t)=R_c(t)$ (Figure 3.7 left). After a time that depends on Pe and ν, the thermal anomaly detaches from the tip and $R(t)-R_c(t)$ increases with time (Figure 3.7) .

In the bending regime, the interior pressure is constant and the thickness profile $h(r)$ is given by (3.50) (Figure 3.5). The time evolution of the size of the thermal anomaly $R_c(t)$ is characterized by looking at the radius in the flow where heat advection locally balances heat loss, i.e.

$$\frac{d}{dt}\left(\Theta_b h\right) \approx Pe^{-1}\frac{\Theta_b}{h}. \tag{3.56}$$

Using the thickness profile (3.50), (3.56) becomes

$$\alpha^2\left(1+\frac{R_c}{R}\right)^2\left(\Theta_b\frac{dh_0}{dt}+h_0\frac{d\Theta_b}{dt}\right)+\frac{4h_0R_c^2\Theta_b}{R^3}\frac{dR}{dt}\alpha\left(1+\frac{R_c}{R}\right)\approx\frac{Pe^{-1}\Theta_b}{\alpha^2\left(1+\frac{R_c}{R}\right)^2h_0}$$

where $\alpha(t)=\left(R(t)-R_c(t)\right)/R(t)$ is the normalized region beyond $r=R_c(t)$. In the limit $\alpha<<1$, i.e. $R_c/R\sim 1$, the time derivative is locally dominated by its advective part ($\propto\alpha$) and we finally get

$$\alpha^3\approx\frac{Pe^{-1}}{h_0^2(t)}\frac{R}{\frac{\partial R}{\partial t}}. \tag{3.57}$$

Substituting $h_0(t)$ and $R(t)$ by their respective scaling laws (3.54) and (3.55), the size evolution of the normalized cold front region α reads

$$\alpha(t)\approx Pe^{-1/3}\nu^{4/33}h_f^{2/33}t^{1/11}. \tag{3.58}$$

which is equivalent to

$$R(t)-R_c(t)=2.1Pe^{-1/3}\nu^{7/33}h_f^{7/66}t^{9/22} \tag{3.59}$$

where the numerical prefactor, which depends on the definition of the thermal anomaly, has been chosen to fit the simulations.

The predicted scaling law for the evolution of the cold fluid region (3.59) indeed closely fits the numerical simulations for $\nu<1$ and for different Peclet numbers (Figure 3.7). For $\nu=1$ and $Pe=1$, the condition $R-R_c<<R$ is no more respected for $t>0.1$, the thermal anomaly is much smaller than the flow itself and the evolution of the cold fluid region diverges from (3.59).

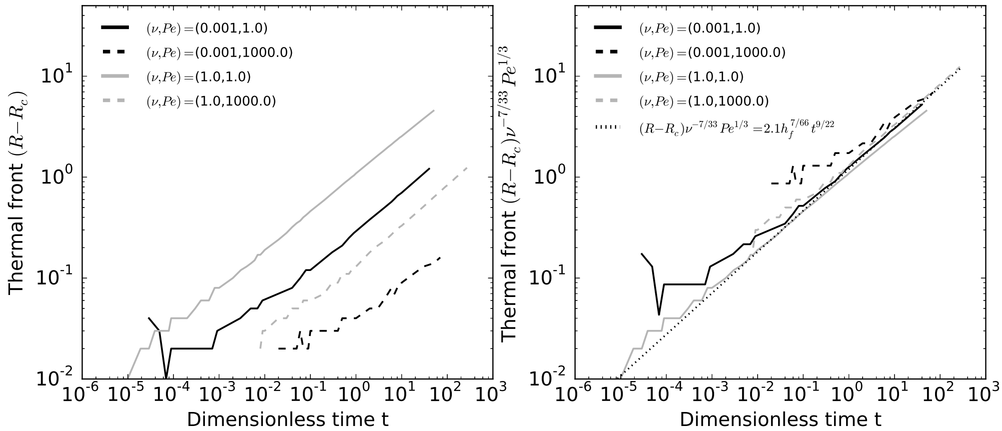

Figure 3.7: Left: Extent of the cold fluid region $R(t)-R_c(t)$ versus dimensionless time for different combinations (ν,Pe) indicated on the plot. Right: Same plot but where we rescale the extent of the cold fluid region by $Pe^{-1/3}\nu^{7/33}$. Dotted-line: scaling law $(R(t)-R_c(t))Pe^{1/3}\nu^{-7/33} = 2.1h_f^{7/66}t^{9/22}$.

3.3.5 Effective viscosity of the current

We use the predicted scaling law for the thickness $h_0(t)$ (3.54) to infer the time evolution of the effective viscosity $\eta_e(t)$. Substituting ν by $\eta_h/\eta_e(t)$ in (3.54) and inverting for $\eta_e(t)/\eta_h$, we get

$$\eta_e(t)/\eta_h = \left(\frac{h_0(t)t^{-8/22}}{0.7h_f^{-1/11}}\right)^{11/2} \tag{3.60}$$

where $h_0(t)$ is given by the simulation.

As suggested by the results of section 3.3.3, the effective viscosity is first close to the hot viscosity η_h, i.e. $\eta_e/\eta_h \sim 1$ (Figure 3.8 a). It rapidly increases in the second phase of propagation and finally tends to the cold viscosity η_c in the third phase, i.e. $\eta_e/\eta_h \sim 1/\nu$. The effective viscosity is however very different from the average viscosity (Figure 3.8 a). Since the spreading is controlled by the propagation of a peeling by bending wave at the tip of the current (*Lister et al.*, 2013), the evolution of the effective viscosity should be linked to the rapid cooling of the front. We calculate the average viscosity $\eta_f(t)$ over a fixed front region of size L in between $R(t)-L$ and $R(t)$

$$\eta_f/\eta_h = \frac{1}{V_f}\int_{R-L}^{R}\int_0^h r\eta(\theta)drdz \tag{3.61}$$

where $V_f(t)$ is the volume of this region. The numerical evaluation of $\eta_f(t)$ for a constant size $L \sim 0.1$ fits relatively well the evolution of the effective

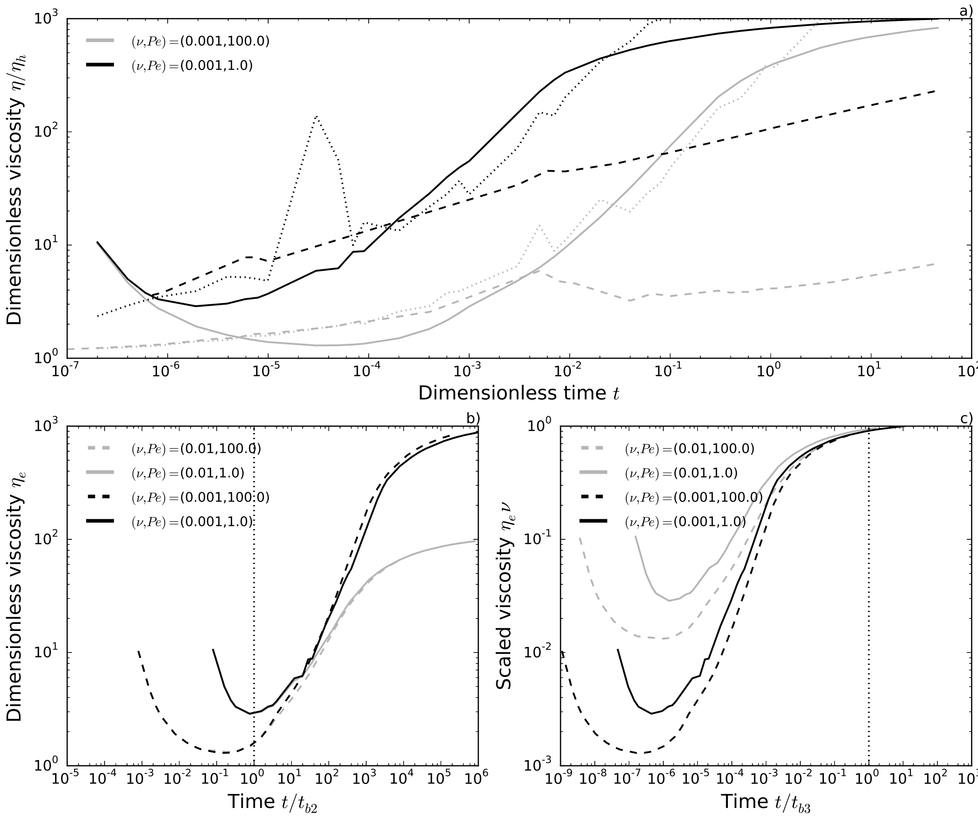

Figure 3.8: a) Dimensionless viscosity $\eta(t)/\eta_h$ versus dimensionless time t for different combinations (ν, Pe) indicated on the plot. Solid lines: effective viscosity η_e/η_h defined by (3.60). Dashed-lines: average flow viscosity defined by $\overline{\eta_a(t)}/\eta_h = \frac{1}{V(t)}\int_0^{R(t)}\int_0^{h(r,t)} r\eta(\theta)drdz$ where $V(t)$ is the current volume. Dotted-lines: average front viscosity η_f/η_h defined by (3.61). b) Dimensionless effective viscosity η_e versus time where the time has been rescaled by the time for the flow to enter the second phase t_{b2}. c) Same as left but where the time has been rescaled by the time for the flow to enter the third phase t_{b3}.

viscosity η_e for the second phase of propagation (Figure 3.8 a). Therefore, the effective viscosity, and thus the different phases of propagation, are controlled by the average viscosity of a small region at the front of size $L = O(0.1)$.

At the initiation of the flow, the prewetting film is composed by fluid at the injection temperature, the thermal anomaly is attached to the front and the current spreads with a hot viscosity η_h. Once the film has cooled by conduction, which occurs over a time $t_{b2} = 0.1 Pe h_f^2$, where the numerical prefactor has been matched to the simulations, the thermal anomaly detaches from the current tip and the effective viscosity starts to increase. Indeed, when rescaling the time of the simulations by t_{b2}, the different simulations enter the second phase simultaneously (Figure 3.8 b). Then, the size of the cold fluid region at the front increases, the effective viscosity increases and the flow finally behaves as an isoviscous current when its effective viscosity becomes close to its maximum value $1/\nu$. In the following, we use $\eta_e = 0.9\eta_c$ to determine the time t_{b3} the current enters this third phase which happens when $R(t) - R_c(t) \lesssim 0.5$. Inverting (3.59) thus gives $t_{b3} \sim 0.03 Pe^{22/27}\nu^{-14/27}h_f^{-7/27}$. Indeed, when rescaling the time of the simulations by t_{b3}, the different simulations enter the third phase simultaneously (Figure 3.8 c).

3.3.6 Note on the effect of crystallization

Here, we examine the effect of crystallization on the flow dynamics and use a value of $St_m = 0.17 < 1$, relevant for magmas. Crystallization induces a release of latent heat in the fluid, increasing the amount of available energy at a given time. When $St_m < 1$, the tip of the current remains hot for a longer time and the flow transitions to the second phase later than in the case where $St_m = 1$ (Figure 3.9). As the crystallization acts only to reduce the cooling term by a factor St_m in (3.47), one can easily rewrite (3.59) to acount for the effect of crystallization on the size of the cold fluid region

$$R(t) - R_c(t) = 2.1 Pe^{-1/3} St_m^{1/3} \nu^{7/33} h_f^{7/66} t^{9/22}. \tag{3.62}$$

Indeed, the dependence with the dimensionless number St_m is well described by the scaling law (3.62) (Figure 3.10). Accordingly, the time t_{b2} and t_{b3} for the current to enter the second and third phase of the flow are delayed when accounting for crystallization and respectively read

$$t_{b2} \sim 0.1 Pe St_m^{-1} h_f^2 \tag{3.63}$$

$$t_{b3} \sim 0.03 St_m^{-22/27} Pe^{22/27} \nu^{-14/27} h_f^{-7/27} \tag{3.64}$$

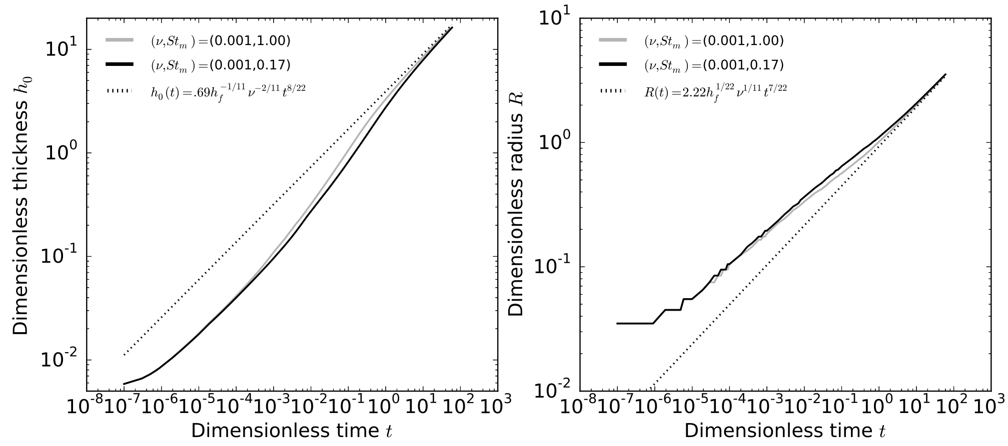

Figure 3.9: Left: Dimensionless thickness at the center h_0 versus dimensionless time t for different values of St_m indicated on the plot, $\nu = 0.001$ and $Pe = 10.0$. Dotted-line: scaling law $h_0 = 0.7 h_f^{-1/11} \nu^{-2/11} t^{8/22}$ for $\nu = 0.001$. Right: Dimensionless radius R versus dimensionless time t for the same combinations of dimensionless numbers. Dotted lines: scaling law $R = 2.2 h_f^{1/22} \nu^{1/11} t^{7/22}$ for $\nu = 0.001$.

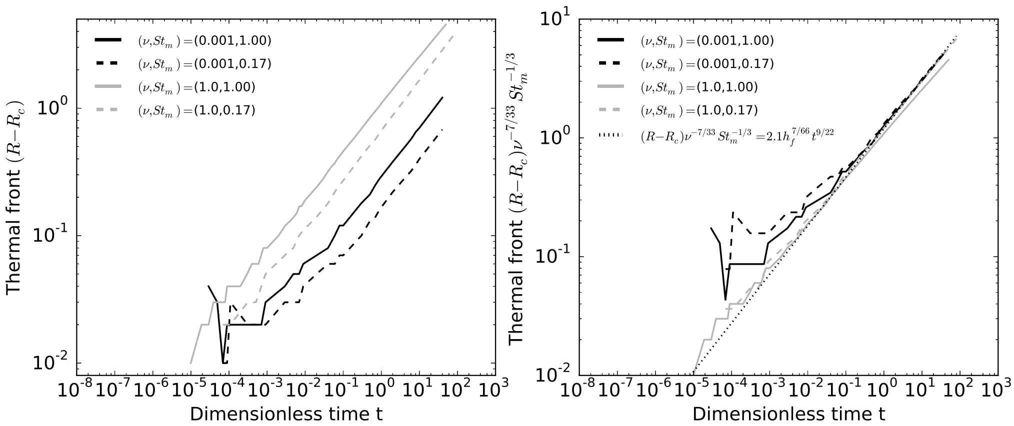

Figure 3.10: Left: Extent of the cold fluid region $R(t) - R_c(t)$ versus dimensionless time for different combinations (ν, St_m) indicated on the plot and $Pe = 1$. Right: Same plot but where we have rescaled the extent of the cold fluid region by $St_m^{1/3} \nu^{7/33}$. Dotted-line: scaling law $(R(t) - R_c(t)) St_m^{-1/3} \nu^{-7/33} = 2.1 h_f^{7/66} t^{9/22}$.

3.4 Evolution in the gravity current regime

To study the late time behavior, we concentrate on the case where only the weight of the fluid contributes to the pressure. The governing equations are thus (3.46) and (3.47) where $P = h$. We follow the same framework as in Section 3.3.

3.4.1 Thermal structure for an isoviscous flow, effect of Pe

As in the bending regime, the bulk of the fluid first expands at the injection temperature and $R_c(t) \sim R(t)$. As the bottom and the top cool by conduction, thermal boundary layers form at the contact with the surrounding medium and connect at the tip of the current. However, in the gravity current regime, the thickness of the current tends to a constant. Therefore, conduction in the surrounding medium rapidly balances the input of heat at the center and when the thermal anomaly detaches from the tip of the current, its extent reaches a steady state (Figure 3.11).

The radius of the steady-state thermal anomaly R_c also largely depends on Pe in this regime: the larger the number Pe, the larger the radius R_c (Figure 3.12). For instance, while the thermal anomaly R_c is less than 1 in the steady state regime for $Pe = 1$, it is about 12 for $Pe = 10^3$ (Figure 3.12, $\nu = 1$).

3.4.2 Thickness and temperature profile, effect of ν

For a current with a viscosity that depends on temperature, as soon as the thermal anomaly detaches from the current radius, the cold fluid at the front tends to slow down the spreading and enhance the thickening of the flow (Figure 3.12). For instance, for $Pe = 1$, while the aspect ratio h_0/R is about 0.12 for $\nu = 1$ at $t = 200$, it is ~ 1 for $\nu = 10^{-3}$ (Figure 3.12). The shape of the current is not self-similar and the front steepens when the viscosity increases in comparison to the isoviscous case as noted by *Bercovici* (1994). However, when the current becomes much larger than the thermal anomaly, the current side slumps to become less steep (Figure 3.12) and recovers a shape similar to the isoviscous flow with cold viscosity.

The thermal structure is similar to the isoviscous case. In particular, after a time that depends on Pe, the thermal anomaly reaches a steady-state profile (Figure 3.12). As in the bending regime, the thickening at the center limits heat loss to the surrounding for large values of the viscosity contrast ν. Therefore, the extent of the thermal anomaly in the steady-state is slightly larger for a larger viscosity contrast. For instance, for $Pe = 10$ at $t = 200$,

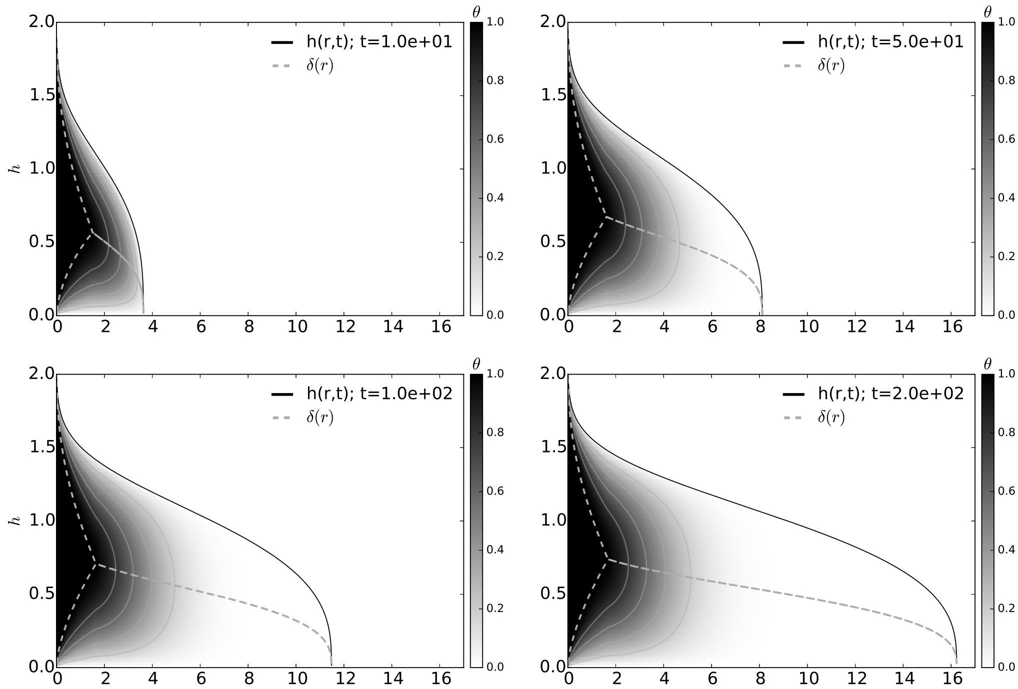

Figure 3.11: Snapshots of the flow thermal structure $\theta(r, z, t)$ at different times indicated on the plot. Dashed lines: thermal boundary layers. Here, $\nu = 1$, $Pe = 100$ and $St_m = 1$.

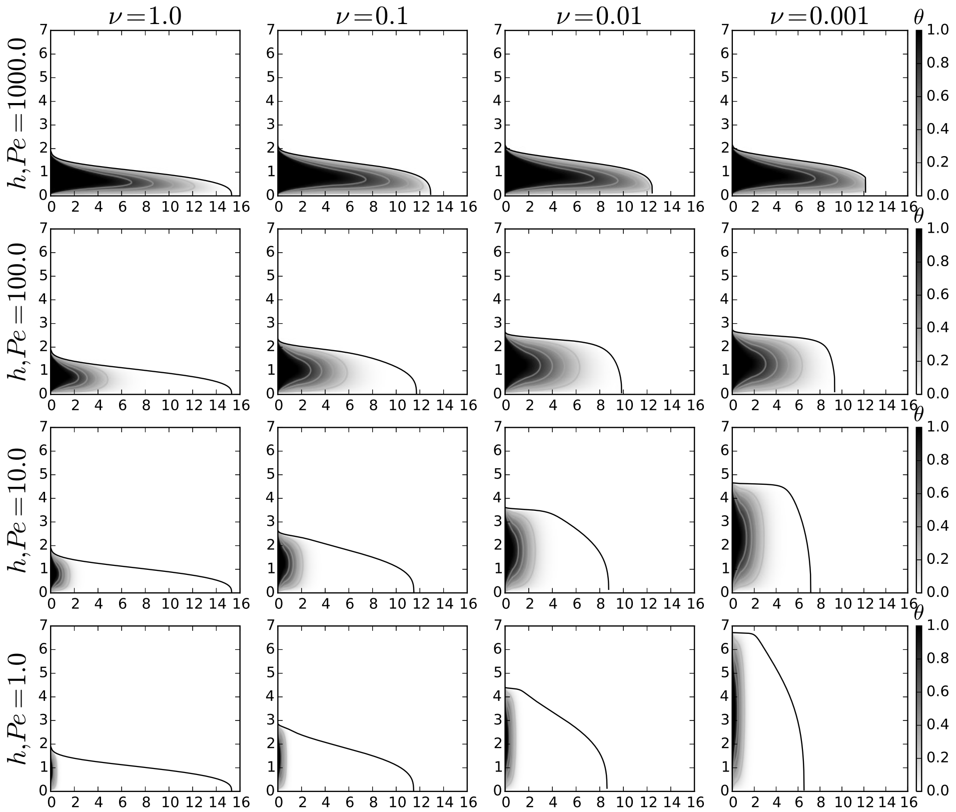

Figure 3.12: Snapshots of the flow thermal structure $\theta(r, z, t)$ for different sets (ν,Pe) with $\nu = 1$,0.1 ,0.01 and 0.001 and $Pe = 1$, 10, 100 and 1000 at $t = 200$.

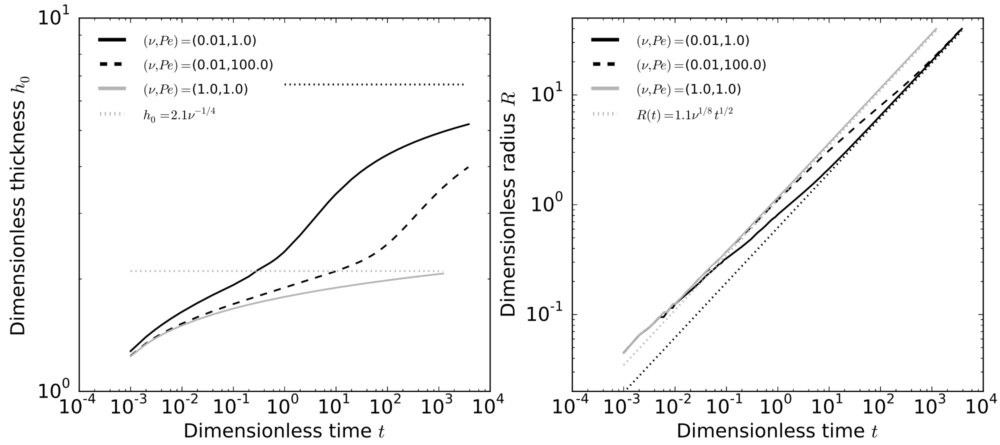

Figure 3.13: Left: Dimensionless thickness at the center h_0 versus dimensionless time t for different sets (ν, Pe) indicated on the plot. Dotted-lines represent the scaling laws $h_0 = 2.1\nu^{-1/4}$ for $\nu = 1.0$ and 10^{-2}. Right: Dimensionless radius R versus dimensionless time t for the same sets (ν, Pe). Dotted-lines represent the scaling laws $R = 1.1\nu^{1/8}t^{1/2}$ for $\nu = 1.0$ and 10^{-2}.

while the thermal anomaly extends over less than 2 for $\nu = 1$, it reaches $Rc \sim 3$ for $\nu = 10^{-3}$.

The flow morphology is much more sensitive to Pe in the gravity current regime than in the bending regime and different Pe lead to different current morphologies for a given ν (Figure 3.12). For instance, for $\nu = 10^{-3}$ at $t = 200$, the thermal anomaly is still attached to the tip for $Pe = 10^3$ and the aspect ratio of the flow h_0/R is close to 0.15. In contrast, for $Pe = 1$, the thermal anomaly radius R_c is less than 30% of the current radius and the aspect ratio of the flow is much larger $h_0/R = 1.15$ (Figure 3.12).

3.4.3 Evolution of the thickness and radius

As in the bending regime, the dynamics in the gravity current regime shows three different spreading phases. The thickness as well as the radius first follow the isoviscous scaling laws for a given hot viscosity η_h, i.e. h_0 tends to a constant and $R \propto t^{1/2}$ (Figure 3.13). In a second phase, the thickness rapidly increases and the spreading slows down. Finally, the thickness and radius follow the isoviscous scaling laws but for a cold viscosity flow.

These dimensionless scaling laws read, as a function of ν

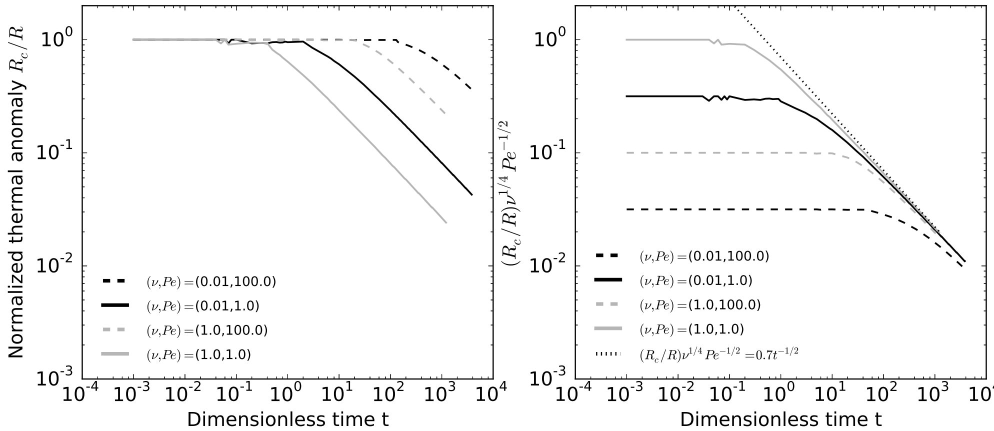

Figure 3.14: Left: Normalized thermal anomaly radius $R_c(t)/R(t)$ versus dimensionless time for different combinations (ν,Pe) indicated on the plot. Right: Same plot but where we rescale the normalized thermal anomaly radius $R_c(t)/R(t)$ by $Pe^{1/2}\nu^{-1/4}$.

$$h_0 = 2.1\nu^{-1/4} \quad (3.65)$$
$$R(t) = 1.1\nu^{1/8}t^{1/2} \quad (3.66)$$

They perfectly match our numerical simulations (Figure 3.13). Therefore, the effective viscosity η_e that controls the flow dynamics is first close to the viscosity of the hot fluid η_h; it then rapidly increases to asymptotically tend to the viscosity of the cold fluid η_c in the third phase.

As in the bending regime, the time the current spends in each phase depends on Pe (Figure 3.13). For instance, for $\nu = 10^{-2}$, while the current leaves the first phase at $t \sim 10^{-1}$ for $Pe = 1.0$, the transition occurs after $t \sim 10^1$ for $Pe = 10^2$ (Figure 3.13). The larger the Pe, the longer the current remains in the first phase and the later is reached the third phase.

3.4.4 Characterization of the thermal anomaly

The thermal anomaly is first advected at the same velocity as the current itself, i.e. $R_c(t)/R(t) \sim 1$ (Figure 3.14 left). After a time that depends on Pe and ν, the thermal anomaly detaches from the front and reaches a steady-state profile (Figure 3.12 and 3.14).

We develop a simple thermal budget to predict the extent of the thermal anomaly in the steady-state regime. At the steady state radius R_c of the thermal anomaly, a balance between heat advection and diffusion in the surrounding medium in a dimensional form gives

$$\rho C_p U_0 \frac{\Delta T}{R_c} \approx \frac{8k\Delta T}{h_0^2} \tag{3.67}$$

where ΔT is a mean temperature contrast between the fluid and the surroundings and U_0 is a mean velocity of advection. For a gravity current, and by opposition to the bending regime, the thickness h_0 reaches a constant. Taking U_0 as a horizontal redistribution of the injection rate at $r = R_c$, we write

$$U_0 = Q_0/(2\pi R_c h_0) \tag{3.68}$$

which gives

$$R_c \approx \frac{1}{4}\sqrt{\frac{h_0 Q_0}{\pi\kappa}} \tag{3.69}$$

By non-dimensionalizing (3.69), we obtain the evolution of the steady-state radius $R_c \approx Pe^{1/2}\nu^{-1/8}$ and hence

$$\frac{R_c}{R(t)} = 0.7Pe^{1/2}\nu^{-1/4}t^{-1/2} \tag{3.70}$$

where we have used (3.66) and the numerical prefactor, which depends on the definition of the thermal anomaly, has been chosen to fit the simulations.

The scaling law (3.70) closely fits the numerical simulations (Figure 3.14). Indeed, when the thermal anomaly enters the steady state, the thermal anomaly radius remains constant and the normalized thermal anomaly radius $R_c(t)/R(t)$ evolves as the inverse of the current radius, i.e. as $t^{-1/2}$ (Figure 3.14). Furthermore, both the dependence with Pe and ν vanish when rescaling $R_c/R(t)$ by $Pe^{1/2}\nu^{-1/4}$ in the steady state regime (Figure 3.14, right).

3.4.5 Effective viscosity of the current

Repeating the same exercise as in section (3.3.5), we use the predicted scaling law for the radius $R(t)$ (3.66) to infer the effective viscosity $\eta_e(t)$ of the current

$$\eta_e(t)/\eta_h = \left(\frac{R(t)t^{-1/2}}{1.1}\right)^{-8} \tag{3.71}$$

where $R(t)$ is given by the simulation.

As expected, the effective viscosity in the gravity current regime represents the average viscosity of the current and the different phases of propagation reflect changes in the average viscosity of the flow (Figure 3.15 a).

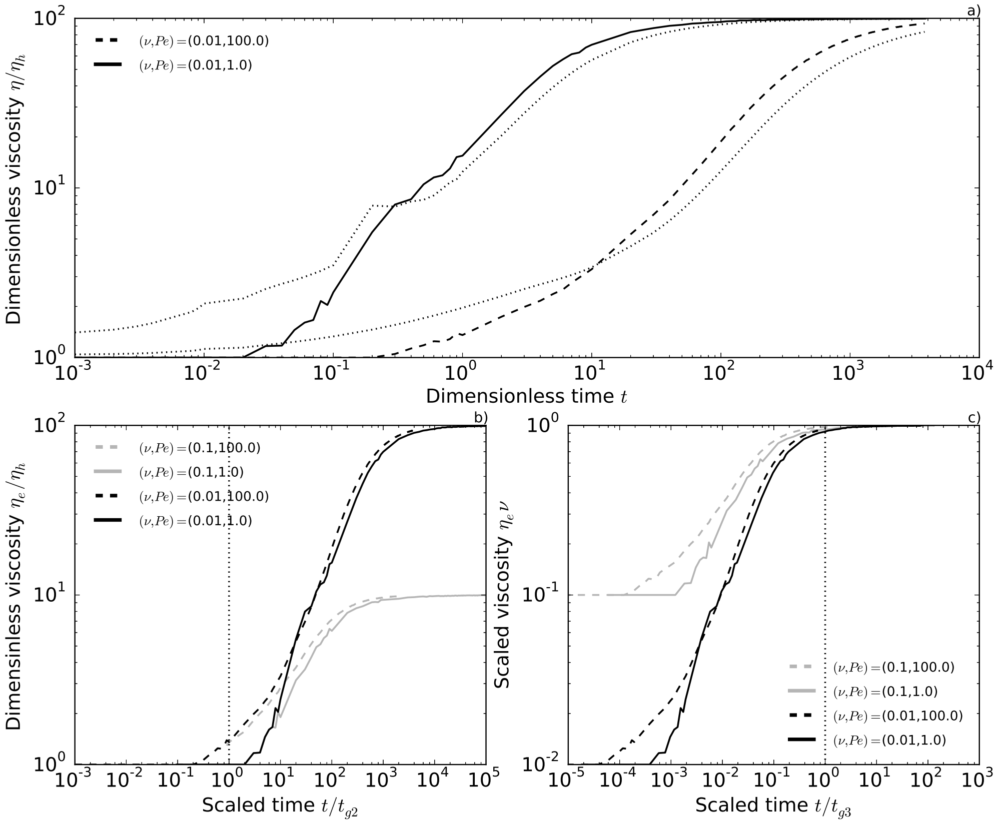

Figure 3.15: a) Dimensionless viscosity $\eta(t)/\eta_h$ defined by (3.60) versus dimensionless time t for different combinations (ν, Pe) indicated on the plot. Black dotted-lines: average flow viscosity defined by $\overline{\eta_a(t)}/\eta_h = \frac{1}{V(t)}\int_0^{R(t)}\int_0^{h(r,t)} r\eta(\theta)drdz$ where $V(t)$ is the current volume. b) dimensionless effective viscosity η_e versus time where the time has been rescaled by the time t_{g2} (3.73). c) Same as left but where the time has been rescaled by t_{g3} (3.74).

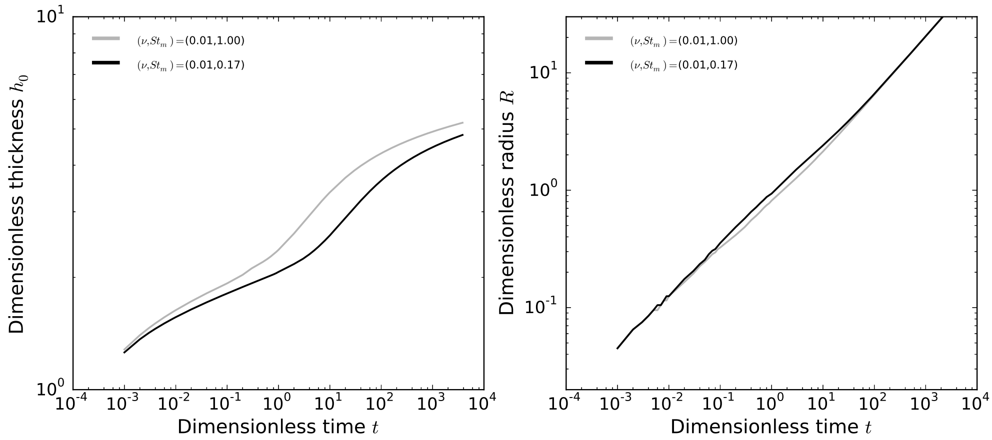

Figure 3.16: Left: Dimensionless thickness at the center h_0 versus dimensionless time t for different sets (ν, St_m) indicated on the plot and $Pe = 1$. Right: Dimensionless radius R versus dimensionless time t for the same sets (ν, St_m) and $Pe = 1$.

At the flow initiation, the thermal anomaly is advected at the same velocity as the current itself and the current spreads with hot viscosity η_h. When the thermal anomaly detaches from the tip and enters a steady state, η_e increases. The time t_{g2} to enter this second phase scales with the time to cool the current by conduction, i.e. $t_{g2} = 10^{-2} Pe$ where the numerical pre-factor has been matched to the simulations. Indeed, when rescaling the time by t_{g2}, the different simulations enter the second phase simultaneously (Figure 3.15 b). Then, the size of the cold fluid region at the front increases, the effective viscosity increases and the flow finally behaves as an isoviscous current when its effective viscosity becomes close to its maximum value $1/\nu$. As in the bending regime, we use $\eta_e = 0.9\eta_c$ to define the time t_{g3} the current enters the third phase of the dynamics which happens when $R_c(t)/R(t) \lesssim 0.3$. Inverting (3.70) thus gives $t_{g3} = 5.2 Pe \nu^{-1/2}$. Indeed, when rescaling the time of the simulations by t_{g3}, the different combinations (ν, Pe) enter the third phase simultaneously (Figure 3.15 c).

3.4.6 Note on the effect of crystallization

As in the bending regime, crystallization induces a release of latent heat, increasing the amount of available energy at a given time. As a result, when $St_m < 1$, the current is hotter on average and it transitions to the second phase later than in the case where $St_m = 1$ (Figure 3.16). As in section (3.3.6), one can easily rewrite (3.70) to account for the effect of crystallization

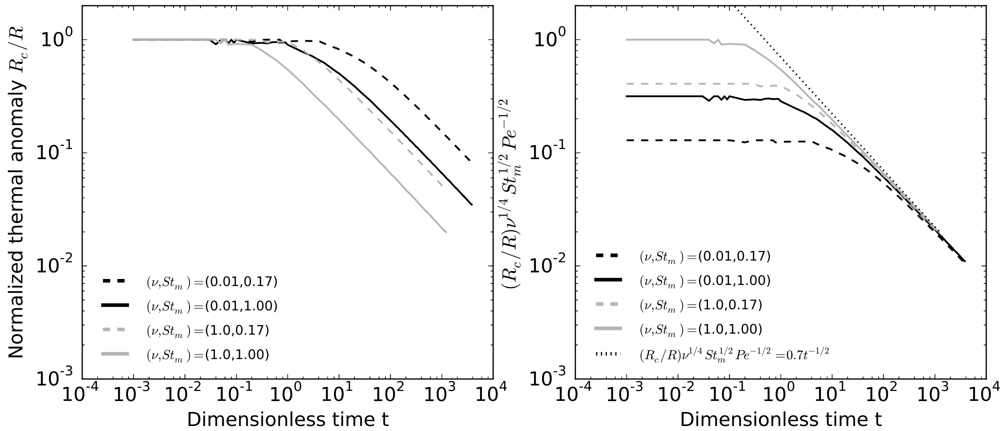

Figure 3.17: Left: Normalized thermal anomaly radius $R_c(t)/R(t)$ versus dimensionless time for different combinations (ν, St_m) indicated on the plot and $Pe = 1$. Right: Same plot but where we have rescaled the normalized thermal anomaly radius $R_c(t)/R(t)$ by $St_m^{-1/2}Pe^{1/2}\nu^{-1/4}$.

on the thermal anomaly evolution

$$\frac{R_c}{R(t)} = 0.7St_m^{-1/2}Pe^{1/2}\nu^{-1/4}t^{-1/2} \tag{3.72}$$

Indeed, the dependence with the dimensionless number St_m is well described by the scaling law (3.72) (Figure 3.17). Accordingly, the time t_{g2} and t_{g3} for the current to enter the second and third phase of the flow are both delayed and respectively read

$$t_{g2} \sim 10^{-2}PeSt_m^{-1} \tag{3.73}$$

$$t_{g3} \sim 5.2PeSt_m^{-1}\nu^{-1/2} \tag{3.74}$$

3.5 Different evolutions with bending and gravity

For an isoviscous flow with $h_f << h << d_c$, in between the bending and gravity regime, *Lister et al.* (2013) also describe a short intermediate regime where the peeling by bending continues to control the propagation but where the flow shows an interior flat-topped region due to the increasing effect of gravity. For simplicity, we only consider the two asymptotic regimes. At the transition, the isoviscous current is characterized by $R \sim 4$ and for $h_f = 0.005$,

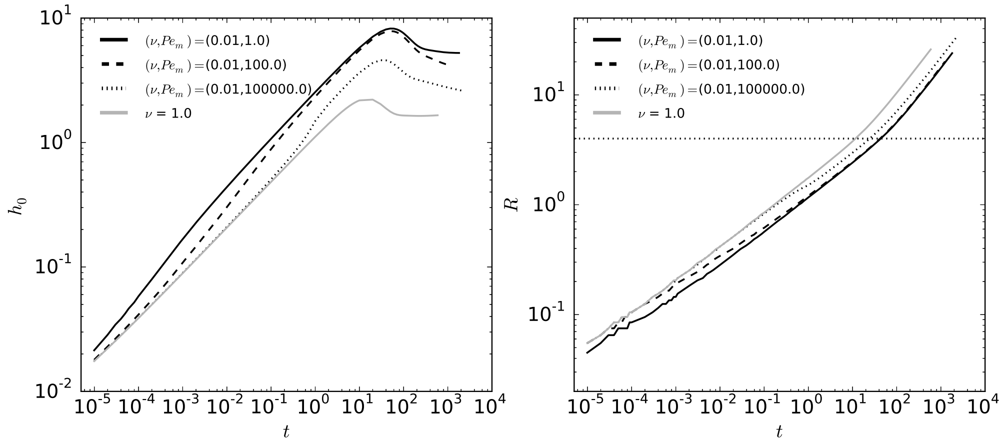

Figure 3.18: Left: Dimensionless thickness at the center h_0 versus dimensionless time for different sets (ν, Pe) indicated on the plot. The grey line represents the isoviscous case $\nu = 1$. Right: Same plot but for the dimensionless radius R. Horizontal black dotted-line represents the transition radius between the bending and the gravity regime.

$h_0 \sim 2$ and $t \sim 10$. In the following, we consider a modified Peclet number $Pe_m = PeSt_m^{-1}$ which integrates the effect of crystallization for clarity.

For a current with a temperature-dependent viscosity, the transition between the bending regime and the gravity regime also occurs when the radius of the current reaches $R \sim 4$ (Figure 3.18). However, the current thickness and time at the transition depend on the thermal state of the flow, i.e. on the combination of (ν,Pe_m) considered (Figure 3.18). For instance, for $\nu = 0.01$ and a small value of Pe, i.e. $Pe = 1.0$, the current transitions to the gravity regime at $t \sim 50$ with $h_0 \sim 8$ while in the third thermal phase of the bending regime. It is then characterized by a cold viscosity $\eta_c = 100$ and a large aspect ratio. In contrast, for a larger value of Pe, i.e. $Pe = 10^5$, the current remains longer in the first phase of the bending regime and it spreads with hot viscosity η_h for a longer period of time. As a consequence, it reaches $R \sim 4$ and enters the gravity regime sooner at $t \sim 30$ while in the second phase of the bending regime and hence characterized by a smaller thickness $h_0 \sim 5$ and a smaller aspect ratio. For even larger Peclet number Pe, the current would transition while in the first thermal phase of the bending regime at $t \sim 10$ and with $h_0 \sim 2$, as in the isoviscous case with viscosity η_h.

Overall, the time for the current to reach the transition t_t is the time for its radius to reach $R(t) = 4$. Setting (3.55) equal to 4, we obtain $t_t = 6.5(\eta_e/\eta_h)^{2/7} h_f^{-1/7}$ where η_e is the effective viscosity of the current (see Section

Name	From	To	Expression
t_t	Bending	Gravity	$6.5(\eta_e/\eta_h)^{2/7}h_f^{-1/7}$
t_t^h	Bending	Gravity	$6.5h_f^{-1/7}$
t_t^c	Bending	Gravity	$6.5\nu^{-2/7}h_f^{-1/7}$
Bending regime			
t_{b2}	Phase 1	Phase 2	$0.1PeSt_m^{-1}h_f^2$
t_{b3}	Phase 2	Phase 3	$0.03St_m^{-22/27}Pe^{22/27}\nu^{-14/27}h_f^{-7/27}$
Gravity regime			
t_{g2}	Phase 1	Phase 2	$10^{-2}PeSt_m^{-1}$
t_{g3}	Phase 2	Phase 3	$5.2PeSt_m^{-1}\nu^{-1/2}$

Table 3.1: Summary of the different transition times. t_t is the transition time between bending and gravity which is bound by t_t^h, when the current transitions in the first bending thermal phase, and t_t^c, when the current transitions in the third bending thermal phase. t_{b2} (resp. t_{b3}) represents the time to transition from phase 1 to phase 2 (resp. from phase 2 to phase 3) in the bending regime. t_{g2} (resp. t_{g3}) represents the time to transition from phase 1 to phase 2 (resp. from phase 2 to phase 3) in the gravity regime.

3.3.5). In particular, it is bounded by two values corresponding to two end-member cases: the case where the current transitions to the gravity regime while in the first bending phase, i.e. when $\eta_e = \eta_h$ and $t_t^h \sim 6.5h_f^{-1/7}$ and the case where the current transitions to the gravity regime while in the third bending phase, i.e. $\eta_e = \eta_c$ and $t_t^c \sim 6.5\nu^{-2/7}h_f^{-1/7}$. Indeed, when rescaling the time of the simulation by t_t^c, the different simulations, for which the third thermal phase of the bending regime has been reached before the transition to the gravity regime, collapse on the same curve (Figure 3.19, right).

The subsequent evolution in the gravity regime also depends on the combinations (ν,Pe_m) considered. Indeed, in contrast to the bending regime where the effective viscosity is that of a small region at the tip, the effective viscosity is the average flow viscosity in the gravity regime. Therefore, the effective viscosity of the flow can drastically decrease when entering the gravity regime and a flow in the ith thermal phase of the bending regime can transition in the jth thermal phase of the gravity regime with $i \geq j$ which results in 6 possible scenarios. For instance, a current in the second thermal phase of the bending regime can transition into the first or second thermal phase of the gravity current regime. However, the case where a current in the third thermal phase of the bending regime transitions to the first thermal phase of the gravity regime is not possible since the thermal anomaly has already detached from

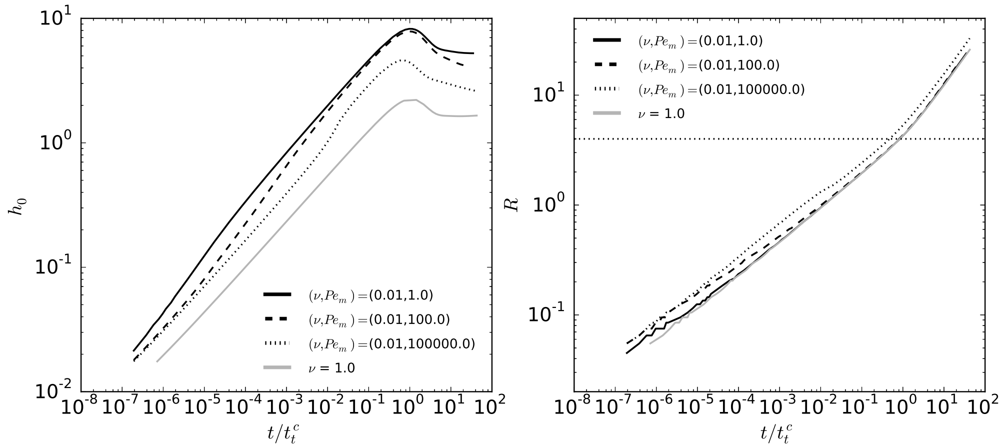

Figure 3.19: Left: Dimensionless thickness at the center h_0 versus time where the time has been rescaled by the time t_t^c the current transitions to the gravity regime while it is in the third bending phase (Table 3.1). The grey line represents the isoviscous case with given viscosity η_h. Right: Same plot but for the dimensionless radius R. Horizontal black dotted-line represents the transition radius between the bending and the gravity regime.

the tip. In the following, we detail the five remaining scenarios in order to build a phase diagram as a function of the combination (ν, Pe_m) considered.

We first consider the case where the current transitions to the gravity regime in the first thermal phase of the bending regime. In that case, the time for the transition is t_t^h; it is less than the time for the second bending thermal phase change t_{b2}; comparing t_t^h and t_{b2} gives $Pe > 65h_f^{-15/7}$ (Figure 3.20, Table 3.1). For $Pe > 65h_f^{-15/7}$, as $t_t^h < t_{g2}$, the current transitions to the first thermal phase of the gravity current regime (B_1G_1 in Figure 3.20).

If the current has already reached the third thermal bending phase, the transition occurs at t_t^c and is necessarily larger than t_{b3}; comparing t_t^c and t_{b3} gives $\nu > 8.3 \cdot 10^{-13} Pe_m^{7/2} h_f^{-1/2}$ (Figure 3.20, Table 3.1). As $t_t^c > t_{g2}$ for $\nu > 8.3 \cdot 10^{-13} Pe_m^{7/2} h_f^{-1/2}$, the current can either transition to the second or third thermal phase of the bending regime. If it transitions to the second phase of the gravity regime, then comparing t_t^c and t_{g3} gives $\nu < 0.3 Pe_m^{14/3} h_f^{2/3}$ (B_3G_2 on Figure 3.20) and if it transitions to the third phase of the gravity current, then $\nu > 0.3 Pe_m^{14/3} h_f^{2/3}$ (B_3G_3 on Figure 3.20).

In the case where the transition occurs when it is in the second bending phase, the time for the transition is not exactly known. However, it is bounded by t_t^h and t_t^c and we can therefore predict some evolution scenarios. Indeed, the transition time is necessarily smaller than t_t^c. Therefore, if $t_t^c < t_{g2}$, i.e.

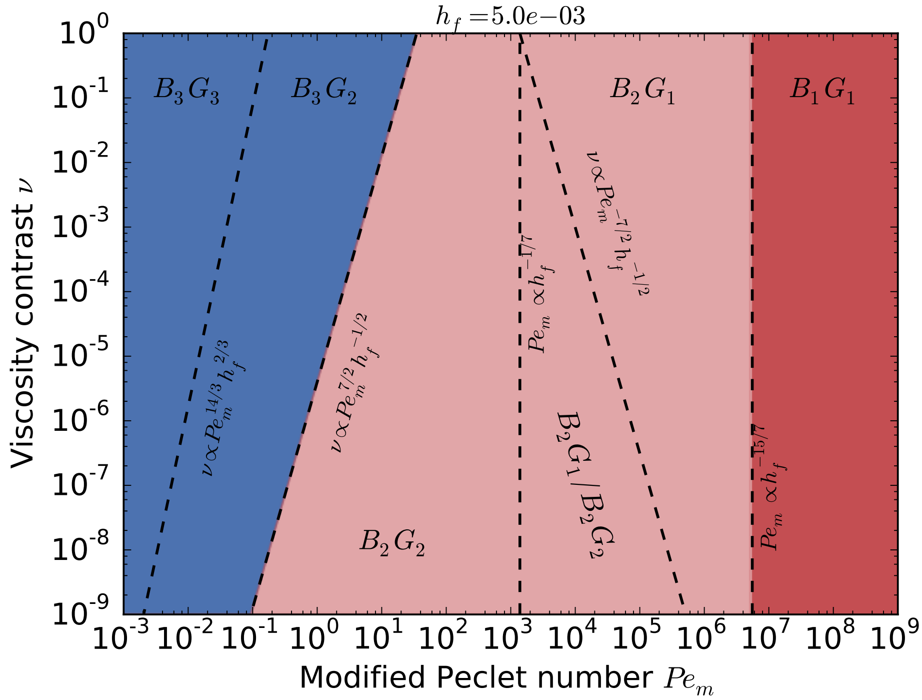

Figure 3.20: Phase diagram for the evolution with bending and gravity for different combinations (ν,Pe_m) and a given value of $h_f = 0.005$. B_iG_j refers to the case where the current transitions from the ith bending thermal phase to the jth gravity thermal phase where i and $j \in \{1, 2, 3\}$.

$\nu > 7.0 \cdot 10^9 Pe_m^{-7/2} h_f^{-1/2}$, the current transitions to the first gravity thermal phase (B_2G_1 on Figure 3.20). Similarly, if $t_t^h > t_{g2}$, i.e. $Pe_m < 650 h_f^{-1/7}$, the current transitions to the second gravity current phase (B_2G_2 on Figure 3.20).

3.6 Summary and conclusion

Isothermal elastic-plated gravity current shows two asymptotic regimes. At early times, the gravity is negligible and the peeling of the front is driven by the bending of the overlying layer. In contrast, at late times, the own flow weight becomes the driving pressure and the current evolves in a gravity current regime. In this study, we have developed a theory for the evolution of an elastic-plated gravity current with a temperature dependent viscosity and studied the response of the flow to its cooling in each regime separately.

In the bending regime, since the flow constantly thickens, the thermal anomaly grows with time but slower than the flow itself and a region of cold fluid rapidly forms at the front. In contrast, in the gravity current regime, since the flow tends to a constant thickness, the temperature profile diffuses to an almost stationary profile and the thermal anomaly reaches a steady-state. The time to reach this steady-state also scales with the dimensionless numbers of the system. Analyses of the heat transport equation in both regimes allowed us to predict the time evolution of this thermal anomaly as a function of the dimensionless number of the system (Pe,ν, St_m).

Numerical resolution of the equations show that the combine of effect of cooling and temperature-dependent viscosity result in important deviations from the isoviscous case. In particular, each regime is split in three different phases: a first phase where the flow behaves as an isoviscous flow with a hot viscosity, a second phase where the flow slows down and drastically thickens and a last phase where the flow returns in an isoviscous flow but with a cold viscosity. These three phases are linked to the coupling between the thermal anomaly and the flow itself and in particular, the second phase of the flow is triggered by the detachment of the thermal anomaly. However, we show that the effective viscosity of the flow is drastically different in the two regimes. While the dynamics is governed by the local thermal state of the front in the bending regime, it is the average thermal structure of the current that controls the flow in the gravity regime.

The final evolution of an elastic-plated gravity current therefore depends on the relative phase change within each regime and on the transition between the bending and the gravity regime itself. We provide a general phase diagram that predicts the different evolution scenarios as a function of the dimensionless parameters. This model for the cooling of an elastic-plated gravity current is further refined and apply to the observation in the next chapter.

Chapter 4

Toward a more realistic model and its application to the spreading of shallow magmatic intrusions

Contents

The previous chapter was a first step toward the understanding of the coupling between the cooling and the spreading of an elastic-plated gravity current. Hereafter, we first investigate the changes triggered by both the heating of the surrounding layer and a more realistic rheology for magmatic intrusions. We then compare the model predictions with the observations presented in chapter 2.

4.1 Theory

We consider the model of elastic-plated gravity current with temperature-dependent viscosity described in Section 3.2 in which we relax the isothermal boundary condition. In the following, we specify only the changes in the theory that come with the new thermal boundary condition and we refer the reader to Section 3.2 for more details about the derivation.

4.1.1 Thermal boundary condition

We now consider the heating of the surrounding medium by the magma. The continuity of the temperature imposes to rewrite the vertical temperature profile as

$$T = \begin{cases} T_b - (T_b - T_s)(1 - \frac{z}{\delta})^2 & 0 \leq z \leq \delta \\ T_b & \delta \leq z \leq h - \delta \\ T_b - (T_b - T_s)(1 - \frac{h-z}{\delta})^2 & h - \delta \leq z \leq h \end{cases} \tag{4.1}$$

where $\delta(r,t)$ is the thermal boundary layer thickness, $T(r,z,t)$ is the temperature of the fluid, $T_b(r,t)$ is the temperature at the center of the profile and $T_s(r,t)$ is the temperature of the surface, i.e. $T(r,z=0,t) = T(r,z=h,t) = T_s(r,t)$. As in Section 3.2, this profile assures the continuity of the temperature and heat flux within the flow. In addition, continuity of the heat flux across the flow boundaries reads

$$k_m \left.\frac{\partial T}{\partial z}\right|_{z=0} = k_r \left.\frac{\partial T_r}{\partial z}\right|_{z=0} \tag{4.2}$$

$$k_m \left.\frac{\partial T}{\partial z}\right|_{z=h} = k_r \left.\frac{\partial T_r}{\partial z}\right|_{z=h} \tag{4.3}$$

where $T_r(r,z)$ is the temperature in the surrounding medium and k_r its thermal conductivity. Assuming a semi infinite layer for the rigid layer below the intrusion, *Carslaw and Jaeger* (1959) show that the temperature T_r in the surrounding rocks can be approximated to a first order by

$$T_r(r,z,t) - T_0 = (T_s - T_0)\,\mathrm{erfc}\left(\frac{-z}{2\sqrt{\kappa_r t}}\right). \tag{4.4}$$

The thickness of the upper layer is equal to the intrusion depth d_c. However, we assume that the depth d_c is large compared to the characteristic length scale for conduction L_c and we use the same approximation to derive T_r above the intrusion

$$T_r(r,z,t) - T_0 = (T_s - T_0)\,\mathrm{erfc}\left(\frac{z-h}{2\sqrt{\kappa_r t}}\right). \tag{4.5}$$

Therefore, the two thermal boundary conditions (4.2) and (4.3) become

$$k_m \left.\frac{\partial T}{\partial z}\right|_{z=0} = k_r \frac{T_s - T_0}{\sqrt{\pi \kappa_r t}} \tag{4.6}$$

$$k_m \left.\frac{\partial T}{\partial z}\right|_{z=h} = -k_r \frac{T_s - T_0}{\sqrt{\pi \kappa_r t}}. \tag{4.7}$$

4.1.2 Dimensionless equations

Except for the conduction term, which now accounts for the dimensionless surface temperature Θ_s, the coupled equations governing the cooling the current are very similar to (3.46) and (3.47) and read

$$\frac{\partial h}{\partial t} - \frac{12}{r}\frac{\partial}{\partial r}\left(rI_1(h)\frac{\partial P}{\partial r}\right) = \mathcal{H}(\frac{\gamma}{2} - r)\frac{32}{\gamma^2}\left(\frac{1}{4} - \frac{r^2}{\gamma^2}\right) \tag{4.8}$$

$$\frac{\partial \xi}{\partial t} + \frac{1}{r}\frac{\partial}{\partial r}\left(r\left(\bar{u}\xi - \Sigma\right)\right) = 2Pe^{-1}St_m\frac{\Theta_b - \Theta_s}{\delta} \tag{4.9}$$

with

$$\bar{\theta} = \frac{1}{3}\left(2\Theta_b + \Theta_s\right) \tag{4.10}$$

$$\bar{u} = \frac{12}{\delta}\frac{\partial P}{\partial r}\left(\delta I_0(\delta) - I_1(\delta)\right) \tag{4.11}$$

$$\Sigma = \frac{12}{\delta}\frac{\partial P}{\partial r}\left(I_0(\delta)\left(G(\delta) - \delta\bar{\theta}\right) + \bar{\theta}I_1(\delta) - I_2(\delta)\right). \tag{4.12}$$

where $G(z)$ denotes a primitive of $\theta(z)$ when $z < \delta$. The rheology, which couples equations (4.8) and (4.9), is contained in the three integrals $I_0(z)$, $I_1(z)$ and $I_2(z)$ and is discussed in the next section. The thermal boundary conditions (4.6) and (4.7) reduce in a dimensionless form to

$$2\frac{\Theta_b - \Theta_s}{\delta} = \Omega Pe^{1/2}\frac{\Theta_s}{\sqrt{\pi t}}. \tag{4.13}$$

where Ω is a new dimensionless number; it is equal to

$$\Omega = \frac{k_r}{k_m}\left(\frac{\kappa_m}{\kappa_r}\right)^{1/2} \tag{4.14}$$

and represents the ratio between heat conduction at the contact with the encasing rocks and heat diffusion within the fluid.

The variable ξ is the sufficient variable to solve for in the heat transport equation (4.9). Indeed,

$$\xi = \frac{\delta}{3}\left(-2\Theta_b - \Theta_s + 3\right) \tag{4.15}$$

where we have used (4.10). In addition, from (4.13), we can rewrite

$$\Theta_s = \frac{2\Theta_b}{\beta\delta + 2}, \tag{4.16}$$

$$\delta = \frac{1}{\Theta_s\beta}\left(2\Theta_b - 2\Theta_s\right), \tag{4.17}$$

$$\Theta_b = \frac{\Theta_s}{2}\left(\beta\delta + 2\right). \tag{4.18}$$

When the thermal boundary layers have just merged, then $\Theta_b = 1$, $\delta = h/2$ and injecting (4.16) into (4.15) gives

$$\xi_t(t) = \frac{\beta(t)h^2(r,t)}{6\beta(t)h(r,t) + 24}. \tag{4.19}$$

Therefore, when $\xi < \xi_t$, the thermal boundary layer are not merged, $\Theta_b = 1$ and injecting (4.17) into (4.15) and solving for Θ_s gives

$$\Theta_s = \frac{3\beta}{4}\xi - \frac{\sqrt{3}}{4}\sqrt{\beta\xi\left(3\beta\xi + 8\right)} + 1. \tag{4.20}$$

In contrast, when $\xi > \xi_t$, the thermal boundary layer have merged, $\delta = h/2$ and injecting (4.18) into (4.15) and solving for Θ_s gives

$$\Theta_s = \frac{-12\xi + 6h}{\left(\beta h + 6\right)h}. \tag{4.21}$$

At the end, we then have

$$\Theta_s(r,t) = \begin{cases} \frac{3\beta}{4}\xi - \frac{\sqrt{3}}{4}\sqrt{\beta\xi\left(3\beta\xi + 8\right)} + 1 & \text{if} \quad \xi \leq \xi_t \\ \frac{-12\xi + 6h(r,t)}{(\beta h(r,t) + 6)h(r,t)} & \text{if} \quad \xi > \xi_t \end{cases} \tag{4.22}$$

and

$$\Theta_b(r) = \begin{cases} 1 & \text{if} \quad \xi \leq \xi_t \\ \frac{\Theta_s}{4}\left(\beta(t)h(r,t) + 4\right) & \text{if} \quad \xi > \xi_t \end{cases} \tag{4.23}$$

$$\delta(r) = \begin{cases} \frac{1}{\Theta_s \beta(t)} \left(-2\Theta_s + 2\right) & \text{if} \qquad \xi \leq \xi_t \\ h(r,t)/2 & \text{if} \qquad \xi > \xi_t \end{cases} \tag{4.24}$$

with

$$\xi_t(t) = \frac{\beta(t) h^2(r,t)}{6\beta(t) h(r,t) + 24} \tag{4.25}$$

$$\beta(t) = \Omega Pe^{1/2} \frac{1}{\sqrt{\pi t}} \tag{4.26}$$

4.1.3 Rheology

The model derived in Section 4.1.2 does not yet assume a specific relation between viscosity and temperature and the choice of the rheology $\eta(T)$, which is contained in the integrals $I_0(z)$, $I_1(z)$ and $I_2(z)$, remains to be defined. In Section 3.2, we assume a viscosity inversely dependent on the temperature which reads in a dimensional form

$$\eta(T) = \frac{\eta_h \eta_c (T_i - T_0)}{\eta_h (T_i - T_0) + (\eta_c - \eta_h)(T - T_0)}. \tag{4.27}$$

where η_h and η_c are the viscosities of the hottest and coldest fluid at the temperature T_i and T_0 respectively (*Bercovici*, 1994). While this model possesses some nice simplification properties, it restricts the change in viscosity to a very narrow range of temperature close to $T = T_0$, i.e. $\theta = 0$ (Figure 4.1). In contrast, the Arrhenius model ($\eta \sim \exp(-k/T)$), which is a more realistic model to relate temperature and viscosity of lavas (*Blatt et al.*, 2006), describes a viscosity that increases over a much larger range of temperature (Figure 4.1). To get some insights into the effect of a more realistic temperature-dependent viscosity, we thus also use a first-order approximation of the Arrhenius model as a second rheology $\eta_2(T)$ (*Diniega et al.*, 2013)

$$\eta_2(T) = \eta_h \exp\left(-\log\left(\frac{\eta_h}{\eta_c}\right)\left(1 - \frac{T - T_0}{T_i - T_0}\right)\right) \tag{4.28}$$

In a dimensionless form, they read

$$\eta_1(\theta)/\eta_h = \frac{1}{\nu + (1-\nu)\theta} \tag{4.29}$$

$$\eta_2(\theta)/\eta_h = \exp\left(-\log(\nu)\left(1-\theta\right)\right) \tag{4.30}$$

where ν is the viscosity contrast described in Section 3.2 and represents the ratio between the hot viscosity η_h and the cold viscosity η_c. The expression of $I_0(\delta)$, $I_1(\delta)$, $I_1(h)$ and $I_2(\delta)$, necessary to close the model, are given in Appendix A for both rheologies.

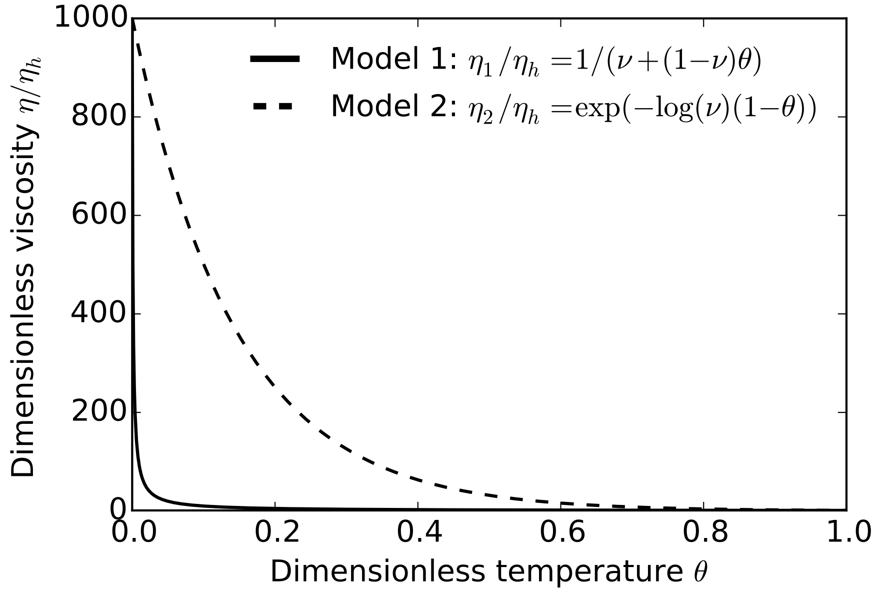

Figure 4.1: Dimensionless viscosity versus dimensionless temperature for both rheology η_1 (4.29) and η_2 (4.30) and $\nu = 0.001$.

4.1.4 Comparison with the isothermal model

We showed that relaxing the isothermal boundary condition introduces a new dimensionless number Ω which controls how much heat can be transferred to the surrounding rocks. In the limit $\Omega \to \infty$, the model should thus reduce to the model described in Section 3.2. Indeed, when $\Omega \to \infty$, the coefficient $\beta \to \infty$ and then $\xi_t \to h/6$ (Section 3.2). When $\xi < \xi_t$, injecting the corresponding expression of Θ_s (4.22) in the corresponding expression of δ (4.24) gives

$$\delta = \frac{3\beta\xi + \sqrt{3}\sqrt{\beta\xi(3\beta\xi+8)} + 8}{2\beta} \tag{4.31}$$

which tends to 3ξ when $\beta \to \infty$. When $\xi > \xi_t$, injecting the corresponding expression of Θ_s (4.22) in the corresponding expression of Θ_b (4.23) gives

$$\Theta_b = \frac{3(\beta h + 4)(h - 2\xi)}{2h(\beta h + 6)} \tag{4.32}$$

which tends to $3/2 - 3\xi/h$ when $\beta \to \infty$ (Section 3.2). Finally, taking the limit of Θ_s for both $\xi > \xi_t$ and $\xi < \xi_t$ show that Θ_s indeed tends to zero when $\Omega \to \infty$.

For magmatic intrusions, the thermal parameters of the magma and the encasing rocks are close and the dimensionless number Ω would be close to

1. In the following, we study the effect of relaxing the isothermal boundary condition on the dynamics by comparing $\Omega = 10^5$ and $\Omega = 1$ in both regimes separately. We also investigate the effect of a more realistic rheology on the flow dynamics.

4.2 Evolution in the bending regime

We follow the same approach as in the previous Chapter and first concentrate on the case in which only bending contributes to the pressure. The governing equations are thus (4.8) and (4.9) where $P = \nabla_r^4 h$. For isothermal boundary condition, we show that the dynamics in the bending regime depends on the average viscosity of a small region at the front of the current and can be divided into three phases. Hereafter, we first describe how the thermal boundary condition influences the timing for the phase transition by looking at two values for the dimensionless number Ω, i.e. $\Omega = 1$ and $\Omega = 10^5$ and $\eta(\theta) = \eta_1(\theta)$. We thus investigate the effect of changing the rheology.

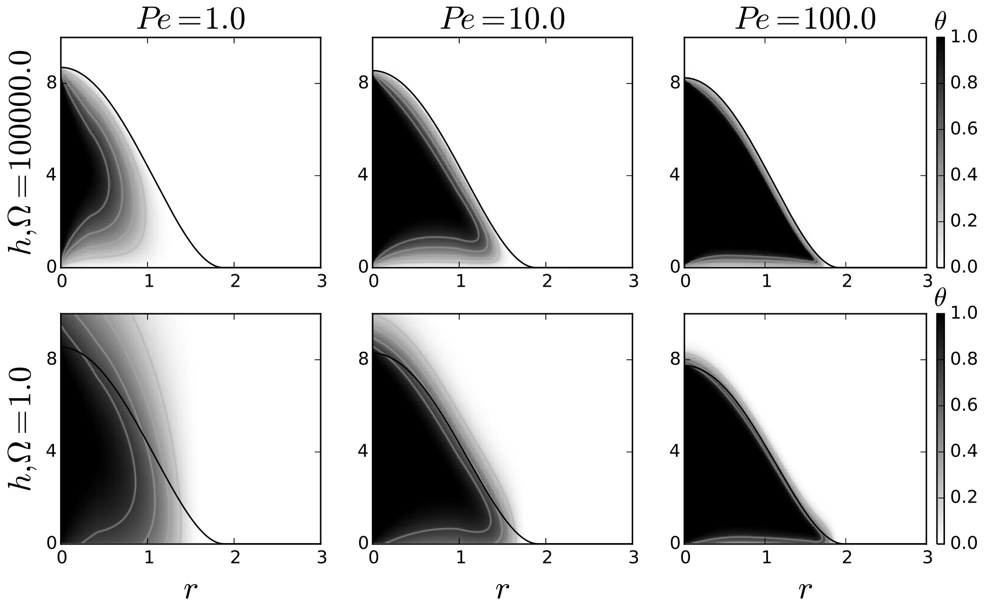

Figure 4.2: Snapshots of the flow thermal structure $\theta(r, z, t)$ for different sets (Pe,Ω) with $Pe = 1.0$,10.0 ,100.0 and $\Omega = 10^5$ and 1.0 at $t = 10$ for $\nu = 0.001$. The thermal structure above the intrusion is given by (4.5) and reads in a dimensionless form $\Theta_r(r, z, t) = \Theta_s(r, t)\,\mathrm{erfc}\left(Pe^{1/2}\frac{\kappa_m}{\kappa_r}\frac{(z-h)}{2\sqrt{t}}\right)$ where the ratio κ_m/κ_r is set to 1. The thermal structure below the intrusions is similar and not shown for clarity.

4.2.1 Relaxing the thermal boundary condition, effect of Ω

The heating of the surrounding medium limits heat loss in the flow central region and the thermal anomaly extends further into the flow (Figure 4.2). For instance, for $\nu = 0.001$ and $Pe = 1.0$, while the thermal anomaly extends over 50% of the current for $\Omega = 10^5$ at $t = 10$, it extends over more than 75% of the flow for $\Omega = 1$ (Figure 4.2). Nevertheless, the tip of the current is still rapidly cooling and the thermal anomaly also detaches from the front when relaxing the thermal boundary condition.

Hence, the dynamics for $\Omega = 1$ also passes through three different phases. The current first behaves as an isoviscous flow with hot viscosity, it then slows down and thickens to finally behave again as an isoviscous flow but with cold viscosity (Figure 4.3). As the current tip remains hot for a longer period of time, the transition to the second and third bending regime are however delayed relatively to the case $\Omega = 10^5$ (Figure 4.3). For instance, for $\nu = 10^{-3}$ and $Pe = 1.0$, while the transition to the second bending phase already begins at $t \sim 10^{-6}$ for $\Omega = 10^5$, it occurs only after $t \sim 10^{-5}$ for $\Omega = 1.0$ (Figure 4.3).

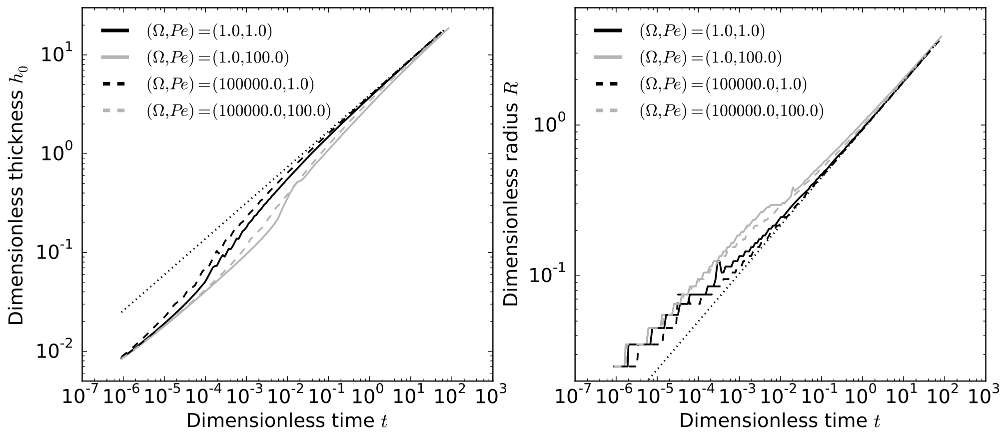

Figure 4.3: Left: Dimensionless thickness at the center h_0 versus dimensionless time t for different sets (Ω, Pe) indicated on the plot. Dotted-line: scaling law $h_0 = 0.7 h_f^{-1/11} \nu^{-2/11} t^{8/22}$ for $\nu = 0.001$. Right: Dimensionless radius R versus dimensionless time t for the same sets (Ω, Pe). Dotted-line: scaling law $R = 2.2 h_f^{1/22} \nu^{1/11} t^{7/22}$ for $\nu = 0.001$. In all simulations, $\nu = 0.001$ and $\eta(\theta) = \eta_1$.

In addition, the second phase of thickening shows two different stages for $\Omega = 1.0$ and $Pe = 100.0$, a first stage where the thickness drastically increases and a second stage where it continues increasing but much slower (Figure 4.3).

This transition, enhanced by the new thermal boundary condition, reflects the detachment of the thermal anomaly in the second bending phase and is discussed in Appendix C.2.

4.2.2 Considering a more realistic rheology, effect of $\eta(\theta)$

The first order Arrhenius rheology $\eta_2(\theta)$ widens the range of temperature over which significant viscosity variation occurs, i.e. $\sim$ 80% of the temperature range against $\sim$ 10% for $\eta_1(\theta)$ (Figure 4.1).

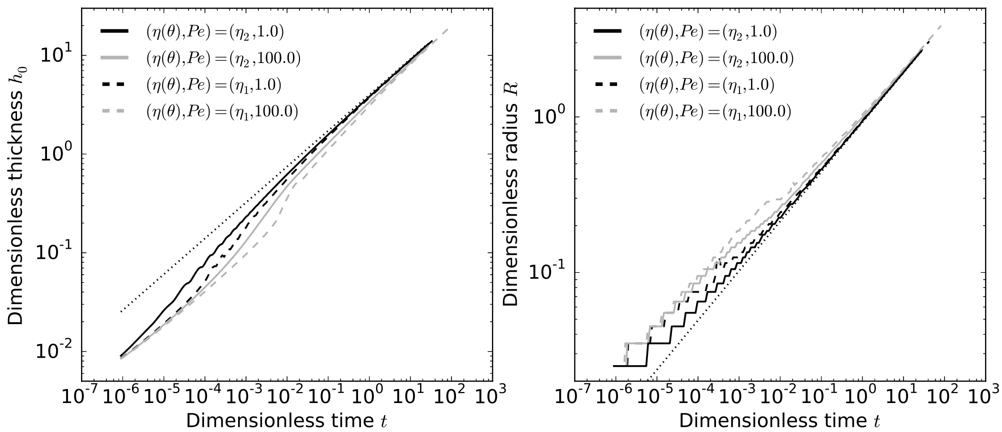

Figure 4.4: Left: Dimensionless thickness at the center h_0 versus dimensionless time t for different sets (η, Pe) indicated on the plot. Dotted-line: scaling law $h_0 = 0.7 h_f^{-1/11} \nu^{-2/11} t^{8/22}$ for $\nu = 0.001$. Right: Dimensionless radius R versus dimensionless time t for the same sets (η, Pe). Dotted-line: scaling law $R = 2.2 h_f^{1/22} \nu^{1/11} t^{7/22}$ for $\nu = 0.001$. In all simulations, $\nu = 0.001$ and $\Omega = 1.0$.

Therefore, the effective flow viscosity starts to increase sooner and the transition to the second bending phase occurs sooner than for the rheology previously considered $\eta_1(\theta)$ (Figure 4.4). For instance, for $\nu = 10^{-3}$ and $Pe = 1.0$, while the second phase of the flow starts around $t \sim 10^{-5}$ for the rheology $\eta_1(\theta)$, it starts around $t \sim 10^{-6}$ for the rheology $\eta_2(\theta)$ (Figure 4.4). In particular, the change in rheology almost compensates for the delay caused by the heating of the surrounding medium. For instance, the transition time for the second bending phase for the current characterized by $\eta = \eta_1(\theta)$ and $\Omega = 10^5$ is almost the same than for the current characterized by $\eta = \eta_2(\theta)$ and $\Omega = 1$ (Figure 4.4 and 4.5).

4.2.3 Characterization of the thermal anomaly

As in Chapter 3, we quantify the size of the thermal anomaly through a critical thermal radius $R_c(t)$ where the temperature at the center of the flow Θ_b is 1% of the injection temperature, i.e. $\Theta_b(r=0) - \Theta_b(r=R_c) = 0.99$. As expected, the thermal anomaly is larger when relaxing the thermal boundary condition and changing the rheology $\eta(\theta)$ has almost no effect on its evolution (Figure 4.5). In addition, the extent of the cold fluid region $R(t) - R_c(t)$ is growing slightly slower with time when considering $\Omega = 1$ in comparison to the isothermal boundary case $\Omega = 10^5$ (Figure 4.5). In the following, we characterize the thermal anomaly evolution in the more realistic case where $\Omega = 1$ and $\eta(\theta) = \eta_2(\theta)$.

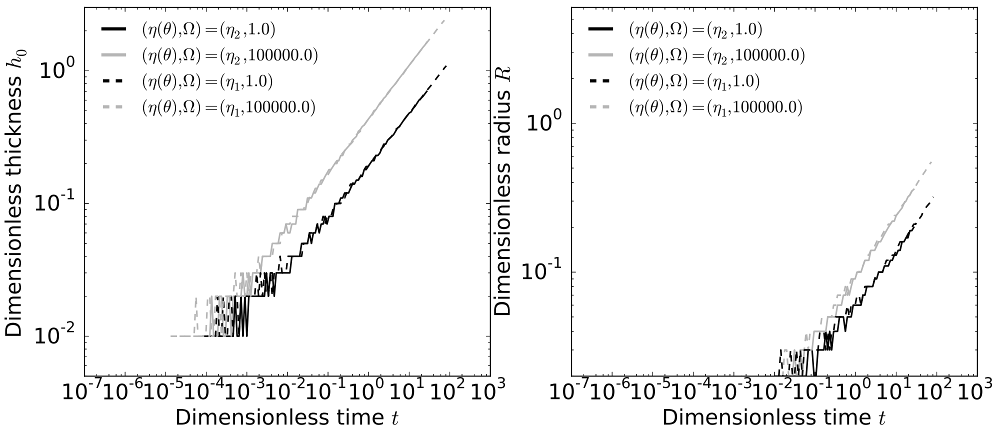

Figure 4.5: Left: Extent of the cold fluid region $R(t) - R_c(t)$ versus dimensionless time for different combinations (η,Ω) indicated on the plot, $\nu = 0.01$ and $Pe = 1.0$. Same plot but for $Pe = 100.0$.

The size of the thermal anomaly $R_c(t)$ is given by the radius where advection of heat is equal to heat loss

$$\frac{d}{dt}\left(\theta(r=R_c,t)\right) \approx Pe^{-1}\frac{\partial^2}{\partial z^2}\left(\theta(r=R_c,t)\right) \tag{4.33}$$

which, by integration over the thickness of the flow h, becomes

$$\begin{aligned}
\frac{d}{dt}\left(\int_0^h \theta dz\right) - \Theta_s\frac{dh}{dt} &\approx Pe^{-1}\frac{\Theta_b - \Theta_s}{h} \\
\overline{\theta}\frac{dh}{dt} + h\frac{d\overline{\theta}}{dt} - \Theta_s\frac{dh}{dt} &\approx Pe^{-1}\frac{\Theta_b - \Theta_s}{h} \\
\frac{2}{3}\left(\Theta_b - \Theta_s\right)\frac{dh}{dt} + h\frac{d\overline{\theta}}{dt} &\approx Pe^{-1}\frac{\Theta_b - \Theta_s}{h}
\end{aligned} \tag{4.34}$$

where $\overline{\theta}$ is equal to $(\int_0^h \theta dz)/h$ here. Using the thickness profile (3.50), (4.34) becomes

$$\alpha^2\left(1+\frac{R_c}{R}\right)^2\left(\frac{2}{3}\left(\Theta_b-\Theta_s\right)\frac{dh_0}{dt}+h_0\frac{d\overline{\theta}}{dt}\right)+\frac{8h_0R_c^2\left(\Theta_b-\Theta_s\right)}{3R^3}\frac{dR}{dt}\alpha\left(1+\frac{R_c}{R}\right)\approx\frac{Pe^{-1}(\Theta_b-\Theta_s)}{\alpha^2\left(1+\frac{R_c}{R}\right)^2h_0} \tag{4.35}$$

where $\alpha(t)$ is the normalized region beyond $r = R_c(t)$, i.e. $\alpha(t) = \left(R(t)-R_c(t)\right)/R(t)$. In the limit $\alpha << 1$, i.e. $R_c/R \sim 1$, and neglecting the higher order terms in (4.35) ($\propto \alpha^2$), we obtain the same scaling law for the size of the normalized cold front region α than the one found in Section 3.3.4. However, it clearly not matches the prediction when $\Omega = 1.0$ (Figure 4.6) and the new thermal anomaly evolution must be linked to a change in the heat advection rate, i.e. the left hand side term in the balance (4.35). Neglecting the advection term to keep only the inflation term instead in (4.35) leads to

$$\alpha^2\left(1+\frac{R_c}{R}\right)^2\frac{dh_0}{dt}\approx\frac{Pe^{-1}}{\alpha^2\left(1+\frac{R_c}{R}\right)^2h_0} \tag{4.36}$$

which, in the limit $\alpha << 1$, becomes

$$\alpha^4\frac{\partial h_0}{\partial t}\approx\frac{Pe^{-1}}{h_0\frac{\partial h_0}{\partial t}}. \tag{4.37}$$

Substituting $h_0(t)$ by its respective scaling law (3.54), the relative size of the normalized cold front region α reads

$$\alpha(t)\propto h_f^{1/22}\nu^{1/11}Pe^{-1/4}t^{7/44} \tag{4.38}$$

which is equivalent to

$$R(t)-R_c(t)=0.8h_f^{1/11}\nu^{2/11}Pe^{-1/4}t^{17/44} \tag{4.39}$$

where the numerical prefactor, which depends on the definition of the thermal anomaly, has been chosen to fit the simulations.

The new predicted scaling law for the evolution of the extent of the cold fluid region (4.39) shows a much better fit with the simulations (Figure 4.6 b). Therefore, the evolution of the thermal anomaly is governed by the inflation rate at the intrusion tip when relaxing the thermal boundary condition. The cold fluid region grows slightly slower, from $t^{9/22}$ to $t^{17/44}$ ($9/22 \sim 0.40$, $17/44 \sim 0.38$) and the dependence in the Peclet number Pe is weaker, i.e. from a power 1/3 to 1/4. Indeed, for small Pe, the vertical diffusion is efficient on the emplacement time scale and rapidly heats up the surrounding

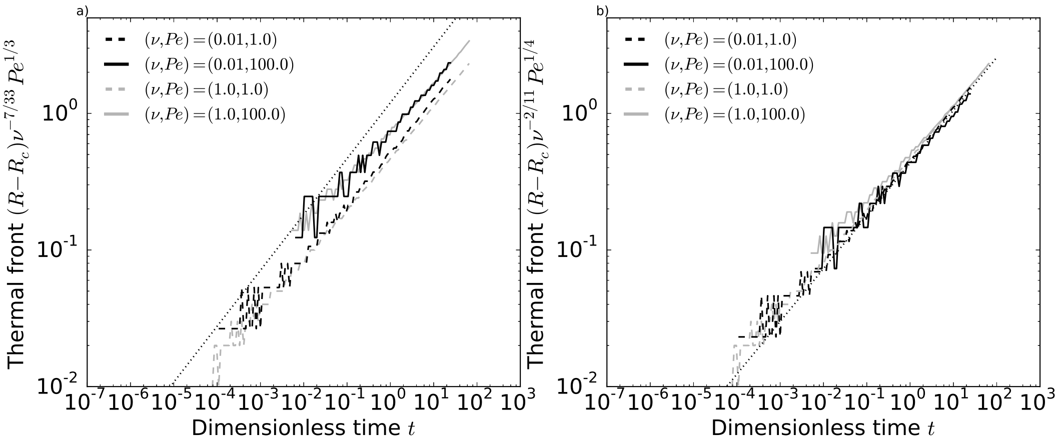

Figure 4.6: a) Extent of the cold fluid region $R(t) - R_c(t)$ rescaled by $Pe^{-1/3}\nu^{7/33}$ versus time for different combinations (ν,Pe) indicated on the plot. Dotted-line: scaling law $(R(t) - R_c(t))Pe^{1/3}\nu^{-7/33} = 2.1h_f^{7/66}t^{9/22}$ b) Same plot but where we rescale the extent of the cold fluid region by $Pe^{-1/4}\nu^{2/11}$. Dotted-line: scaling law $(R(t) - R_c(t))Pe^{1/4}\nu^{-2/11} = 0.7h_f^{1/11}t^{17/44}$. In all simulations, $\Omega = 1.0$ and $\eta(\theta) = \eta_2$.

medium. The heat loss in the interior are smaller and the thermal anomaly larger in comparison to the case where $\Omega = 10^5$. In contrast, for large values of Pe, the advection dominates and the saving of heat due to the heating of the surrounding medium is less important decreasing the overall difference between small and large values of Pe.

As we show in section 4.2.2, the time t_{b2} for the current to enter the second bending phase does not change much as the delay induced by the heating of the surrounding medium is offset by the change in rheology. Accordingly, we use the time t_{b2} (3.63) defined in section 3.3.5 to characterize the first bending transition (Figure 4.7 a). In contrast, the time t_{b3} for the current to enter the third phase of the flow, which is defined as the time for the effective viscosity to reach 90% of its maximum value η_c and depends on the evolution of the cold fluid region (Section 3.3.5), is now larger and equal to

$$t_{b3} = 0.4h_f^{-4/17}\nu^{-8/17}Pe^{11/17}St_m^{-11/17} \tag{4.40}$$

4.2.4 Size of the thermal aureole

The size of the thermal aureole, the heated region surrounding the current, scales as $(\kappa_r\tau)^{1/2}$, i.e. $Pe^{-1/2}$ and hence is much larger for small values of Pe.

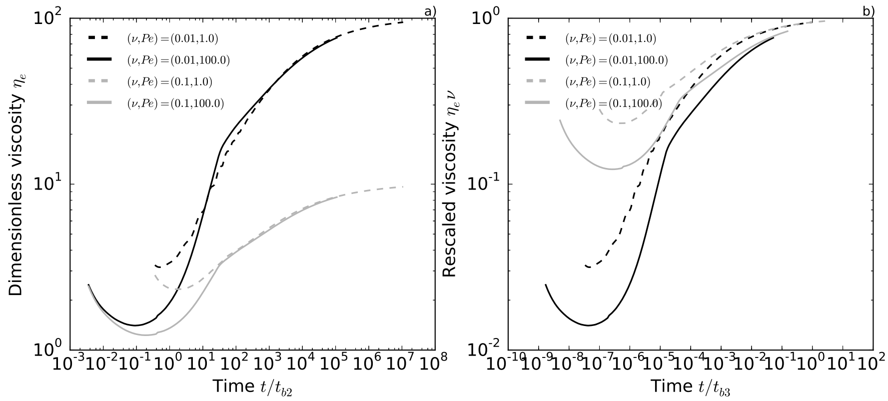

Figure 4.7: a) Dimensionless effective viscosity versus time where the time has been rescaled by the time for the flow to enter the second phase t_{b2}. b) Same as left but where we rescale the viscosity by ν and the time by t_{b3}. In all simulations, $\Omega = 1.0$ and $\eta(\theta) = \eta_2$.

Indeed, for large values of Pe, advection dominates on the emplacement time scale and the thermal aureole is restricted to a small zone around the current (Figure 4.2). For instance, the thickness of the thermal aureole at the center for $Pe = 1.0$ is almost equal to the current thickness h_0 whereas it is only a few percent of h_0 for $Pe = 100.0$ (Figure 4.2).

4.3 Evolution in the gravity regime

As in chapter 3, we now consider the late time behavior in which only the weight of the fluid contributes to the dynamic pressure P. The governing equations are (4.8) and (4.9) where $P = h$. We follow the same framework as in the previous section.

4.3.1 Relaxing the thermal boundary condition, effect of Ω

As in the bending regime, for a small value of Ω, the heating of the surrounding medium limits heat loss in the central region of the current and the thermal anomaly extends further into the flow. For instance, for $Pe = 1$ and $\nu = 0.01$ at $t = 200$, while $R_c \sim 1$ for $\Omega = 10^5$, R_c is larger than 5 for $\Omega = 1$ (Figure 4.8). In addition, after it detaches from the current tip, the thermal anomaly does not reach a steady-state profile but keeps growing with time instead (Figure 4.9). Indeed, in contrast to the isothermal boundary case, the constant

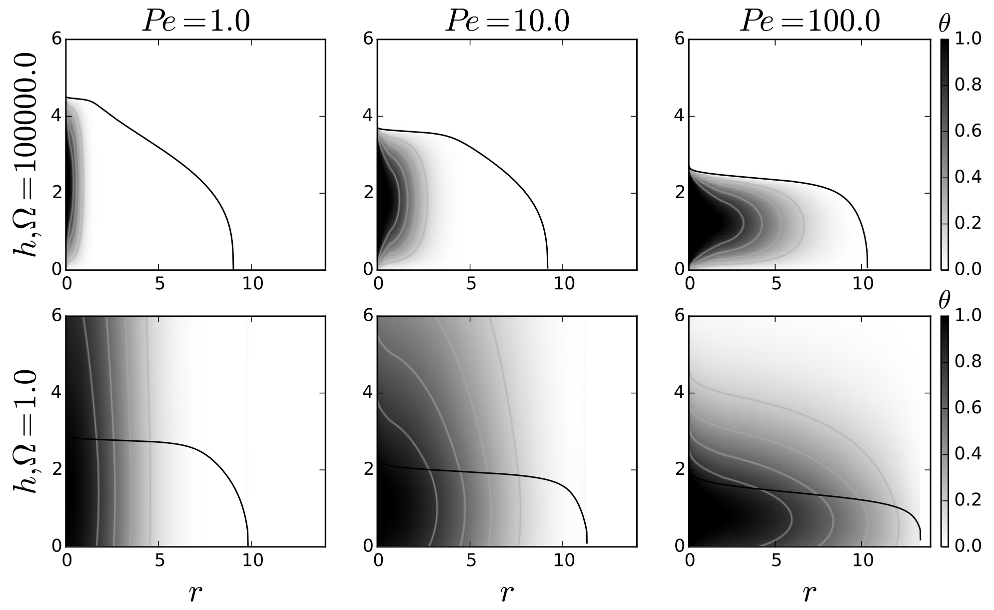

Figure 4.8: Snapshots of the flow thermal structure $\theta(r,z,t)$ for different sets (Pe,Ω) with Pe = 1.0 ,10.0 ,100.0 and $\Omega = 10^5$ and 1.0 at $t = 200$ for $\nu = 0.01$. The thermal structure above the current is given by (4.5) and reads in a dimensionless form $\Theta_r(r,z,t) = \Theta_s(r,t)\,\mathrm{erfc}\left(Pe^{1/2}\frac{\kappa_m}{\kappa_r}\frac{(z-h)}{2\sqrt{t}}\right)$ where the ratio κ_m/κ_r is set to 1.

increase of the surface temperature continuously decreases the heat loss in the central region of the current which allows the expansion of the thermal anomaly.

For small values of Pe, the efficient heat conduction results in an almost vertical isothermal current at $t = 200$ (Figure 4.8). In contrast, for large values of Pe, the vertical diffusion of heat is less efficient, the thermal aureole is restricted to a small region around the intrusion, the thermal anomaly is larger and the temperature gradient within the flow are stronger (Figure 4.8).

While three phases also characterized the dynamics when $\Omega = 1.0$, their extent and duration are modified by the new thermal boundary condition (Figure 4.10). In particular, the current remains hot for a longer period of time and the second phase is delayed in comparison to the case where $\Omega = 10^5$. For instance, for $\nu = 0.01$ and $Pe = 1.0$, while this transition occurs around $t = 0.1$ for $\Omega = 10^5$, it happens only after $t = 1$ for $\Omega = 1$ (Figure 4.10). As the thermal anomaly does not reach a steady state for $\Omega = 1$, the cooling of the current in the second gravity phase is also slower than for $\Omega = 10^5$ and the current reaches the third phase also much later for $\Omega = 1$ (Figure 4.10).

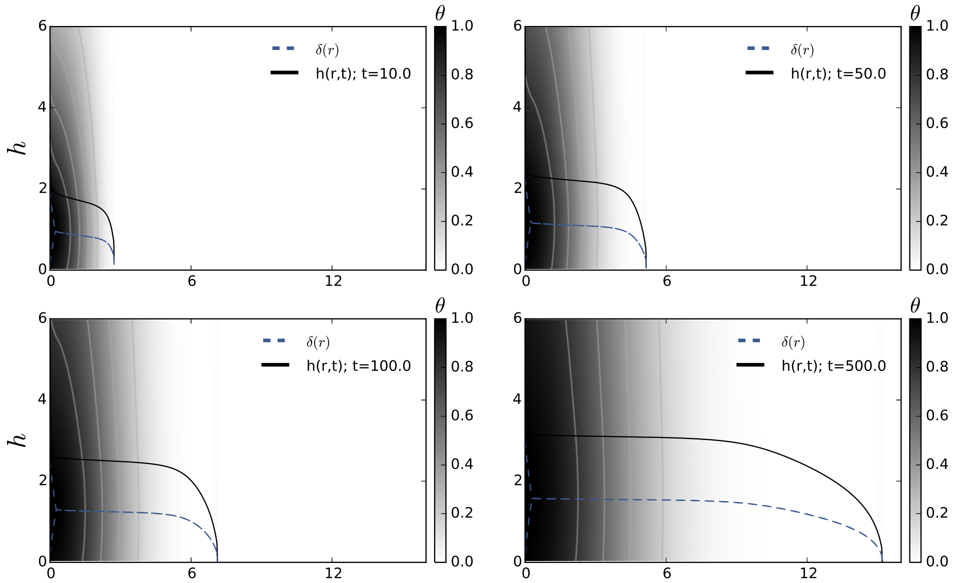

Figure 4.9: Snapshots of the flow thermal structure $\theta(r,z,t)$ at different times indicated on the plot. Dashed lines represent the thermal boundary layers. Solid grey lines are isotherms for $\theta = 0.2$, 0.4, 0.6 and 0.8. Here, $\nu = 0.01$, $Pe = 1.0$ and $St_m = 1$. The thermal structure above the intrusion is given by (4.5) and reads in a dimensionless form $\Theta_r(r,z,t) = \Theta_s(r,t)\,\text{erfc}\left(Pe^{1/2}\frac{\kappa_m}{\kappa_r}\frac{(z-h)}{2\sqrt{t}}\right)$ where the ratio κ_m/κ_r is set to 1.

In the next section, we consider the effect of the first order Arhenius rheology on the dynamics for $\Omega = 1.0$.

4.3.2 Considering a more realistic rheology, effect of $\eta(\theta)$

As in the bending regime, the chosen rheology $\eta(\theta)$ also affects the timing for the phase transition, and, in particular, these transitions occur sooner for the first order Arrhenius rheology $\eta_2(\theta)$ than for $\eta = \eta_1(\theta)$. In particular, the delay induced in the phase transitions by the heating of the surrounding medium is almost offset by the first order Arrhenius rheology. For instance, the transition to the second gravity phase occurs around the same time for a current characterized by $\eta(\theta) = \eta_1$ and $\Omega = 10^5$ than for a current characterized by $\eta(\theta) = \eta_2$ and $\Omega = 1.0$ (Figure 4.10 and 4.11).

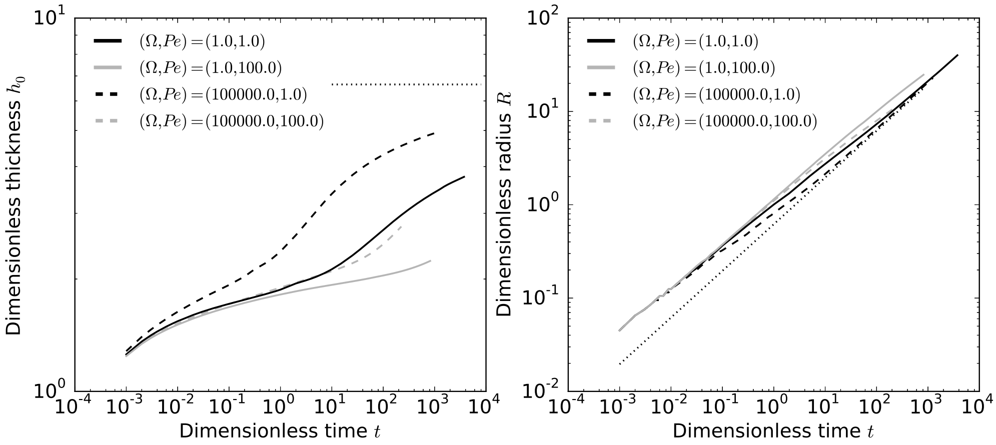

Figure 4.10: Left: Dimensionless thickness at the center h_0 versus dimensionless time t for different sets (Ω, Pe) indicated on the plot. Dotted-line: scaling law $h_0 = 0.7 h_f^{-1/11} \nu^{-2/11} t^{8/22}$ for $\nu = 0.01$. Right: Dimensionless radius R versus dimensionless time t for the same sets (Ω, Pe). Dotted-line: scaling law $R = 2.2 h_f^{1/22} \nu^{1/11} t^{7/22}$ for $\nu = 0.01$. In all simulations, $\nu = 0.01$ and $\eta(\theta) = \eta_1$.

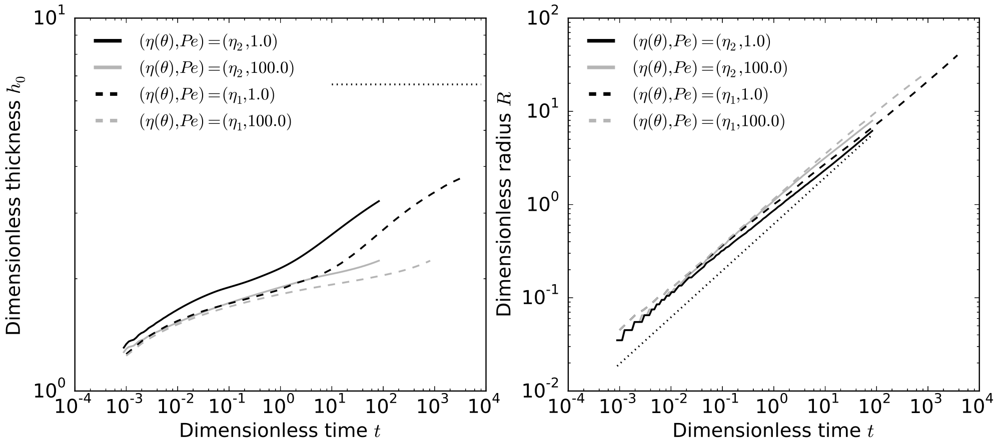

Figure 4.11: Left: Dimensionless thickness at the center h_0 versus dimensionless time t for different sets (η, Pe) indicated on the plot. Dotted-line: scaling law $h_0 = 0.7 h_f^{-1/11} \nu^{-2/11} t^{8/22}$ for $\nu = 0.01$. Right: Dimensionless radius R versus dimensionless time t for the same sets (η, Pe). Dotted-line: scaling law $R = 2.2 h_f^{1/22} \nu^{1/11} t^{7/22}$ for $\nu = 0.01$. In all simulations, $\nu = 0.01$ and $\Omega = 1$.

4.3.3 Characterization of the thermal anomaly

As in the bending regime, the thermal anomaly is first attached to the tip of the current, i.e. $R_c(t)/R(t) = 1$. After a time that depends on Pe as well as ν, the thermal anomaly detaches from the tip and follows its own evolution. However, in contrast to the isoviscous case, the thermal anomaly does not reach a steady state and R_c/R does not evolve as $t^{-1/2}$ anymore (Figure 4.12 a). We develop a simple thermal budget that accounts for the heating of the surrounding medium to quantify the new evolution of the thermal anomaly.

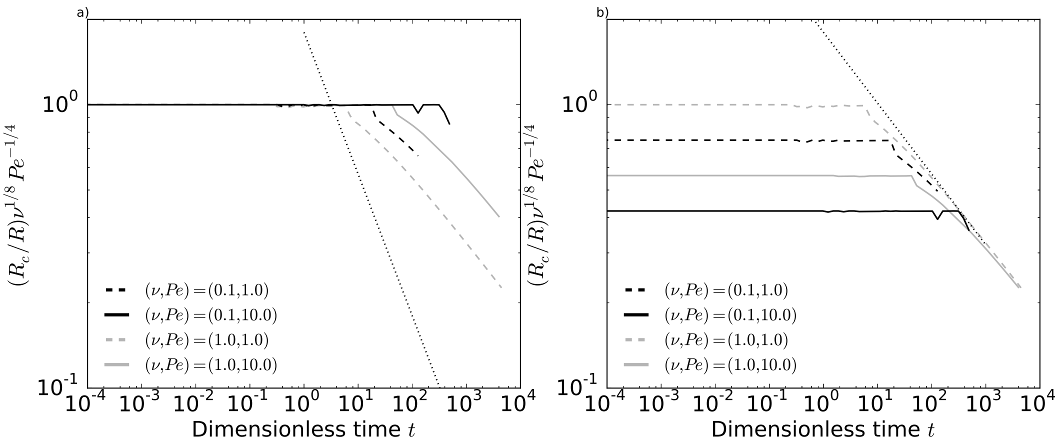

Figure 4.12: a) Normalized thermal anomaly radius $R_c(t)/R(t)$ versus time for different combinations (ν,Pe) indicated on the plot. Dotted-line: $R_c(t)/R(t) \sim t^{1/2}$ b) Same plot but where we rescale the normalized thermal anomaly by $Pe^{1/4}\nu^{-1/8}$. Dotted-line: scaling law $(R_c(t)/R(t))Pe^{-1/4}\nu^{1/8} = 1.8t^{-1/4}$. In all simulations, $\Omega = 1.0$ and $\eta(\theta) = \eta_1$.

When the thermal anomaly has detached from the intrusion front, a balance between heat advection and diffusion in the surrounding medium in a dimensional form reads

$$\rho C_p U_0 \frac{\Delta T}{R_c} \approx k_m \frac{\Delta T}{h_0^2} \tag{4.41}$$

where ΔT is the mean temperature contrast between the fluid and the surrounding and U_0 is taken as a redistribution of the injection rate at $r = R_c$, i.e. $U_0 = Q_0/(2\pi R_c h_0)$. In addition, the continuity of the heat flux at the boundary (4.6) imposes

$$k_m \frac{\Delta T}{h_0} \approx k_s \frac{\Delta T}{\sqrt{\pi \kappa_r t}}. \tag{4.42}$$

Injecting (4.42) and the expression for the velocity into (4.41) gives

$$R_c \approx \left(\frac{Q_0 \kappa_r^{1/2}}{\kappa_m k_s} \right)^{1/2} t^{1/4}. \tag{4.43}$$

By non-dimensionalizing (4.43), we obtain the evolution of the thermal anomaly when it has detached from the tip $R_c(t) \sim \Omega^{-2} Pe^{1/4} t^{1/4}$ and hence

$$\frac{R_c(t)}{R(t)} = 1.8 \Omega^{-2} Pe^{1/4} \nu^{-1/8} t^{-1/4} \tag{4.44}$$

where we have used the scaling law for $R(t)$ given by (3.66) and the numerical prefactor, which depends on the definition of the thermal anomaly, has been chosen to fit the simulations. The scaling law, which is only valid for $\Omega = O(1)$, indeed closely fits the simulations. In particular, both the dependence with the Peclet number Pe and the viscosity contrast vanishes when rescaling by $Pe^{1/4}\nu^{-1/8}$ (Figure 4.12 b).

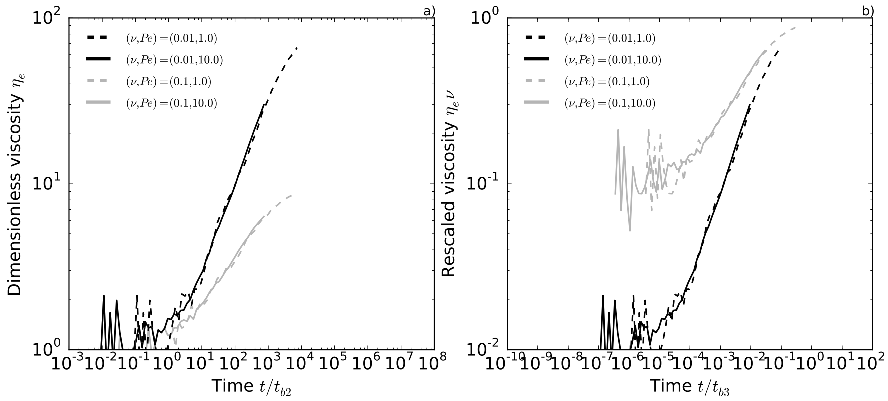

Figure 4.13: a) Dimensionless effective viscosity versus time where the time has been rescaled by the time for the flow to enter the second phase t_{g2}. b) Same as left but where we rescale the viscosity by ν and the time by t_{g3}. In all simulations, $\Omega = 1.0$ and $\eta(\theta) = \eta_1$.

The time t_{g2} for the current to enter the second gravity phase does not change much as the delay induced by the heating of the surrounding medium is offset by the change in rheology. Accordingly, we use the time t_{g2} (3.73) to characterize the first gravity transition (Figure 4.13 a). In contrast, the time t_{g3} for the current to enter the third phase of the flow, which is defined as the time for the effective viscosity to reach 90% of its maximum value η_c and depends on the evolution of the thermal anomaly (Section 3.4.5), is now larger and equal to

$$t_{g3} = 80\Omega^{-8}\nu^{-1/2}PeSt_m^{-1} \tag{4.45}$$

Name	From	To	Expression
t_t	Bending	Gravity	$6.5(\eta_e/\eta_h)^{2/7}h_f^{-1/7}$
t_t^h	Bending	Gravity	$6.5h_f^{-1/7}$
t_t^c	Bending	Gravity	$6.5\nu^{-2/7}h_f^{-1/7}$
Bending regime			
t_{b2}	Phase 1	Phase 2	$0.1PeSt_m^{-1}h_f^2$
t_{b3}	Phase 2	Phase 3	$0.4h_f^{-4/17}St_m^{-11/17}Pe^{11/17}\nu^{-8/17}$
Gravity regime			
t_{g2}	Phase 1	Phase 2	$10^{-2}PeSt_m^{-1}$
t_{g3}	Phase 2	Phase 3	$80PeSt_m^{-1}\nu^{-1/2}$

Table 4.1: Summary of the different transition times. t_t is the transition time between bending and gravity which is bound by t_t^h, when the current transitions in the first bending thermal phase, and t_t^c, when the current transitions in the third bending thermal phase. t_{b2} (resp. t_{b3}) represents the time to transition from phase 1 to phase 2 (resp. from phase 2 to phase 3) in the bending regime. t_{g2} (resp. t_{g3}) represents the time to transition from phase 1 to phase 2 (resp. from phase 2 to phase 3) in the gravity regime.

4.4 Evolution with bending and gravity in the more realistic model

In the previous chapter, we showed that the final evolution of an elastic-plated gravity current depends on the relative phase changes within each regime and the transition between the bending and the gravity regime itself. The Arrhenius rheology tends to offset the delay caused by the heating of the surrounding medium and overall, the phase diagram presented in section (3.5) shows only minor modifications (Figure 4.14). Except for the transitions from the third bending phase to the second and third gravity phases, which are shifted to the left, the phase diagram is indeed not modified (Appendix B). Therefore, in the framework of our more realistic model, the current is only more likely to transition to the gravity regime before reaching the third bending phase. In the following, we look at the observations discussed in chapter 2 in the light of our new model.

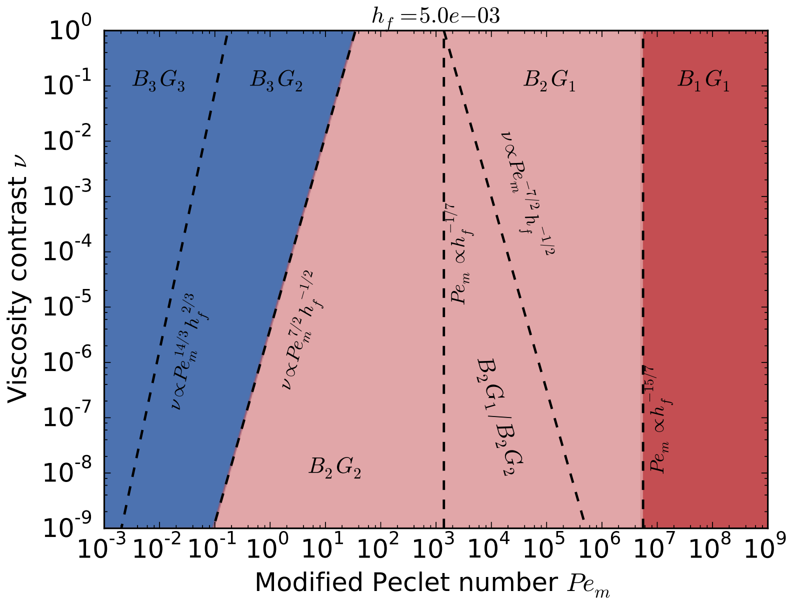

Figure 4.14: Phase diagram for the evolution with bending and gravity for the more realistic case discussed in this chapter for different combinations (ν,Pe_m) and a given value of $h_f = 0.005$. B_iG_j refers to the case where the current transitions from the ith bending thermal phase to thew jth gravity thermal phase where i and $j \in \{1, 2, 3\}$.

4.5 Application to the spreading of shallow magmatic intrusions

4.5.1 Elba Island christmas-tree laccolith complex

The isoviscous elastic-plated gravity current model has been used in Chapter 2 to study the laccoliths of Elba Island (*Michaut*, 2011). It shows that, while their final morphology is consistent with their arrest in the bending regime, their dimension requires unreasonable magma viscosity to agree with the isoviscous model (Chapter 2). In addition, given the fracture toughness of rocks, their radius seems too small to be fractured controlled and their arrest might be better explained by their cooling (*Michaut*, 2011). In the following, we compare the new model predictions to the size of the laccoliths provided by *Rocchi et al.* (2002). In order to account for the intrinsic scale of different settings for each intrusion and compare them to the model, the data have first to be nondimensionalized using characteristic values for each intrusion parameters.

Table 4.2: Range of values for the model parameters

Parameters	Symbol	Earth	Moon	Unit
Depth of intrusion	d_c	$0.2 - 2.7$	$0.5 - 1.5$	km
Young's Modulus	E	10	10	GPa
Poisson's ratio	ν^*	0.25	0.25	
Gravity	g	9.81	1.62	m s^{-2}
Magma density	ρ_m	$2500 - 2900$	2900	kg m^{-3}
Liquidus magma viscosity	η_h	$10^2 - 10^6$	$1 - 10$	Pa s
Solidus magma viscosity	η_c	$10^6 - 10^{10}$	$10^3 - 10^5$	Pa s
Feeder dyke width	a	$1 - 100$	10	m
Depth of the melt source	Z_c	$1 - 10$	500	km
Initial overpressure	ΔP	$20 - 50$	50	MPa
Injection rate	Q_0	$0.1 - 10^3$	$1 - 10^4$	m^3 s^{-1}
Magma thermal conductivity	k_m	2.5	2.5	W K^{-1} m^{-1}
Magma thermal diffusivity	κ_m	10^{-6}	10^{-6}	m^2 s^{-1}
Magma liquidus temperature	T_L	900-1200	1200	
Magma solidus temperature	T_S	700-1000	1000	
Magma heat capacity	C_p	4.18×10^5	4.18×10^5	J kg^{-1} K^{-1}
Latent heat of crystallization	L	4.18×10^5	4.18×10^5	J kg^{-1}
Rock thermal diffusivity	κ_r	10^{-6}	10^{-6}	m^2 s^{-1}
Characteristic scales	**Symbol**	**Earth**	**Moon**	**Unit**
Height scale	H	$0.1 - 10$	$0.1 - 1$	m
Length scale	Λ	$1 - 7$	$2.2 - 12$	km
Time scale	τ	$10^{-3} - 100$	$10^{-3} - 10$	years
Dimensionless number	**Symbol**	**Earth**	**Moon**	
Peclet number	Pe	$10^{-4} - 500$	$10^{-3} - 10^4$	
Viscosity contrast	ν	$10^{-4} - 10^{-10}$	$10^{-3} - 10^{-5}$	
Modified Stefan number	St_m	$0.1 - 0.5$	$0.1 - 0.5$	
	Ω	1	1	

Range of values for the dimensionless numbers

The different parameters along with a discussion on the possible values for h_f have been provided in chapter 2 and are summarized in table 4.2. We refer the reader to Section 2.3.2 for more details about their derivation. In the following, we quantify the values of the dimensionless numbers introduced by the cooling of the current in the setting of Elba Island laccoliths.

For a latent heat of crystallization $L = 4.18 \times 10^5$ J kg^{-1}, a difference between solidus temperature T_S and liquidus temperature T_L between 100 K and 300 K, the number St_m varies from 0.1 to 0.5. For a thermal diffusivity for the magma equal to $\kappa_m = 10^{-6}$ m s^{-2}, an injection rate Q_0 between 0.1 and 100 m^3 s^{-1} and an intrusion depth between 0.2 and 2.7 km, the Peclet number varies from 10^{-3} to 100 and therefore, Pe_m varies from 0.01 to 1000. Finally, the increase in viscosity upon cooling varies from 4 to 6 for mafic magmas and can be up to 10 orders of magnitude for felsic magmas (*Shaw*, 1972; *Lejeune and Richet*, 1995; *Giordano et al.*, 2008; *Diniega et al.*, 2013). We thus consider that the viscosity contrast ν ranges from 10^{-4} to 10^{-10}.

It is generally assumed that the magma stops spreading when its crystal content becomes close to its maximum packing, i.e. $\phi \sim 60\%$ (*Pinkerton and Stevenson*, 1992). Beyond this point, crystal collisions dominate and the viscosity jumps to much higher values (*Lejeune and Richet*, 1995; *Giordano et al.*, 2008). We assume that this is equivalent to η_e tending to η_c in our model. With this assumption, the model thus predicts that a magmatic intrusion would solidify as a laccolith upon reaching the third bending phase.

Do laccoliths stop in the bending regime?

The thickness h_0 as a function of its radius R for a current that solidifies in the third phase of the bending regime can be derived from the scaling laws (3.54) and (3.55) and should follow

$$h_0 = 0.3 h_f^{-1/7} \nu^{-2/7} R^{8/7} \tag{4.46}$$

The observations show a very good agreement with the model for a viscosity contrast close to 8 orders of magnitude ($\nu = 6.9 \pm 2.3 \times 10^{-8}$, $r^2 = 0.9$), which is consistent with the felsic composition of these laccoliths, and $h_f = 0.001$ (Figure 4.15 a) (*Marsh*, 1981; *Diniega et al.*, 2013). Varying h_f has only minor effect on the best fit viscosity contrast and is discussed in Appendix B. Therefore, introducing the cooling in the elastic-plated gravity current model allows to reconciliate the model predictions and the observations in the case of laccoliths (Chapter 2). In particular, the shape of the laccolith at Elba Island is now entirely consistent with the model predictions and therefore with their arrest in the bending regime.

What can we learn from the phase diagram ?

Assuming that the intrusion stops when it reaches the third bending phase, the phase diagram proposed in section 4.4 simplifies (Figure 4.16). It shows that sills and laccoliths are two specific end member regions as a function of Pe and ν. In particular, while the top portion of the phase diagram corresponds to magmatic intrusions more mafic in composition, the bottom should be more representative of felsic magmatic intrusions. The boundary between the two

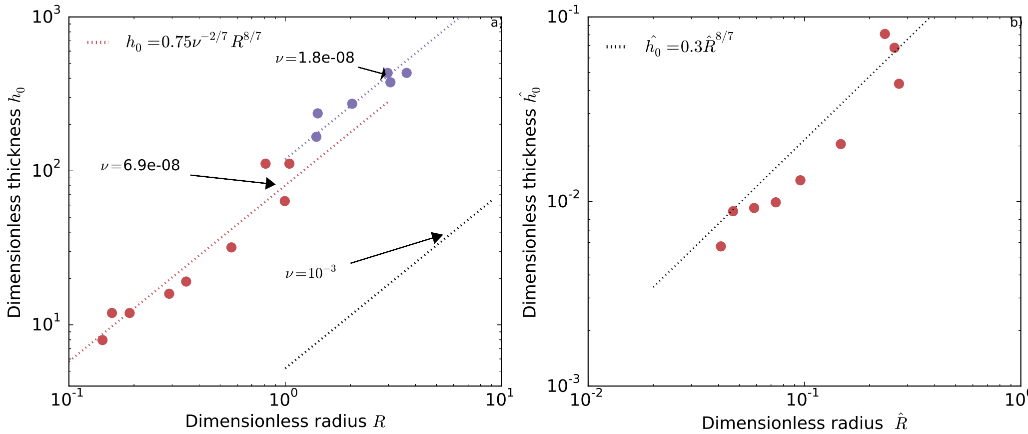

Figure 4.15: a) Dimensionless maximum thickness h_0 versus radius R for laccoliths from Elba Island and revised low-slope lunar domes. Parameters for calculating Λ (3.23) and H (3.24) are $E = 10^9$ GPa, $\nu^* = 0.25$, $\rho_m = 2500$ kg m^{-3}, $g = 9.81$ m s^{-2}, $\eta_h = 10^6$ Pa s and $Q_0 = 10$ m^3 s^{-1} on Earth and everything else being equal, $g = 1.62$ m s^{-2}, $\eta_h = 1$ Pa s on the Moon. Dotted lines: best fit scaling laws (4.46) with $h_f = 0.001$ for both laccoliths at Elba Island and low-slope lunar domes. $\nu = 6.9 \pm 2.3 \cdot 10^{-8}$ ($r^2 = 0.92$) and $\nu = 1.8 \pm 0.4 \cdot 10^{-8}$ ($r^2 = 0.88$) represent the linear least square best fit for the data on Earth and the Moon respectively. b) Dimensionless thickness $\hat{h}_0$ versus $\hat{R}$ where $\hat{h}_0$ and $\hat{R}$ are given by (4.48) with $h_f = 0.001$ for laccoliths at Elba Island. Substituting (3.25) into (3.33), we obtain $Pe = Q_0 H/(\pi\kappa\Lambda^2)$; the parameters for calculating Pe for each laccolith are the same than those used for the nondimensionalization, $\kappa = 10^{-6}$ m s^{-2} and St_m is considered constant and set to 0.1. The viscosity contrast is set to $\nu = 6.9 \cdot 10^{-8}$ for all laccoliths. Dotted line: scaling law $\hat{h}_0 \sim 0.3\hat{R}^{8/7}$.

regions show that felsic magmatic intrusions should solidify as sills on a larger range of number Pe. Indeed, felsic magmatic intrusions tend to be thicker than their mafic counterparts. In the framework of our model, they then stay hot for a longer period of time and therefore, can reach the gravity regime more easily. Given the felsic composition of Elba island laccoliths, this phase diagram can then be used to constrain the physical parameters of the magma. In the following, we use this approach to better constrain the injection rate feeding these laccoliths at the time of emplacement.

We first compute a value for the Peclet number for each laccolith at Elba Island using its corresponding depth of intrusion and the parameters listed in Figure 4.15. Indeed, injecting the scales (3.23), (3.24) and (3.25) in the

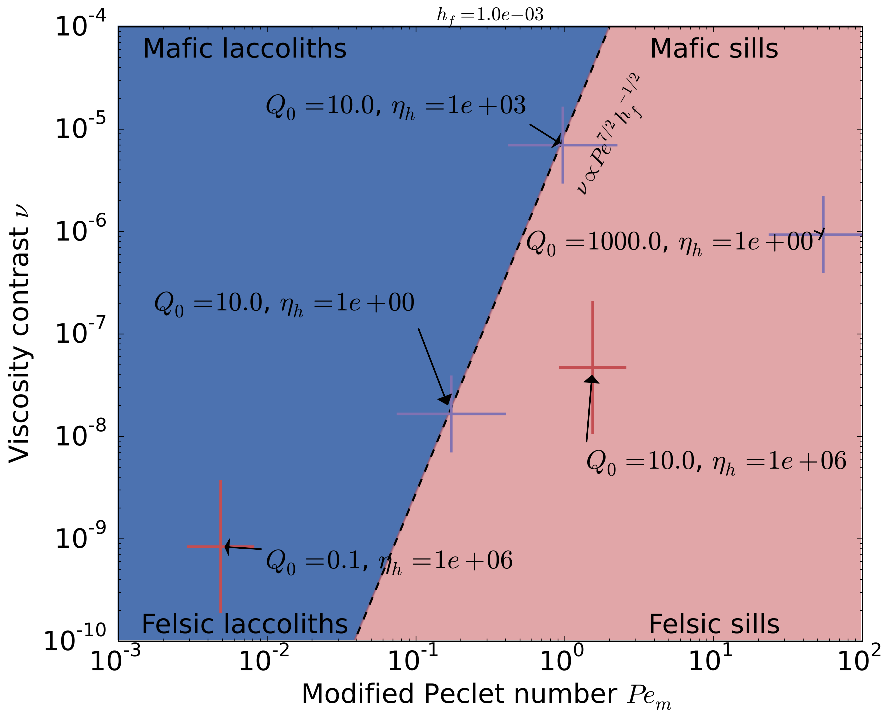

Figure 4.16: Subset of the phase diagram proposed in section 4.4 relevant for the study of terrestrial laccoliths. Red and purples crosses represent a range of value for ν and Pe for Elba Island laccoliths and low-slope lunar domes respectively. The width of each cross is defined by the minimum and the maximum value obtained for the Peclet number given the range of variation of parameters listed in table 4.2 and the injection rate Q_0 and the viscosity at the liquidus temperature η_h indicated on the plot. The height of the cross corresponds to the minimum and maximum values for the viscosity contrast obtain from (4.46) when $h_f = 0.001$.

expression of Pe (3.33), we find that in term of the injection rate and the depth of intrusion d_c, Pe reads

$$Pe \sim 10^3 d_c^{-3/2} Q^{5/4}. \tag{4.47}$$

For $St_m = 0.1$, the intrusion depths given by *Rocchi et al.* (2002) and $Q_0 = 10$ m^3 s^{-1}, the modified Peclet number Pe_m ranges from 1 to 6. As the best fit range of values for the viscosity contrast, discussed in the previous section, is $\nu = 6.9 \pm 2.3 \times 10^{-8}$, the phase diagram thus predicts that these laccoliths should have stop in the gravity regime indicating that we might have overestimated the injection rate (Figure 4.16). Indeed, taking a smaller value for the injection rate of $Q_0 = 0.1$ m^3 s^{-1}, reasonable for viscous felsic magmas (*Harris et al.*, 2000), the model predicts a larger viscosity contrast $\nu = 1.2 \pm 0.4 \times 10^{-9}$, still consistent with the range of expected values for felsic magmas, and weaker Peclet numbers. Therefore, the range of values for the dimensionless numbers now falls within the laccolith regions and is consistent with the observations (Figure 4.16).

Is conduction cooling enough to solifidy a laccolith ?

If the laccoliths stopped spreading as soon as they reached the third phase of the bending regime, the variance in thickness and radius in between the different intrusions should also be explained by variations in the Peclet number, most likely due to variations in intrusion depths in this example. Indeed, the time t_{b3}, necessary to reach the third phase of the bending regime, the thickness and the radius of the current at this time all depend on the combination (ν,Pe_m) considered (see Section 4.4).

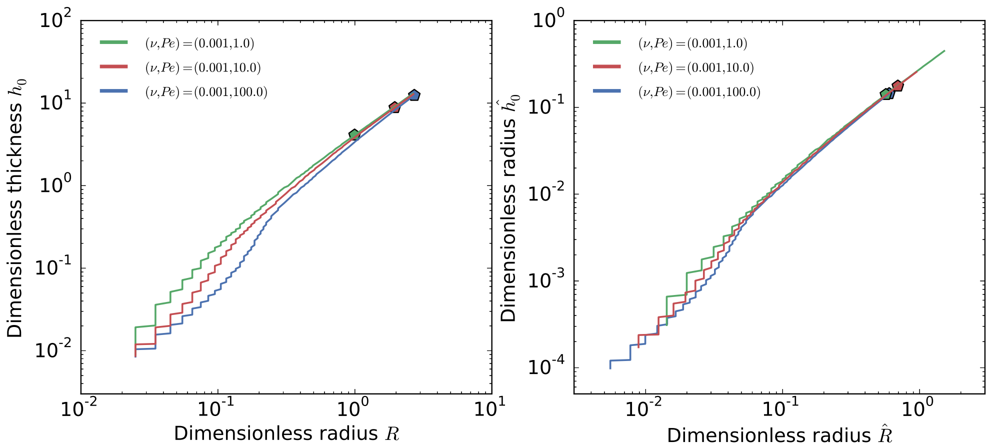

Figure 4.17: a) Dimensionless thickness at the center h_0 versus dimensionless radius R for different sets (ν, Pe) indicated on the plot ($\eta(\theta) = \eta_2$, $\Omega = 1.0$). Pentagons refer to the size where the effective viscosity of the current equal 70% of the maximum viscosity η_c, i.e. $\eta_e = 0.7\eta_c$. b) Dimensionless thickness $\hat{h}_0$ versus dimensionless radius $\hat{R}$ where $\hat{h}_0$ and $\hat{R}$ are given by (4.48) with $h_f = 0.001$. As expected, after rescaling h_0 and R, the sizes of the solidified laccoliths should collapse almost on the same point.

To test this hypothesis, we rescale the variables using the time t_{b3} (4.40) as follow

$$\hat{t} = h_f^{4/17} Pe_m^{-11/17} \nu^{8/17} t \quad \hat{R} = h_f^{1/34} Pe_m^{-7/34} \nu^{1/17} R \quad \hat{h}_0 = h_f^{3/17} Pe_m^{-4/17} \nu^{6/17} h_0 \tag{4.48}$$

where the viscosity contrast and the prewetting film thickess are constant, i.e. $\nu = 8.2 \cdot 10^{-9}$ and $h_f = 0.001$, and the Peclet number varies between each laccolith. In term of $\hat{h_0}$ and $\hat{R}$, the scaling law (4.46) rewrites $\hat{h_0} \sim 0.3\hat{R}^{8/7}$ and does not depend on the dimensionless numbers anymore (Figure 4.17). However, the different laccoliths do not collapse on the same dot after rescaling (Figure 4.15 b). In particular, the dependence of Pe of our scaling, resulting from different intrusion depths, is not enough to explain the variability in the size of terrestrial laccoliths. An additional cooling mechanism, amplifying the effect of Pe, is thus required to explain the exact extent of laccoliths, which could be extraction of heat by circulation of fluid on Earth. To test this hypothesis, we look at the low-slope domes on the Moon where conduction is most likely the only source of cooling.

4.5.2 Low-slope lunar domes

Circulation of fluid in the lunar crust is more likely to be absent and the model developed in this chapter is also appropriate for studying the cooling of low-slope lunar domes. In this section, we restrict our analysis to some specific domes whose characteristics have been precisely revisited by Mélanie Thiriet (Purple dots Figure 2.5). Their shapes and characteristics have already been discussed in chapter 2 and hereafter, we look at their dimension in the light of the cooling elastic-plated gravity current model.

Range of values for the dimensionless numbers

Parameters for the magma in lunar setting have been discussed in chapter 2 and are summarized in table 4.2. In particular, for a same injection rate, the smaller gravity, together with the higher density and the smaller viscosity of lunar magmas, leads to smaller Peclet numbers. For instance, for an intrusion 1.5 km deep, using $g = 1.62$ m s^{-2}, $\eta_h = 1$ Pa s and $\rho_m = 2900$ kg m^{-3} instead of $g = 9.81$ m s^{-2}, $\eta_h = 10^6$ Pa s and $\rho_m = 2500$ kg m^{-3} leads to a Peclet number two orders of magnitude smaller on the Moon than on Earth, i.e. $Pe = 0.04$ and $Pe = 1.8$ respectively. However, injection rates on the Moon are also more likely to be larger than on Earth. For an injection rate one to two orders of magnitude larger and d between 0.5 and 1.5 km, the range of Peclet number are in fact very similar, i.e. from 10^{-3} to 10^4. Therefore, taking $St_m = 0.1$, we have Pe_m that varies between 0.01 and 10^5 for low-slope lunar domes. Finally, lunar basalt are mafic in composition and the viscosity contrast ν should vary between 10^{-3} and 10^{-5} (*Diniega et al.*, 2013).

Constraining the magma physical properties

For an injection rate of $Q_0 = 10$ m^3 s^{-1} and the parameters listed in Table 4.2, the low-slope lunar dome dimensions are also consistent with a viscosity contrast of 8 order of magnitudes (best fit: $\nu = 1.8 \pm 0.4 \times 10^{-8}$) (Figure 4.15). Assuming that the intrusion depth ranges from 500 m to 5 km, the Peclet number ranges from 0.1 to 1 and the range of values for the dimensionless number falls at the boundary between the two domains in the phase diagram (Figure 4.16). It is consistent with the radius of these lunar domes being close to $R = 4$, i.e. close to the transition radius with the gravity regime (Figure 4.15). However, the estimate for the viscosity contrast is much larger than the value expected for mafic magmas. For the same injection rate and a viscosity for the magma at liquidus temperature of $\eta_h = 10^3$ Pa s instead of $\eta_h = 1$ Pa s, the model predicts a viscosity contrast close to 5 orders of magnitudes ($\nu = 6.9 \pm 1.8 \times 10^{-6}$), much closer to the expected value (Figure 4.16). A similar value for the viscosity contrast can be obtained for $\eta_h = 1$ Pa s and $Q_0 = 1500$ m^3 s^{-1}. However, in that case, the Peclet numbers are much larger and the range of values for the dimensionless numbers fall within the sill region (Figure 4.16). Therefore, it suggests that the injection rates for these lunar domes were most likely close to $Q_0 \sim 10$ m^3 s^{-1}, hence a few orders of magnitude smaller than the effusion rates estimated from the runout distances of some lava flows in the lunar maria i.e. $Q_0 \geq 10^6$ m^3 s^{-1} (*Gregg and Fink*, 1996).

Is conductive cooling enough to solidify a laccolith on the Moon ?

On the Moon, the dimensionless sizes of the domes vary by less than one order of magnitude and might be explain only by the conductive cooling of the magmatic intrusion (Figure 4.15). However, the depth of these intrusions have not yet been reported by *Wöhler et al.* (2009) and hence, we can not proceed as for Elba Island laccoliths to test this hypothesis. Instead, we estimate a range of intrusion depth that would produce a collapse of the rescaled size of the domes, i.e. $\hat{h_0}$ as a function of $\hat{R}$. Indeed, assuming that the different lunar domes differ only by their intrusion depth, $\hat{R} = \hat{R}^r$ implies that

$$d_c = (R/R^r)^{34/15}\, d_c^r \tag{4.49}$$

where the radii are with dimension and the topscript r denotes a reference dome. We take the largest dome as a reference and we set its depth to the largest reasonable value, i.e. $d_c = 5$ km, mainly to ensure that the dimensionless radius of the other domes remains smaller than 4. Injecting the dome radii in (4.49) then give intrusion depths between 0.5 km and 5 km and Peclet

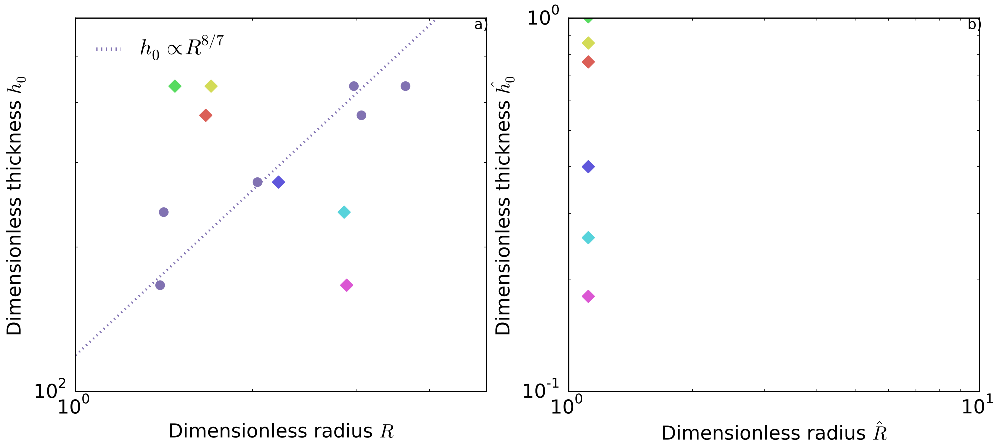

Figure 4.18: a) Dimensionless thickness h_0 versus dimensionless radius R for some lunar low-slope domes. Purple dots: characteristics length scale Λ (3.23) and thickness H (3.24) are calculated the same way as in Figure 4.15. Colored diamonds: characteristics length scale Λ (3.23) and thickness H (3.24) are calculated the same way as in Figure 4.15 except for the intrusion depth, taken from (4.49) with $R^r = 36.6$ km and $d_c^r = 5$ km. b) Dimension thickness $\hat{h_0}$ versus dimensionless radius $\hat{R}$. Colored polygons refers to the colors in a).

numbers between 10^{-2} and 0.5, consistent with the expected values. However, while this new parameters result in the collapse of $\hat{R}$ for the different domes, the variation in Peclet number can not account for the dispersion in the dome thicknesses (Figure 4.18). In addition, the dimensionless thickness as a function of the dimensionless radius does not follow the scaling law (4.46) anymore (Figure 4.18). The same observations are obtained using different reference domes or by setting the constrain on the rescaled thickness instead of the radius, i.e. $\hat{h} = \hat{h}_r$. Therefore, conductive cooling does not appear to be responsible for the arrest of terrestrial laccoliths.

4.5.3 Large mafic sills

As we discussed in chapter 2, the size of large mafic sills reported by *Cruden et al.* (2012) show an increasing thickness with diameter apparently in contradiction with the constant thickness predicted by the elastic-plated gravity current model (Figure 2.5). One possible explanation is that different sills are characterized by different injection rates, i.e. by different height scales. Forcing the dimensionless thicknesses of different sills to be constant imposes that

$$Q_0 = (h_0/h_0^r)^4 Q_r \tag{4.50}$$

where h_0 is the sill thickness with dimension, Q_0 its injection rate and h_0^r and Q_0^r are reference values for this parameters. Taking the thickest sill as a reference with $Q_0^r = 10^4$ m^3 s^{-1}, we find that in order to collapse all the data on a constant thickness, the injection rate have to vary by at least 7 orders of magnitudes, i.e. from $Q_0 = 10^{-3}$ to $Q_0 = 10^4$ m^3 s^{-1}. It is much larger than the expected range of variations for this parameter and hence, these mafic sills do not appear to have all stop in the third gravity regime. Another possible explanation is that fracturation at the tip, instead of cooling, have triggered the arrest of these magmatic intrusions in the second gravity phase. Indeed, while fracturation is not sufficient to stop a magmatic intrusion in the bending regime, it might be responsible for the arrest of large mafic sills (*Michaut*, 2011). The increasing thickness with diameter would thus be consistent with the thickness increase induced by the cooling of the sill in the second gravity phase. However, more information about the intrusion depth and the relationship between the different sill units, which are not given by *Cruden et al.* (2012), would be required to precisely test this hypothesis.

4.5.4 Thermal aureole

4.6 Summary and discussion

In this chapter, we discuss a more realistic model for the emplacement of magmatic intrusions in the shallow crust of terrestrial planets. In particular, we describe the dynamics of a magma characterized by an Arrhenius rheology and heating the surrounding layer as it spreads. We show that relaxing the thermal boundary condition decreases the heat loss in the surrounding rocks and therefore, allows the intrusion to stay hot for a longer period of time. In particular, the thermal anomaly detaches slower from the tip of the intrusion and does not reach a steady state anymore in the gravity regime as the heating of the surrounding medium constantly decreases the heat loss in the central region. Nevertheless, the Arrhenius rheology largely compensates for the delay in the transition induced by the heating of the surrounding medium. Therefore, except for the third phase in both regimes which is reached slightly later, the dynamics shows only small variations in comparison to the one described in chapter 3.

Application of this model to the christmas-tree laccolith complex at Elba Island shows that the cooling allows to reconciliate the elastic-plated gravity current model with the observations. In particular, we show that the size of these laccoliths is now consistent with their arrest in the third bending phase. The model predicts an injection rate close 0.1 m^3 s^{-1} and a viscosity contrast close to 8 orders of magnitude consistent with the felsic composition of these laccoliths. Nevertheless, the dependence of the number Pe, resulting from different intrusion depths, is not enough to explain the variability in the size of these laccoliths. An additional cooling mechanism, amplifying the effect of Pe, is thus required to explain the exact extent of these laccoliths, which could be extraction of heat by circulation of fluid. However, further applications to low-slope lunar domes, where conduction is more likely to be the only cooling mechanism, do not show better results. Therefore, further mechanisms than cooling might be invoked to explain the arrest of magmatic intrusion in the laccolith regime.

Lager and more detailed observations could provide further insights in the emplacement of these laccoliths. In addition, precise information on the extent of the thermal aureole, which has not yet been reported in the literature, could provide precious constrain for the model. While some research has been conducted in this area, a complete picture of the solution has not yet been obtained, in regard to the evolution of the size and thickness of the intrusion as a function of the parameters of the problem (elasticity and toughness of the host rock, viscosity of the magma, injection rate of the feeder dyke, and depth of emplacement).

Part III

Cratères à sol fracturée: Témoins d'un magmatisme intrusif lunaire

Part IV

Summary and perspectives

Part V

Appendices and bibliography

Appendix A

Numerical scheme for a cooling elastic-plated gravity current

In this appendix, we present the numerical scheme used to solve the coupled nonlinear partial differential equations (4.8) and (4.9). The governing equations presented in Chapter 3 are just a particular case where $\Omega \to \infty$.

A.1 General procedure

The coupled nonlinear partial differential equations (4.8) and (4.9) are solved on a grid of size M defined by the relation $r_i = (i-0.5)\Delta r$ for $i = 1, .., M$. The grid is shifted at the center to avoid problem arising from the axisymmetrical geometry. We index the grid point by the indice i and denote the solution on this grid h_i and ξ_i and the secondary variables $\Theta_{b,i}$, $\Theta_{s,i}$ and δ_i. Both equations can be expressed on the convenient form

$$\frac{\partial u}{\partial t} - f = 0 \tag{A.1}$$

where u is the function we want to integrate and f a non-linear function that depends on u. We solve these equations by first discretizing all the spatial derivatives using Finite Difference. The accuracy of the scheme is determined by the higher order derivatives since their numerical approximation requires the largest number of sample points. We then get two systems of M ordinary differential equations with the form

$$\frac{\partial u_i}{\partial t} - f_i = 0 \qquad i = 1, ..., M \tag{A.2}$$

The time derivatives are first order and, since explicit schemes tend to be very sensitive and unstable, we use a fully implicit backward Euler scheme to get

$$\frac{u_i^{n+1} - u_i^n}{\Delta t} - f_i(u_i^{n+1}) = 0 \qquad i = 1, ..., M \tag{A.3}$$

Since $f_i(u_i^{n+1})$ is not a linear function, the system above cannot be re-arranged to solve u_i^{n+1} in term of u_i^n and an iterative method has to be employed instead.

Fixed point iteration method have shown poor results in converging toward the solution and we finally apply second order Newton's method to obtain the solution at each time step. In particular, we first linearize u^{n+1} around a guess of the solution by assuming $u^{n+1} = u^* + \delta u^n$, where u^* is a guess and δu^n is the error and we drop the i for clarity. Then, we expressed the non-linear part using a Taylor's expansion

$$f^{n+1} = f(u^{n+1}) = f(u^* + \delta u^n) = f(u^*) + J_f^h(u^*)\delta u^n$$

where $J_f^u(u^*)$ is the jacobian matrix for the function f evaluated in h^*. Injecting the expansion into (A.3) finally gives a system of M linear equations for the correction term δ_h^n which can be expressed as

$$(I - \Delta t J_f^u(u^*))\delta u^n = u^n - u^* + \Delta t f(u^*) \tag{A.4}$$

where I is the identity matrix. Therefore, each iteration solves for δu^n and we use $u_n + \delta u^n$ as a new guess u^* in each iteration. This is repeated until δu^n becomes sufficiently small. Finally, since the equations are coupled, we use a fixed-point iteration method to converge toward the solution (h, ξ) at each time step. Therefore, the algorithm is the following at each time step

- Start with a guess for the values of all variables.
- Solve the thickness equation (4.8) for h^{n+1} using Newton-Rhapsod method.
- Solve the heat equation (4.9) for ξ^{n+1} using h^{n+1} as a new guess for h^* and Newton-Rhapsod method.
- Repeat step one until further iterations cease to produce any significant changes in the values of both h^{n+1} and ξ^{n+1}.

The computational scheme is summarized in the following.

A.2 Thickness equation

The thickness equation (4.8) is written as

$$\frac{\partial h}{\partial t} - f(h, \xi) \;=\; 0 \tag{A.5}$$

with

$$f \;=\; \frac{1}{r}\frac{\partial}{\partial r}\left(r\phi\left(\frac{\partial}{\partial r}(h + P)\right)\right) + w_i \tag{A.6}$$

$$\phi \;=\; 12 I_1(h) \tag{A.7}$$

and where P is the dimensionless bending pressure $P = \nabla^4 h$.

Spatial discretization of f

The spatial discretization is obtained using a central difference scheme over a sub-grid shifted by $0.5\Delta r$ from the main grid. Therefore, we have

$$\begin{aligned} f_i &= \frac{1}{r_i \Delta_r}\left(r_{i+1/2}\phi_{i+1/2}\left(\frac{\partial h}{\partial r} + \frac{\partial P}{\partial r}\right)\Big|_{i+1/2} - r_{i-1/2}\phi_{i-1/2}\left(\frac{\partial h}{\partial r} + \frac{\partial P}{\partial r}\right)\Big|_{i-1/2}\right) \\ &= A_i \phi_{i+1/2}\left(h_{i+1} - h_i\right) - B_i \phi_{i-1/2}\left(h_i - h_{i-1}\right) \\ &+ A_i \phi_{i+1/2}\left(P_{i+1} - P_i\right) - B_i \phi_{i-1/2}\left(P_i - P_{i-1}\right) \\ &+ w_i \end{aligned} \quad \text{(A.8)}$$

where $A_i = r_{i+1/2}/(r_i \Delta_r^2)$ and $B_i = r_{i-1/2}/(r_i \Delta_r^2)$. The bending pressure term P is very stiff and needs a careful treatment. In particular, the fourth order derivative requires a fourth order central difference scheme and therefore, P_i is expressed over a seven point stencil on the main grid such that

$$P_i = \alpha_i h_{i-3} + \beta_i h_{i-2} + \gamma_i h_{i-1} + \lambda_i h_i + \kappa_i h_{i+1} + \delta_i h_{i+2} + \varepsilon_i h_{i+3} \quad \text{(A.9)}$$

with

$$\begin{aligned} \alpha_i &= \frac{1}{24\Delta r^4}\left(-4 + 3p_3\Delta_r\right) \\ \beta_i &= \frac{1}{24\Delta r^4}\left(48 - 24p_3\Delta_r - 2p_2\Delta_r^2 + 2p_1\Delta_r^3\right) \\ \gamma_i &= \frac{1}{24\Delta r^4}\left(-156 + 39p_3\Delta_r + 32p_2\Delta_r^2 - 16p_1\Delta_r^3\right) \\ \lambda_i &= \frac{1}{24\Delta r^4}\left(224 - 60p_2\Delta r^2\right) \\ \kappa_i &= \frac{1}{24\Delta r^4}\left(-156 - 39p_3\Delta_r + 32p_2\Delta_r^2 + 16p_1\Delta_r^3\right) \\ \delta_i &= \frac{1}{24\Delta r^4}\left(48 + 24p_3\Delta_r - 2p_2\Delta_r^2 - 2p_1\Delta_r^3\right) \\ \varepsilon_i &= \frac{1}{24\Delta r^4}\left(-4 - 3p_3\Delta_r\right) \end{aligned}$$

and where $p_1 = 1/r_i^3$, $p_2 = 1/r_i^2$ and $p_3 = 2/r_i$. Finally, the term $\phi_{i-1/2}$ and $\phi_{i-1/2}$, which depend on the variable Θ_b, δ as well as different power of h, are evaluated in $i - 1/2$ and $i + 1/2$ respectively. Different choices for the value of the variable at the mid-cell grid point do not show any significant difference and a simple average is taken such that the variable $u_{i+1/2}$ is taken as $0.5(u_i + u_{i+1})$.

Expression of the jacobian J_f^h

The discretized function f_i can be break down in three part, the gravitational part f_i^g which is expressed in term of the value of h on three grid points $\{i-1, i, i+1\}$, the bending part f_i^b which is expressed in term of the value of h on nine grid points $\{i-4, i-3, ..., i+3, i+4\}$ and the injection term which depends only on the grid point i such that

$$f_i = f_i^g + f_i^b + w_i \tag{A.10}$$

Therefore, the jacobian is nona-diagonal and its coefficient J_{il} are

$$J_{il} = \begin{cases} \frac{\partial f_i^b}{\partial h_l} & l = \{i-4, i-3, i-2, i+2, i+3, i+4\} \\ \frac{\partial f_i^g}{\partial h_l} + \frac{\partial f_i^b}{\partial h_l} & l = \{i-1, i, i+1\} \\ 0 & \text{otherwise} \end{cases} \tag{A.11}$$

The different terms can be easily derived from (A.8) and (A.9) with just slight adjustment coming from the boundary conditions.

Boundary condition

We begin with $h_i = h_f$ for $i = 1, .., M$. Since the flow is symmetric in $r = 0$, we require that

$$\left.\frac{\partial h}{\partial r}\right|_{r=0} = \left.\frac{\partial P}{\partial r}\right|_{r=0} = 0 \tag{A.12}$$

and therefore for $i = 1$, we have

$$\begin{aligned} f_i &= A_1 \phi_{i+1/2} \left(h_{i+1} - h_i\right) \\ &+ A_i \phi_{i+1/2} \left(P_{i+1} - P_i\right) \\ &+ w_i \end{aligned} \tag{A.13}$$

The expression of the bending pressure, evaluated over a 7 point stencils, is problematic close to the boundary and reflection formulae will be used in order to accommodate the boundary conditions *Patankar* (1980). In particular, we have $h_0 = h_1$, $h_{-1} = h_2$ and $h_{-2} = h_3$. Similarly, boundary condition at the end of the mesh is accounted by using a grid much larger than the flow itself and requiring

$$\left.\frac{\partial h}{\partial r}\right|_{r=r_M} = \left.\frac{\partial P}{\partial r}\right|_{r=r_M} = 0 \tag{A.14}$$

which gives for $i = M$

$$\begin{aligned} f_i &= B_i \phi_{i-1/2} \left(h_i - h_{i-1}\right) \\ &+ B_i \phi_{i-1/2} \left(P_i - P_{i-1}\right) \\ &+ w_i \end{aligned} \tag{A.15}$$

with $h_{i>=M} = h_f$.

Newton-Rhapsod method

The Newton-Rhapsod method reads

$$(I - \Delta t J_f^h(h_k^*))\delta h_k^n = h^n - h_k^* + \Delta t f(h_k^*) \tag{A.16}$$

where the k refers to the k iterations, I is a $M \times M$ diagonal matrix and $J_f^h(h^*)$ is a $M \times M$ nona-diagonal matrix. This system of linear equations can be solved using a nona-diagonal algorithm. At the first iteration, we use $h_1^* = h^n$ as a first guess and then we iterate using $h_k^* = h^n + \delta h_{k-1}^n$ as a new guess for each iterations until δh_k^n becomes sufficiently small. In particular, we require that

$$\delta h_k^n / h_k^* < \varepsilon \tag{A.17}$$

with $\varepsilon = 10^{-4}$.

A.3 Heat equation

The heat equation (4.9) is written as

$$\frac{\partial \xi}{\partial t} - g(h, \xi) \quad = \quad 0 \tag{A.18}$$

with

$$g = \frac{1}{r}\frac{\partial}{\partial r}(r\Gamma\xi) + \frac{1}{r}\frac{\partial}{\partial r}(r\Sigma) + 2Pe^{-1}St_m\frac{(\Theta_b - \Theta_s)}{\delta} \tag{A.19}$$

$$\overline{\theta} = \frac{1}{3}(2\Theta_b + \Theta_s) \tag{A.20}$$

$$\Gamma = -\frac{12}{\delta}\frac{\partial P}{\partial r}(\delta I_0(\delta) - I_1(\delta)) \tag{A.21}$$

$$\Sigma = \frac{12}{\delta}\frac{\partial P}{\partial r}\left(I_0(\delta)\left(G(\delta) - \delta\overline{\theta}\right) + \overline{\theta}I_1(\delta) - I_2(\delta)\right). \tag{A.22}$$

Spatial discretization of g

As for the thickness equation, the spatial discretization is obtained using a central difference scheme over a sub-grid shifted by $0.5\Delta r$ from the main grid. Therefore, we have

$$g_i = \left(C_i\Gamma_{i+1/2}\xi_{i+1/2} - D_i\Gamma_{i-1/2}\xi_{i-1/2}\right) \tag{A.23}$$

$$+ \left(C_i\Sigma_{i+1/2} - D_i\Sigma_{i-1/2}\right) \tag{A.24}$$

$$+ 2Pe^{-1}St_m\frac{\Theta_{b,i} - \Theta_{s,i}}{\delta_i} \tag{A.25}$$

with $C_i = r_{i+1/2}/(r_i\Delta r)$ and $D_i = r_{i-1/2}/(r_i\Delta r)$. We use the average between the grid point i and $i-1$ (resp. $i+1$) to evaluate the quantity in Γ and Σ at $i-1/2$ (resp. $i+1/2$). In addition, we use a classical upwind scheme to handle ξ at the mid grid point which requires

$$\xi_{i+1/2} = \xi_i \tag{A.26}$$

$$\xi_{i-1/2} = \xi_{i-1} \tag{A.27}$$

Expression of the Jacobian J_g^ξ

The expression of the Jacobian is much straightforward in that case and its coefficient J_{il} are

$$J_{il} = \begin{cases} -D_i\Gamma_{i-1/2} & l = i-1 \\ C_i\Gamma_{i+1/2} & l = i \\ 0 & \text{otherwise} \end{cases} \tag{A.28}$$

with only slight adjustment coming from the boundary conditions.

Boundary conditions

We consider $\Theta_b = 1$ and $\delta = 10^{-4}$ in the film at $t = 0$. In this way, we ensure that the average temperature across the film at $t = 0$ is close to 1. By construction, $D_1 = 0$ and therefore, for $i = 1$ we have

$$g_i = C_i\Gamma_{i+1/2}\xi_i + C_i\Sigma_{i+1/2} + 2Pe^{-1}St_m\frac{\Theta_{b,i} - \Theta_{s,i}}{\delta_i} \tag{A.29}$$

For $i = M$, we consider that $\Gamma_{i+1/2} = \Gamma_i$ and $\Sigma_{i=1/2} = \Sigma_i$. However, the choice for the boundary condition at the border of the grid $i = M$ is not important as we solve the problem over a grid much larger than the flow itself.

Newton-Rhapsod method

The Newton-Rhapsod method reads

$$(I - \Delta t J_g^\xi(\xi_k^*))\delta\xi_k^n = \xi^n - \xi_k^* + \Delta t f(\xi_k^*) \tag{A.30}$$

where the k refers to the k iterations, I is a $M \times M$ diagonal matrix and $J_f^h(\xi^*)$ is a $M \times M$ tri-diagonal matrix. This system of linear equations can be solved using a tri-diagonal algorithm. As for the thickness equation, at the first iteration, we use $\xi_1^* = \xi^n$ as a first guess and then we iterate using

$\xi_k^* = \xi^n + \delta\xi_{k-1}^n$ as a new guess for each iterations until $\delta\xi_k^n$ becomes sufficiently small. In particular, we require that

$$\delta\xi_k^n / \xi_k^* < \varepsilon \tag{A.31}$$

with $\varepsilon = 10^{-4}$. In addition, at each iteration, the quantity $\Theta_{s,k}^*$, $\Theta_{b,k}^*$ and δ_k^*, that are needed to evaluate Γ and Σ, are derived from the value of ξ_k^* using (4.22), (4.23) and (4.24)

A.4 Integral expressions

The model developed in Section 4.1 depends on the integrals

$$I_0(z) = \int_0^z \frac{1}{\eta(y)}\left(y - \frac{h}{2}\right) dy \tag{A.32}$$

$$I_1(z) = \int_0^z \frac{1}{\eta(y)}\left(y - \frac{h}{2}\right) y dy \tag{A.33}$$

$$I_2(z) = \int_0^y \frac{1}{\eta(y)}\left(y - \frac{h}{2}\right) G(y) dy \tag{A.34}$$

where $G(z)$ is a primitive of $\theta(z)$ where $z < \delta$ and is given by

$$G(z) = \frac{z\left(3\delta^2\Theta_s + 3\delta z(\Theta_b - \Theta_s) + z^2(\Theta_s - \Theta_b)\right)}{3\delta^2}. \tag{A.35}$$

In particular, the model requires the expression of $I_0(\delta)$, $I_1(\delta)$, $I_1(h)$ and $I_2(\delta)$.

Rheology 1: $\eta(\theta) = \eta_1(\theta)$

In that case, the four integrals can be easily derived and read

$$\begin{aligned}
I_0(\delta) &= \frac{\delta}{12}\left(6\delta\nu + (1-\nu)\left(-\alpha_1\delta + 2\alpha_1 h + 6\Theta_b\delta - 6\Theta_b h\right) - 6h\nu\right)\\
I_1(\delta) &= \frac{\delta^2}{120}\left(40\delta\nu + (1-\nu)\left(-4\alpha_1\delta + 5\alpha_1 h + 40\Theta_b\delta - 30\Theta_b h\right) - 30h\nu\right)\\
I_1(h) &= \frac{1}{60}\left((1-\nu)\left(-4\alpha_1\delta^3 + 10\alpha_1\delta^2 h - 10\alpha_1\delta h^2 + 5\Theta_b h^3\right) + 5h^3\nu\right)\\
I_2(\delta) &= -\frac{\delta^2}{2520}\left(378\alpha_1\delta\nu - 315\alpha_1 h\nu - 840\Theta_b\delta\nu + 630\Theta_b h\nu\right)\\
&\quad -\frac{\delta^2}{2520}(1-\nu)\left(-50\alpha_1^2\delta + 70\alpha_1^2 h + 462\alpha_1\Theta_b\delta - 420\alpha_1\Theta_b h - 840\Theta_b^2\delta + 630\Theta_b^2 h\right)
\end{aligned}$$

where $\alpha_1 = \Theta_b - \Theta_s$ has been introduced for clarity.

Rheology 2: $\eta(\theta) = \eta_2(\theta)$

For cases where $\nu < 1$, we have

$$\begin{aligned}
I_0(\delta) &= -\frac{\delta\nu^{1-\Theta_b}\left(\sqrt{\pi}\sqrt{\alpha_1}(2\delta-h)\sqrt{-\alpha_2}\mathrm{erf}\left(\sqrt{\alpha_1}\sqrt{-\alpha_2}\right)+2\delta\left(\nu^{\alpha_1}-1\right)\right)}{4\alpha_1\alpha_2} \\
I_1(\delta) &= \frac{\delta^2\nu^{1-\Theta_b}\left(\sqrt{\pi}\,\mathrm{erf}\left(\sqrt{\alpha_1}\sqrt{-\alpha_2}\right)\left(\alpha_1(h-2\delta)\alpha_2+\delta\right)\right)}{4\alpha_1^{3/2}(-\alpha_2)^{3/2}} \\
&+\frac{\delta^2\nu^{1-\Theta_b}\left(\sqrt{\alpha_1}\sqrt{-\alpha_2}\left(2\delta\left(\nu^{\alpha_1}-2\right)-h\nu^{\alpha_1}+h\right)\right)}{4\alpha_1^{3/2}(-\alpha_2)^{3/2}} \\
I_1(h) &= \frac{\nu^{1-\Theta_b}\left(\sqrt{\alpha_1}\sqrt{-\alpha_2}\left(12\delta^2\left(\delta\left(\nu^{\alpha_1}-2\right)-h\nu^{\alpha_1}+h\right)+\alpha_1(2\delta-h)^3\log(\nu)\right)\right)}{12\alpha_1^{3/2}(-\alpha_2)^{3/2}} \\
&-\frac{\nu^{1-\Theta_b}\left(3\sqrt{\pi}\delta\mathrm{erf}\left(\sqrt{\alpha_1}\sqrt{-\alpha_2}\right)\left(\alpha_1(h-2\delta)^2\alpha_2-2\delta^2\right)\right)}{12\alpha_1^{3/2}(-\alpha_2)^{3/2}}
\end{aligned}$$

$$\begin{aligned}
I_2(\delta) &= \frac{\delta^2\nu^{1-\Theta_b}\left(\sqrt{\pi}\mathrm{erf}\left(\sqrt{\alpha_1}\sqrt{-\alpha_2}\right)\left(-2\alpha_1(2\delta-h)(\alpha_1-3\Theta_b)\alpha_2^2-6\delta\Theta_b\alpha_2-3\delta\right)\right)}{24\alpha_1^{3/2}(-\alpha_2)^{5/2}} \\
&+\frac{\delta^2\nu^{1-\Theta_b}\left(2\sqrt{\alpha_1}\nu^{\alpha_1}\sqrt{-\alpha_2}\left(\nu^{-\alpha_1}(\alpha_2(-2\delta(\alpha_1-6\Theta_b)-3h\Theta_b)+2\delta-h)\right)\right)}{24\alpha_1^{3/2}(-\alpha_2)^{5/2}} \\
&+\frac{\delta^2\nu^{1-\Theta_b}\left(2\sqrt{\alpha_1}\nu^{\alpha_1}\sqrt{-\alpha_2}\left(2\delta\alpha_1\alpha_2-6\delta\Theta_b\alpha_2+\delta-\alpha_1h\alpha_2+3h\Theta_b\alpha_2+h\right)\right)}{24\alpha_1^{3/2}(-\alpha_2)^{5/2}}
\end{aligned}$$

where in addition to α_1, we also introduced $\alpha_2 = \log(\nu)$ for clarity. In the case where $\nu = 1$, the expression above simplify and read

$$\begin{aligned}
I_0(\delta) &= \frac{1}{2}\delta(\delta-h) \\
I_1(\delta) &= \frac{1}{12}\delta^2(4\delta-3h) \\
I_1(h) &= \frac{h^3}{12} \\
I_2(\delta) &= -\frac{1}{120}\delta^2(18\delta\alpha_1-40\delta\Theta_b-15\alpha_1h+30h\Theta_b)
\end{aligned}$$

Appendix B
Details on the phase diagram

A current in the ith thermal phase can transition in the jth phase of the gravity regime where $i \geq j$. Indeed, the effective viscosity being that of a small region at the tip in the bending regime and the average flow viscosity in the gravity regime, it cannot increase during the transition. Hence, B_1G_2, B_1G_3 and B_2G_3 are unfeasible (Table B.1 and Figure B.1 a). In addition, the transition from the third thermal phase of the bending regime to the first thermal phase of the gravity regime implies that $t_t^c < t_{b2}$ and $t_t^c > t_{g3}$, which is not possible (Table B.1 and Figure B.1 a). Therefore, the five possible sequences that remain are B_1G_1, B_2G_1, B_2G_2, B_3G_2 and B_3G_3 (Table B.1 and Figure B.1 a).

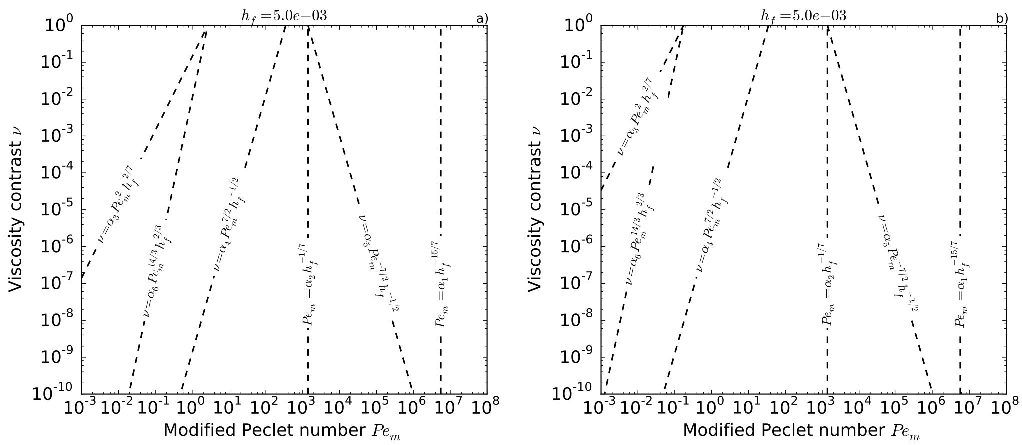

Figure B.1: a) Phase transitions reported in Table B.1 for the model described in Chapter 3. Same plot but for the more realistic model described in Chapter 4.

In the more realistic model described in Chapter 4, the time to enter the third flow phase is slightly delayed in both regimes. In particular, for the current that has reached the third bending phase, $t_t^c > t_{b3}$ now implies $\nu > 2.8 \cdot 10^{-7} Pe^{7/2} hf^{-1/2}$ (Figure B.1 b). In addition, comparing t_t^c and t_{g3} now reads $\nu < 1.2 \cdot 10^5 Pe_m^{14/3} h_f^{2/3}$ (Figure B.1 b).

Transition	Condition 1	Condition 2	Condition 3	Output
		Transition in the first bending thermal phase $B1$		
$t_t = t_t^h$	$t_t^h < t_{b2}$	$t_t^h < t_{g2}$	-	B_1G_1
	$Pe_m > \alpha_1 h_f^{-15/7}$	$Pe_m > \alpha_2 h_f^{-1/7}$	-	Feasible
$t_t = t_t^h$	$t_t^h < t_{b2}$	$t_t^h > t_{g2}$	$t_t^h < t_{g3}$	B_1G_2
	$Pe_m > \alpha_1 h_f^{-15/7}$	$Pe_m < \alpha_2 h_f^{-1/7}$	$\nu < \alpha_3 Pe_m^2 h_f^{2/7}$	Unfeasible
$t_t = t_t^h$	$t_t^h < t_{b2}$	$t_t^h > t_{g3}$	-	B_1G_3
	$Pe_m > \alpha_1 h_f^{-15/7}$	$\nu > \alpha_3 Pe_m^2 h_f^{2/7}$	-	Unfeasible
		Transition in the second bending thermal phase $B2$		
$t_t^h < t_t < t_t^c$	$t_t^h > t_{b2}$	$t_t^c < t_{b3}$	$t_t^c < t_{g2}$	B_2G_1
	$Pe_m < \alpha_1 h_f^{-15/7}$	$\nu < \alpha_4 Pe_m^{7/2} h_f^{-1/2}$	$\nu > \alpha_5 Pe_m^{-7/2} h_f^{-1/2}$	Feasible
$t_t^h < t_t < t_t^c$	$t_t^h > t_{b2}$	$t_t^c < t_{b3}$	$t_t^c < t_{g3}$	B_2G_2 or B_2G_1
	$Pe_m < \alpha_1 h_f^{-15/7}$	$\nu < \alpha_4 Pe_m^{7/2} h_f^{-1/2}$	$\nu < \alpha_6 Pe_m^{14/3} h_f^{2/3}$	Feasible
$t_t^h < t_t < t_t^c$	$t_t^h > t_{b2}$	$t_t^c < t_{b3}$	$t_t^h > t_{g2}$	B_2G_2
	$Pe_m < \alpha_1 h_f^{-15/7}$	$\nu < \alpha_4 Pe_m^{7/2} h_f^{-1/2}$	$Pe_m < \alpha_2 h_f^{-1/7}$	Feasible
$t_t^h < t_t < t_t^c$	$t_t^h > t_{b2}$	$t_t^c < t_{b3}$	$t_t^h > t_{g3}$	B_2G_3
	$Pe_m < \alpha_1 h_f^{-15/7}$	$\nu < \alpha_4 Pe_m^{7/2} h_f^{-1/2}$	$\nu > \alpha_3 Pe_m^2 h_f^{2/7}$	Unfeasible
		Transition in the third bending thermal phase $B3$		
$t_t = t_t^c$	$t_t^c > t_{b3}$	$t_t^c < t_{g2}$	-	B_3G_1
	$\nu > \alpha Pe_m^{7/2} h_f^{-1/2}$	$\nu > \alpha_5 Pe_m^{-7/2} h_f^{-1/2}$	-	Unfeasible
$t_t = t_t^c$	$t_t^c < t_{b2}$	$t_t^c > t_{g2}$	$t_t^c < t_{g3}$	B_3G_2
	$\nu > \alpha Pe_m^{7/2} h_f^{-1/2}$	$\nu < \alpha_5 Pe_m^{-7/2} h_f^{-1/2}$	$\nu < \alpha_6 Pe_m^{14/3} h_f^{2/3}$	Feasible
$t_t = t_t^c$	$t_t^c < t_{b2}$	$t_t^c > t_{g3}$	-	B_3G_3
	$\nu > \alpha Pe_m^{7/2} h_f^{-1/2}$	$\nu > \alpha_6 Pe_m^{14/3} h_f^{2/3}$	-	Feasible

Table B.1: Parameter space analysis. All conditions have to be respected for a scenario to be possible. For the model described in Chapter 3, the coefficients are: $\alpha_1 = 65$, $\alpha_2 = 650$, $\alpha_3 = 151$, $\alpha_4 = 8.3 \cdot 10^{-13}$, $\alpha_5 = 7.0 \cdot 10^9$, $\alpha_6 = 0.3$. For the more realistic model derived in Chapter 4, the coefficients are: $\alpha_1 = 65$, $\alpha_2 = 650$, $\alpha_3 = 0.6$, $\alpha_4 = 2.8 \cdot 10^{-7}$, $\alpha_5 = 7.0 \cdot 10^9$, $\alpha_6 = 1.2 \cdot 10^5$.

Appendix C
Effect of the prewetting film

To mitigate the problem at the contact line, we introduce a thin prewetting film, with thickness h_f such that $h(r,t) \to h_f$ as $r \to \infty$ (Section 2.1.3). In this appendix, we discuss the effect of changing the prewetting thickness h_f on some results presented in Chapter 3 and 4.

C.1 Scaling laws for the thickness and the radius

The scaling laws for the thickness $h_0(t)$ (3.54) as well as for the radius $R(t)$ (3.55) derived in Section 3.3 depends on the film thickness h_f. Accordingly,

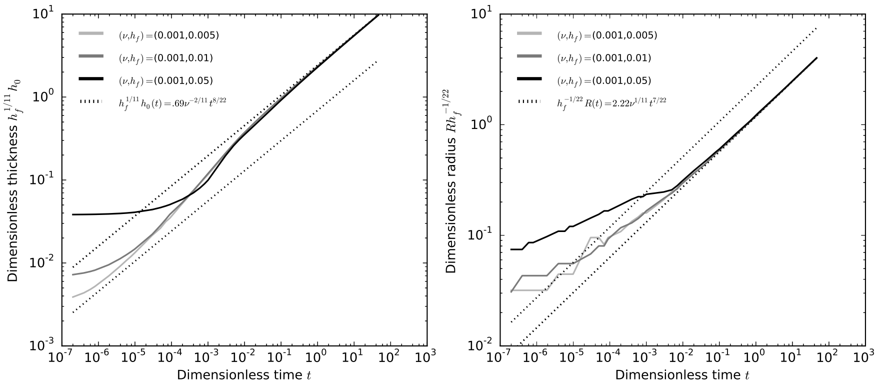

Figure C.1: Left: Dimensionless thickness at the center $h_0 h_f^{1/11}$ versus dimensionless time t for different sets (ν, h_f) indicated on the plot. Dashed-lines represent the scaling laws $h_0 h_f^{1/11} = 0.7\nu^{-2/11}t^{8/22}$ for $\nu = 1.0$ and 0.001. Right: Dimensionless radius R versus dimensionless time t for the same sets (ν, h_f). Dashed-lines represent the scaling laws $Rh_f^{-1/22} = 2.2\nu^{1/11}t^{7/22}$ for $\nu = 1.0$ and 0.001. Here, $\Omega = 10^5$ and $\eta(\theta) = \eta_1(\theta)$.

when rescaling the thickness by $h_f^{-1/11}$ and the radius by $h_f^{1/22}$, the different simulations collapse on the same curve (Figure C.1).

Similarly, when rescaling the extent of the cold fluid region $R(t) - R_c(t)$ by $h_f^{7/66}$, the different simulations also collapse on the same curve (Figure C.2).

Similar results can be obtained for $R(t) - R_c(t)$ in the framework of the more realistic model described in Chapter 4. These scaling laws are thus able to account for the effect of the prewetting film thickness h_f which is, in general, rather weak.

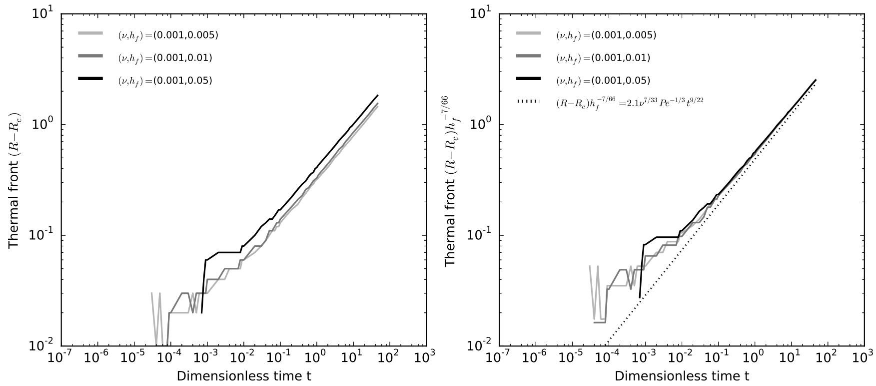

Figure C.2: Left: Extent of the cold fluid region $R(t) - R_c(t)$ versus dimensionless time for different combinations (ν, h_f) indicated on the plot. Right: Same plot but where we have rescaled the extent of the cold fluid region by $h_f^{7/66}$. Dashed-line: scaling law $(R(t) - R_c(t))h_f^{-7/66} = 2.1Pe^{-1/3}\nu^{7/33}t^{9/22}$.

C.2 Two stage growth in the second bending phase

In Chapter 4, for some simulations, the second phase of important thickening in the bending regime occurs in two stages: a first stage where the thickness drastically increases and a second stage where it continues increasing but much slower (Figure 4.3 and 4.4). To get some insights into this transition, we run some simulations for $\Omega = 1.0$ with a higher spatial resolution, i.e. $Dr = 0.005$ instead of $Dr = 0.01$ (Figure C.3).

The simulations show that this transition corresponds to the detachment of the thermal anomaly (Figure C.3). In particular, during the first stage, the thermal anomaly is still attached to the tip and the prewetting film, located beyond $r = R(t)$, is still cooling. In contrast, during the second stage, which is characterized by a decrease in the thickening rate, the prewetting film located beyond $r = R(t)$ is entirely cold , i.e. $\overline{\theta} = 0$ for $r > R(t)$ and the thermal anomaly slowly gets away from the tip (Figure C.3). For instance, for $\eta_1(\theta)$, $\nu = 0.001$ and $Pe = 100.0$, the transitions between the two stages occurs at $t = 1.8\ 10^{-2}$ and indeed coincide to the film becoming entirely cold (Figure

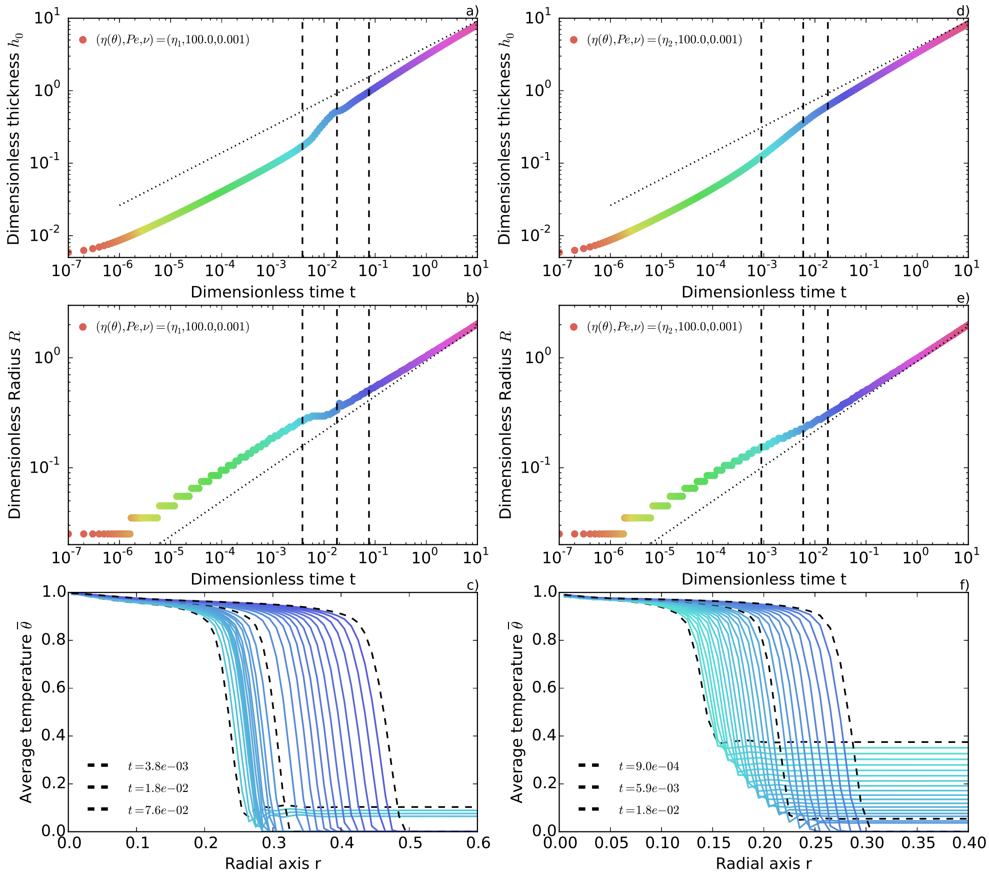

Figure C.3: Dimensionless thickness h_0 versus dimensionless time t for $Pe = 100.0$, $\nu = 0.001$, $\Omega = 1.0$ and the rheology $\eta_1(\theta)$. Colors refer to the time t. Dotted line: Scaling law $h_0 = 0.7 h_f^{-1/11} \nu^{-2/11} t^{8/22}$. Vertical dashed-lines: initial, intermediate and final times of the temperature profiles plotted in c). b) Dimensionless radius R versus dimensionless time t for $Pe = 100.0$, $\nu = 0.001$ and the rheology $\eta_1(\theta)$. Colors refer to the time t. Dotted line: Scaling law $R = 2.2 h_f^{1/22} \nu^{1/11} t^{7/22}$. Vertical dashed-lines: same than in a). c) Dimensionless average temperature over the flow thickness $\overline{\theta}$ versus radial axis r for times between $t = 3.8\ 10^{-3}$ and $t = 7.6\ 10^{-2}$. Dashed-line profiles: profiles at the three different times underlined in a) and b). Colors also refer to the time on the same scale than a) and b). d), e) and f), same plots than a), b) and c) but for the Arrhenius rheology η_2.

C.3 a, b, c). For the rheology $\eta_2(\theta)$, the transition is smoother because the viscosity increases on a wide range of temperature (Figure C.3 d, e, f). Even if this transition should be present for all the simulations, the smaller spatial resolution used in this Chapter 3 and 4 does not allow to resolve this transition for all the combinations of the dimensionless numbers.

C.3 Phase diagram

The phase diagram presented in section 4.4 and its application to the spreading of laccoliths depends on the chosen value for h_f. The meaning of the prewetting film thickness in the application to the spreading of laccolith is unclear. However, reasonable values for h_f are values with physical significance for this structural length scale at the tip of a laccolith and should range from a few centimeters to no less than 0.1 millimeter. Therefore, as the dependence with h_f is weak, a variation of 2 orders of magnitude does not change significantly the results (Figure C.4).

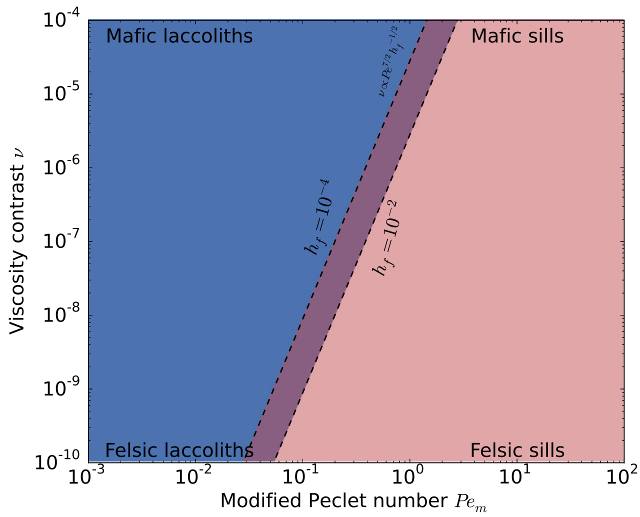

Figure C.4: Phase diagram for the evolution with bending and gravity for different combinations (ν,Pe_m) and different values for the film thickness $h_f = 10^{-2}$ and 10^{-4}.

The same result hold when we look at the relation between the thickness and the radius of the laccolith (4.46). Indeed, the best fit for the value of the viscosity contrast scales as $h_f^{-1/2}$, i.e. $\nu_{\text{best}} = h_f^{-1/2} 2.59\ 10^{-10}$ and therefore, varying h_f by two orders of magnitudes change the viscosity contrast by one order of magnitude which is acceptable for our application.

Bibliography

Anderson, E. M. (1951), The dynamics of faulting and dyke formation with applications to Britain. (Cited on page 7.)

Balmforth, N. J., and R. V. Craster (2004), Dynamics of cooling viscoplastic domes, *J. Fluid Mech.* (Cited on pages 39, 45, 48, 49 and 52.)

Barmin, A., O. Melnik, and R. Sparks (2002), Periodic behavior in lava dome eruptions, *Earth and Planetary Science Letters*, *199*(1-2), 173–184. (Cited on page 33.)

Bercovici, D. (1994), A theoretical model of cooling viscous gravity currents with temperature-dependent viscosity, *Geophys. Res. Lett.* (Cited on pages 39, 45, 46, 66 and 85.)

Bercovici, D., and J. Lin (1996), A gravity current model of cooling mantle plume heads with temperature-dependent buoyancy and viscosity, *J. Geophys. Res.*, *101*(B2), 3291–3309. (Cited on pages 39 and 45.)

Bertozzi, A. L. (1998), The mathematics of moving contact lines in thin liquid films, *Notices AMS.* (Cited on page 26.)

Blatt, H., R. J. Tracy, and B. Owens (2006), Petrology: igneous, sedimentary, and metamorphic. (Cited on page 85.)

Bunger, A. P., and A. R. Cruden (2011), Modeling the growth of laccoliths and large mafic sills: Role of magma body forces, *J. Geophys. Res.*, *116*(B2), B02,203. (Cited on pages 22, 27, 29 and 44.)

Bunger, A. P., and D. Emmanuel (2005), Near-surface hydraulic fracture, *Engineering Fracture Mechanics*, *72*(16), 2468–2486. (Cited on page 37.)

Cameron, A., and W. Benz (1991), The origin of the Moon and the single impact hypothesis IV, *Icarus*, *92*, 204–216. (Cited on page 13.)

Canup, R. M. (2012), Forming a Moon with an Earth-like composition via a giant impact, *Science*, *338*, 1052–1055. (Cited on page 13.)

Canup, R. M., and E. Asphaug (2001), Origin of the Moon in a giant impact near the end of the Earth's formation, *Nature*, *412*(6848), 708–712. (Cited on page 13.)

Carslaw, H. S., and J. C. Jaeger (1959), Heat in solids. (Cited on page 82.)

Castro, J. M., C. I. Schipper, S. P. Mueller, A. S. Militzer, A. Amigo, C. S. Parejas, and D. Jacob (2013), Storage and eruption of near-liquidus rhyolite magma at Cordón Caulle, Chile, *Bull Volcanol*, *75*(4), 1–17. (Cited on page 33.)

Chevrel, M. O., T. Platz, E. Hauber, D. Baratoux, Y. Lavallée, and D. B. Dingwell (2013), Lava flow rheology: A comparison of morphological and petrological methods, *Earth and Planetary Science Letters*, *384*(C), 109–120. (Cited on page 33.)

Clemens, J. D., and C. K. Mawer (1992), Granitic magma transport by fracture propagation, *Tectonophysics*, *204*(3-4), 339–360. (Cited on pages 6 and 7.)

Corry, C. E. (1988), Laccoliths: mechanics of emplacement and growth. (Cited on pages 12, 18, 19, 30, 31 and 34.)

Crisp, J., and S. Baloga (1990), A method for estimating eruption rates of planetary lava flows, *Icarus*, *85*(2), 512–515. (Cited on page 36.)

Crisp, J. A. (1984), Rates of magma emplacement and volcanic output, *Journal of Volcanology and Geothermal Research*, *20*(3-4), 177–211. (Cited on page 9.)

Cruden, A., and K. McCaffrey (2002), First international workshop on the-Physical Geology of Subvolcanic Systems – Laccoliths, Sills, and Dykes, in *LASI 1*, pp. 8–11. (Cited on page 19.)

Cruden, A., A. Bunger, and S. Morgan (2012), Emplacement dynamics of laccoliths, sills and dykes from dimensional scaling and mechanical models, in *LASI 1*. (Cited on pages 10, 17, 18, 20, 31, 108 and 109.)

Das, S. B., I. Joughin, M. D. Behn, I. M. Howat, M. A. King, D. Lizarralde, and M. P. Bhatia (2008), Fracture Propagation to the Base of the Greenland Ice Sheet During Supraglacial Lake Drainage, *Science*, *320*(5877), 778–781. (Cited on page 44.)

Diniega, S., S. E. Smrekar, S. Anderson, and E. R. Stofan (2013), The influence of temperature-dependent viscosity on lava flow dynamics, *J. Geophys. Res. Earth Surf.*, *118*(3), 1516–1532. (Cited on pages 85, 102 and 106.)

Dixon, J. M., and D. G. Simpson (1987), Centrifuge modelling of laccolith intrusion, *9*(1), 87–103. (Cited on page 45.)

Dyskin, A. V., L. N. Germanovich, and K. B. Ustinov (2000), Asymptotic analysis of crack interaction with free boundary, *International journal of solids ...*, *37*(6), 857–886. (Cited on page 37.)

Elkins-Tanton, L. T., S. Burgess, and Q.-Z. Yin (2011), The lunar magma ocean: Reconciling the solidification process with lunar petrology and geochronology, *Earth and Planetary Science Letters*, *304*(3-4), 326–336. (Cited on page 13.)

Flitton, J. C., and J. R. King (2004), Moving-boundary and fixed-domain problems for a sixth-order thin-film equation, *European Journal of Applied Mathematics*, *15*(06), 713–754. (Cited on pages 26, 44 and 45.)

Garel, F., E. Kaminski, S. Tait, and A. Limare (2012), An experimental study of the surface thermal signature of hot subaerial isoviscous gravity currents: Implications for thermal monitoring of lava flows and domes, *J. Geophys. Res.*, *117*(B2), B02,205. (Cited on page 61.)

Garel, F., E. Kaminski, S. Tait, and A. Limare (2014), An analogue study of the influence of solidification on the advance and surface thermal signature of lava flows, *Earth and Planetary Science Letters*, *396*(C), 46–55. (Cited on pages 39 and 45.)

Gilbert, G. K. (1877), Report on the Geology of the Henry Mountains , Government Printing Office, Washington, DC. (Cited on pages 10 and 11.)

Giordano, D., J. K. Russell, and D. B. Dingwell (2008), Viscosity of magmatic liquids: A model, *Earth and Planetary Science Letters*, *271*(1-4), 123–134. (Cited on pages 33, 46 and 102.)

Glazner, A. F., J. M. Bartley, D. S. Coleman, W. Gray, and R. Z. Taylor (2004), Are plutons assembled over millions of years by amalgamation from small magma chambers?, *GSA Today*, *14*(4), 4–8. (Cited on pages 7 and 9.)

Goodman, T. R. (1958), *The heat-balance integral and its application to problems involving a change of phase*, Trans. ASME. (Cited on page 48.)

Gregg, T. K. P., and J. H. Fink (1996), Quantification of extraterrestrial lava flow effusion rates through laboratory simulations, *Journal of Geophysical Research: Planets (1991–2012)*, *101*(E7), 16,891–16,900. (Cited on page 107.)

Habert, G., and M. De Saint-Blanquat (2004), Rate of construction of the Black Mesa bysmalith, Henry Mountains, Utah, *Geological Society*. (Cited on page 12.)

Han, S.-C., N. Schmerr, G. Neumann, and S. Holmes (2014), Global characteristics of porosity and density stratification within the lunar crust from GRAIL gravity and Lunar Orbiter Laser Altimeter topography data, *Geophys. Res. Lett.*, *41*(6), 1882–1889. (Cited on page 14.)

Harris, A., J. B. Murray, S. E. Aries, M. A. Davies, L. P. Flynn, M. J. Wooster, R. Wright, and D. A. Rothery (2000), Effusion rate trends at Etna and Krafla and their implications for eruptive mechanisms, *102*(3-4), 237–269. (Cited on pages 33 and 105.)

Head, J. W., and L. Wilson (1992), Lunar mare volcanism: Stratigraphy, eruption conditions, and the evolution of secondary crusts, *Geochimica et Cosmochimica Acta*, *56*(6), 2155–2175. (Cited on page 14.)

Hewitt, I. J., N. J. Balmforth, and J. R. De Bruyn (2014), Elastic-plated gravity currents, pp. 1–29. (Cited on pages 22, 26, 27, 34, 44 and 45.)

Horsman, E., B. Tikoff, and S. Morgan (2005), Emplacement-related fabric and multiple sheets in the Maiden Creek sill, Henry Mountains, Utah, USA, *Journal of Structural Geology*, *27*(8), 1426–1444. (Cited on pages 12 and 19.)

Horsman, E., S. Morgan, M. de Saint-Blanquat, G. Habert, A. Nugent, R. A. Hunter, and B. Tikoff (2009), Emplacement and assembly of shallow intrusions from multiple magma pulses, Henry Mountains, Utah, *100*(1-2), 117–132. (Cited on pages 13 and 19.)

Hort, M. (1997), Cooling and crystallization in sheet-like magma bodies revisited, *Journal of Volcanology and Geothermal Research*, *76*(3-4), 297–317. (Cited on page 48.)

Hosoi, A., and L. Mahadevan (2004), Peeling, Healing, and Bursting in a Lubricated Elastic Sheet, *Phys. Rev. Lett.*, *93*(13), 137,802. (Cited on page 44.)

Huang, Q., and M. A. Wieczorek (2012), Density and porosity of the lunar crust from gravity and topography, *J. Geophys. Res.*, *117*(E5), E05,003. (Cited on page 14.)

Huppert, H. E. (1982a), The propagation of two-dimensional and axisymmetric viscous gravity currents over a rigid horizontal surface, *J. Fluid Mech.*, *121*(-1), 43–58. (Cited on pages 28, 45 and 55.)

Huppert, H. E. (1982b), Flow and instability of a viscous current down a slope, *Nature*. (Cited on page 51.)

Johnson, A. M., and D. D. Pollard (1973), Mechanics of growth of some laccolithic intrusions in the Henry mountains, Utah, I: field observations, Gilbert's model, physical properties and flow of the magma, *Tectonophysics*. (Cited on pages 12, 17, 19 and 38.)

Jozwiak, L. M., J. W. Head, M. T. Zuber, D. E. Smith, and G. A. Neumann (2012), Lunar floor-fractured craters: Classification, distribution, origin and implications for magmatism and shallow crustal structure, *J. Geophys. Res.*, *117*(E11), E11,005. (Cited on page 17.)

Kavanagh, J. L., and R. S. J. Sparks (2011), Insights of dyke emplacement mechanics from detailed 3D dyke thickness datasets, *Journal of the Geological Society*, *168*(4), 965–978. (Cited on page 10.)

Kavanagh, J. L., T. Menand, and R. S. J. Sparks (2006), An experimental investigation of sill formation and propagation in layered elastic media, *Earth and Planetary Science Letters*, *245*(3-4), 799–813. (Cited on pages 7, 8 and 19.)

Kerr, A. D., and D. D. Pollard (1998), Toward more realistic formulations for the analysis of laccoliths, *Journal of Structural Geology*, *20*(12), 1783–1793. (Cited on page 18.)

Kerr, R. C., and J. R. Lister (1995), Comment on "On the relationship between dike width and magma viscosity" by Yutaka Wada, *Journal of Geophysical Research: Solid* .... (Cited on page 33.)

Kiefer, W. S., R. J. Macke, D. T. Britt, A. J. Irving, and G. J. Consolmagno (2012), The density and porosity of lunar rocks, *Geophys. Res. Lett.*, *39*(7). (Cited on page 14.)

Koch, F. G., A. M. Johnson, and D. D. Pollard (1981), Monoclinal bending of strata over laccolithic intrusions, *Tectonophysics*, *74*(3-4), T21–T31. (Cited on pages 12, 19, 29 and 38.)

Krumbholz, M., C. F. Hieronymus, S. Burchardt, V. R. Troll, D. C. Tanner, and N. Friese (2014), Weibull-distributed dyke thickness reflects probabilistic character of host-rock strength, *Nature Communications*, *5*, 1–7. (Cited on page 10.)

Lejeune, A. M., and P. Richet (1995), Rheology of crystal-bearing silicate melts: An experimental study at high viscosities, *Journal of Geophysical Research: Planets (1991–2012)*, *100*(B3), 4215–4229. (Cited on pages 39, 45, 46 and 102.)

Lister, J. R., and R. C. Kerr (1991), Fluid-mechanical models of crack propagation and their application to magma transport in dykes, *Journal of Geophysical Research: Solid ...*, *96*(B6), 10,049–10,077. (Cited on pages 7, 17 and 37.)

Lister, J. R., G. G. Peng, and J. A. Neufeld (2013), Viscous Control of Peeling an Elastic Sheet by Bending and Pulling, *Phys. Rev. Lett.*, *111*(15), 154,501. (Cited on pages 22, 26, 27, 28, 29, 33, 44, 45, 46, 54, 55, 62 and 74.)

Maccaferri, F., E. Rivalta, D. Keir, and V. Acocella (2014), Off-rift volcanism in rift zones determined by crustal unloading, *Nature Geosci*, *7*(4), 297–300. (Cited on page 8.)

Marsh, B. D. (1981), On the crystallinity, probability of occurrence, and rheology of lava and magma, *Contr. Mineral. and Petrol.*, *78*(1), 85–98. (Cited on pages 46 and 102.)

McCaffrey, K., and N. Petford (1997), Are granitic intrusions scale invariant?, *Journal of the Geological Society*, *154*(1), 1–4. (Cited on pages 18, 19 and 34.)

McKenzie, D. (1984), The Generation and Compaction of Partially Molten Rock, *Journal of Petrology*, *25*(3), 713–765. (Cited on page 6.)

McKenzie, D. (1985), The extraction of magma from the crust and mantle, *Earth and Planetary Science Letters*, *74*(1), 81–91. (Cited on page 6.)

Menand, T. (2011), Physical controls and depth of emplacement of igneous bodies: A review, *Tectonophysics*, *500*(1-4), 11–19. (Cited on pages 7, 19 and 38.)

Menand, T., K. A. Daniels, and B. P (2010), Dyke propagation and sill formation in a compressive tectonic environment, *J. Geophys. Res.*, *115*(B08201). (Cited on page 8.)

Michaut, C. (2011), Dynamics of magmatic intrusions in the upper crust: Theory and applications to laccoliths on Earth and the Moon, *J. Geophys. Res. Solid Earth*, *116*(B05205). (Cited on pages 20, 21, 22, 26, 27, 28, 29, 30, 34, 35, 36, 38, 39, 44, 45, 51, 52, 54, 55, 100 and 109.)

Michaut, C., and D. Bercovici (2009), A model for the spreading and compaction of two-phase viscous gravity currents, *J. Fluid Mech.*, *630*, 299–329. (Cited on pages 26 and 52.)

Michaut, C., and C. Jaupart (2006), Ultra-rapid formation of large volumes of evolved magma, *Earth and Planetary Science Letters*, *250*(1-2), 38–52. (Cited on page 48.)

Miller, R. B., and S. R. Paterson (1999), In defense of magmatic diapirs, *Journal of Structural Geology*, *21*(8-9), 1161–1173. (Cited on page 7.)

Mizutani, H., T. Matsui, and H. Takeuchi (1972), Accretion process of the moon, *The Moon*, *4*(3-4), 476–489. (Cited on page 13.)

Morgan, S., A. Stanik, E. Horsman, B. Tikoff, M. de Saint-Blanquat, and G. Habert (2008), Emplacement of multiple magma sheets and wall rock deformation: Trachyte Mesa intrusion, Henry Mountains, Utah, *Journal of Structural Geology*, *30*(4), 491–512. (Cited on pages 12, 19 and 38.)

Patankar, S. (1980), Numerical heat transfer and fluid flow. (Cited on page 120.)

Petford, N., R. C. Kerr, and J. R. Lister (1993), Dike transport of granitoid magmas, *Geology*, *21*(9), 845–848. (Cited on page 7.)

Petford, N., A. R. Cruden, K. McCaffrey, and J. L. Vigneresse (2000), Granite magma formation, transport and emplacement in the Earth's crust, *Nature*, *408*(6813), 669–673. (Cited on page 9.)

Pieri, D. C., and S. M. Baloga (1986), Eruption rate, area, and length relationships for some Hawaiian lava flows, *Journal of Volcanology and Geothermal Research*, *30*(1-2), 29–45. (Cited on page 33.)

Pinel, V., and C. Jaupart (2000), The effect of edifice load on magma ascent beneath a volcano, ... *Transactions of the Royal* .... (Cited on page 8.)

Pinel, V., and C. Jaupart (2004), Magma storage and horizontal dyke injection beneath a volcanic edifice, *Earth and Planetary Science Letters*, *221*(1-4), 245–262. (Cited on page 8.)

Pinkerton, H., and R. J. Stevenson (1992), Methods of determining the rheological properties of magmas at sub-liquidus temperatures, *Journal of Volcanology and Geothermal Research*, *53*(1-4), 47–66. (Cited on page 102.)

Platz, T., P. K. Byrne, M. Massironi, and H. Hiesinger (2015), Volcanism and tectonism across the inner solar system: an overview, *Geological Society, London, Special Publications*, *401*(1), 1–56. (Cited on page 15.)

Pollard, D. D., and A. M. Johnson (1973), Mechanics of growth of some laccolithic intrusions in the Henry Mountains, Utah, II: bending and failure of overburden layers and sill formation, *Tectonophysics*, *18*(3-4), 311–354. (Cited on page 17.)

Rocchi, S., D. S. Westerman, A. Dini, F. Innocenti, and S. Tonarini (2002), Two-stage growth of laccoliths at Elba Island, Italy, *Geology*, *30*(11), 983–986. (Cited on pages 12, 19, 30, 31, 32, 100 and 104.)

Rocchi, S., D. S. Westerman, A. Dini, and F. Farina (2010), Intrusive sheets and sheeted intrusions at Elba Island, Italy, *Geosphere*. (Cited on pages 11 and 35.)

Roni, E., D. S. Westerman, and A. Dini (2014), Feeding and growth of a dyke–laccolith system (Elba Island, Italy) from AMS and mineral fabric data, *Journal of the Geological Society*, *171*, 413–424. (Cited on page 12.)

Rubin, A. M. (1995), Propagation of magma-filled cracks, *Annual Review of Earth and Planetary Sciences*. (Cited on pages 7, 10 and 17.)

Schultz, P. H. (1976), Floor-fractured lunar craters, *The Moon*, *15*(3-4), 241–273. (Cited on pages 15, 17 and 39.)

Schultz, R. A., R. Soliva, H. Fossen, C. H. Okubo, and D. M. Reeves (2008), Dependence of displacement–length scaling relations for fractures and deformation bands on the volumetric changes across them, *Journal of Structural Geology*, *30*(11), 1405–1411. (Cited on page 10.)

Shaw, H. R. (1972), Viscosities of magmatic silicate liquids; an empirical method of prediction, *Am J Sci*, *272*(9), 870–893. (Cited on pages 33, 39, 45, 46 and 102.)

Shearer, C. K. (2006), Thermal and Magmatic Evolution of the Moon, *Reviews in Mineralogy and Geochemistry*, *60*(1), 365–518. (Cited on page 36.)

Snoeijer, J. H., and B. Andreotti (2013), Moving Contact Lines: Scales, Regimes, and Dynamical Transitions, *Annu. Rev. Fluid Mech.*, *45*(1), 269–292. (Cited on page 26.)

Stasiuk, M. V., C. Jaupart, R. Stephen, and J. Sparks (1993), Influence of cooling on lava-flow dynamics, *Geology*, *21*(4), 335–338. (Cited on page 33.)

Taisne, B., and S. Tait (2009), Eruption versus intrusion? Arrest of propagation of constant volume, buoyant, liquid-filled cracks in an elastic, brittle host, *J. Geophys. Res.*, *114*(B6), B06,202. (Cited on page 7.)

Taisne, B., S. Tait, and C. Jaupart (2011), Conditions for the arrest of a vertical propagating dyke, *Bull Volcanol*, *73*(2), 191–204. (Cited on page 7.)

Thorey, C., and C. Michaut (2014), A model for the dynamics of crater-centered intrusion: Application to lunar floor-fractured craters, *J. Geophys. Res.* (Cited on page 45.)

Tsai, V. C., and J. R. Rice (2010), A model for turbulent hydraulic fracture and application to crack propagation at glacier beds, *J. Geophys. Res.*, *115*(F3), F03,007. (Cited on page 44.)

Tuffen, H., M. R. James, J. M. Castro, and C. I. Schipper (2013), Exceptional mobility of an advancing rhyolitic obsidian flow at Cordón Caulle volcano in Chile, *Nature Communications*, *4*. (Cited on page 33.)

Turcotte, D. L., and G. Schubert (1982), Geodynamics: Applications of continuum physics to geological problems, John Wiley, New York. (Cited on page 23.)

Wada, Y. (1994), On the relationship between dike width and magma viscosity, *J. Geophys. Res.*, *99*(B9), 17,743–17,755. (Cited on page 33.)

Walker, G. P. L. (1989), Gravitational (density) controls on volcanism, magma chambers and intrusions, *Australian Journal of Earth Science*, *36*(2), 149–165. (Cited on pages 7 and 10.)

Watanabe, T., T. Masuyama, K. Nagaoka, and T. Tahara (2002), Analog experiments on magma-filled cracks: Competition between external stresses and internal pressure, *Earth Planet Sp*, *54*(12), e1247–e1261. (Cited on page 7.)

White, S. M., J. A. Crisp, and F. J. Spera (2006), Long-term volumetric eruption rates and magma budgets, *Geochem. Geophys. Geosyst.*, *7*(3), Q03,010–21. (Cited on page 9.)

Whittington, A. G., B. M. Hellwig, H. Behrens, B. Joachim, A. Stechern, and F. Vetere (2009), The viscosity of hydrous dacitic liquids: implications for the rheology of evolving silicic magmas, *Bull Volcanol*, *71*(2), 185–199. (Cited on page 33.)

Wichman, R. W., and P. H. Schultz (1996), Crater-centered laccoliths on the Moon: Modeling intrusion depth and magmatic pressure at the crater Taruntius, *Icarus*, *122*(1), 193–199. (Cited on page 17.)

Wieczorek, M. A., M. T. Zuber, and R. J. Phillips (2001), The role of magma buoyancy on the eruption of lunar basalts, *Earth and Planetary Science Letters*, *185*(1-2), 71–83. (Cited on page 14.)

Wieczorek, M. A., G. A. Neumann, F. Nimmo, W. S. Kiefer, G. J. Taylor, H. J. Melosh, R. J. Phillips, S. C. Solomon, J. C. Andrews-Hanna, S. W. Asmar, A. S. Konopliv, F. G. Lemoine, D. E. Smith, M. M. Watkins, J. G. Williams, and M. T. Zuber (2013), The crust of the Moon as seen by GRAIL, *Science*, *339*(6120), 671–675. (Cited on page 14.)

Wöhler, C., R. Lena, and J. Phillips (2007), Formation of lunar mare domes along crustal fractures: Rheologic conditions, dimensions of feeder dikes, and the role of magma evolution, *Icarus*, *189*(2), 279–307. (Cited on pages 14 and 35.)

Wöhler, C., R. Lena, and Geologic Lunar Research Group (2009), Lunar intrusive domes: Morphometric analysis and laccolith modelling, *Icarus*, *204*(2), 381–398. (Cited on pages 18, 32, 35, 36 and 107.)

Zimbelman, J. R. (1998), Emplacement of long lava flows on planetary surfaces, *J. Geophys. Res. Solid Earth.* (Cited on page 36.)

Zuber, M. T., D. E. Smith, R. S. Zellar, G. A. Neumann, X. Sun, R. B. Katz, I. Kleyner, A. Matuszeski, J. F. McGarry, M. N. Ott, L. A. Ramos-Izquierdo, D. D. Rowlands, M. H. Torrence, and T. W. Zagwodzki (2009), The lunar reconnaissance orbiter laser ranging Investigation, *Space Sci Rev*, *150*(1-4), 63–80. (Cited on page 35.)